AFOSR-TR. 81-0614

LEVEL III

AD A102333

A088123

Annual Technical Report No. 2

April 1, 1980 - September 30, 1980

The views and conclusions contained in this
document are those of the authors and should
not be interpreted as necessarily representing
the official policies, either expressed or
implied, of the Defense Advanced Research
Projects Agency or the U. S. Government.

DTIC FILE COPY

81 8 03 072

REPORT DOCUMENTATION PAGE	READ INSTRUCTIONS BEFORE COMPLETING FORM

1. REPORT NUMBER AFOSR TR-81-0614	2. GOVT ACCESSION NO. AD-A102 333	3. RECIPIENT'S CATALOG NUMBER

4. TITLE (and Subtitle) DETERMINISTIC METHODS OF SEISMIC SOURCE IDENTIFICATION	5. TYPE OF REPORT & PERIOD COVERED Interim Annual
	6. PERFORMING ORG. REPORT NUMBER

7. AUTHOR(s) C. B. Archambeau	8. CONTRACT OR GRANT NUMBER(s) F49620-C-0018 ARPA Order-3291

9. PERFORMING ORGANIZATION NAME AND ADDRESS University of Colorado CIRES — Cooperative Inst Boulder, CO 80301	10. PROGRAM ELEMENT, PROJECT, TASK AREA & WORK UNIT NUMBERS 61102F A.O. 3291-32 2309/A1 A1

11. CONTROLLING OFFICE NAME AND ADDRESS AFOSR/NP Bolling AFB, DC 20332	12. REPORT DATE 20 July 1981
	13. NUMBER OF PAGES 140 144

14. MONITORING AGENCY NAME & ADDRESS(if different from Controlling Office) Annual technical rept. no. 2, 1 Apr-30 Sep 80,	15. SECURITY CLASS. (of this report) Unclassified
	15a. DECLASSIFICATION/DOWNGRADING SCHEDULE

16. DISTRIBUTION STATEMENT (of this Report)

Approved for public release; distribution unlimited

17. DISTRIBUTION STATEMENT (of the abstract entered in Block 20, if different from Report)

18. SUPPLEMENTARY NOTES

19. KEY WORDS (Continue on reverse side if necessary and identify by block number)

Seismic Radiation
Source Discrimination
Inversion Techniques
Underground nuclear explosives
Yield determination

20. ABSTRACT (Continue on reverse side if necessary and identify by block number)

The objectives of the research conducted were to: (1) Develop and perfect methods of synthesis of theoretical seismic radiation fields at regional and teleseismic distance ranges in order to provide a basis for developing, testing and understanding seismic source discrimination methods; (2) Develop formal inversion procedures to be used to obtain quantitative estimates of physical parameters of seismic sources and the medium and to

DD FORM 1473 EDITION OF 1 NOV 65 IS OBSOLETE
1 JAN 73

406887

(Abstract cont.)

use these estimates to determine underground explosion yields, and as a basis
for source identification and discrimination; and to (3) Develop the means and
methods to analyze seismic data for source identification and propagational
medium characteristics for event discrimation and yeild estimation purposes-

TABLE OF CONTENTS

Research on Deterministic Methods of

Seismic Source Identification

Report No. 2 - Summary

The objectives of the research conducted were to: (1) Develop and
perfect methods of synthesis of theoretical seismic radiation fields at
regional and teleseismic distance ranges in order to provide a basis for
developing, testing and understanding seismic source discrimination
methods; (2) Develop formal inversion procedures to be used to obtain
quantitative estimates of physical parameters of seismic sources and the
medium and to use these estimates to determine underground explosion yields,
and as a basis for source identification and discrimination; and to
(3) Develop the means and methods to analyze seismic data for source
identification and propagational medium characteristics for event
discrimination and yield estimation purposes.

In this report we describe methods of modal synthesis which provide
very detailed theoretical seismograms in the near and regional distance
ranges. In the discussion we give the mathematical basis for the method,
along with some examples of its use. We also describe a sophisticated
automatic signal analysis program, which is to be used to generate discrimination
variables from observed data. The program and underlying procedures were tested
using synthetic seismic signals in order to evaluate its performance in the
presence of interfering noise. The signal analysis program was also applied

to observed seismic data. The purpose of this program is to isolate

particular, important, seismic phases (discrete signals) and to obtain

accurate estimates of the spectral characteristics of these signals

for purposes of event discrimination. Based on its performance, on a

variety of observed and synthetic seismic data, it appears that the method

can provide much enhanced discrimination/event identification capability,

over currently used methods. Finally we illustrate, and discuss, the

use of theoretical event magnitude data (m_b and M_s) as a bases for event

identification. In particular we show that, based on theoretical m_b

versus M_s relations obtained by synthesizing seismic wave fields in the

teleseismic distance range, we can obtain good estimates of seismic source

parameters, in particular stress changes and failure zone dimensions for

earthquakes and effective stress and nonlinear zone dimensions for

explosions, and can use these parameters to form a discrimination available

(stress change divided by failure zone surface area) which can serve as

a very effective means of discriminating underground explosions from

earthquakes. As a supplement to this report, we include summary discussions

of (1) anomalous radiation from explosions and (2) the effects of

attenuation in the earth on seismic signals.

I. Introduction

The objectives of the research being conducted are to: (1) Develop methods of seismogram synthesis using mode superposition and related methods, (2) Finalize the theory for source inversion by modal decomposition, (3) Determine the anelastic characteristics of the medium using known source characteristics, (4) Interpret seismic event discrimination in terms of the physical properties of the source, (5) Establish seismic event discrimination methods from formal inversion techniques, and (6) Establish regional discrimination techniques based upon physical properties of the source.

In this report we emphasize research results relating to (1) seismogram synthesis, (2) automated regional and teleseismic signal analysis for discrimination and yield estimation, and (3) source property inversion and discrimination of events in terms of inferred physical characteristics of the source. In addition we have included, as appendices, discussions of the status of our knowledge and understanding of anomalous seismic radiation from explosions (Appendix 1) and a similar review of regional and teleseismic attenuation effects on body and surface waves (Appendix 2). Finally, in the Appendix 3, we include the complete set of theoretical m_b versus M_s curves generated for use in source property inferences (i.e. average stress changes and rupture or nonlinear zone dimensions). These latter curves form the basis for the formation of a discrimination approach which would rely explicitly on differences of source (physical) properties, as inferred from m_b and M_s magnitude data.

II. Modal Synthesis of Seismic Radiation Fields

Normal Mode Superposition - The Theoretical Basis

In the following sections we present a summary of the steps one must take to compute the normal mode eigenvalues and eigenfunctions. Since this subject has been treated in the past by a number of researchers, we have omitted much of the detailed analyses and given only the major steps. Basically, the analysis given here closely follows that of Ben-Menahem and Singh (1972) and Harkrider (1964) who show how to synthesize Rayleigh waves for a general point source. We do present, however, a number of new results and methods that constitute the basis for a successful mode representation of a complete synthetic seismogram.

Coordinate Systems and Layer Conventions

In order to easily match the boundary conditions at the horizontal layer interfaces, we use a cylindrical coordinate system which is shown in figure 1 along with the layer numbering conventions. Since we will be writing solutions of the wave equation in each individual layer and then matching boundary conditions throughout the stack, we employ both a global coordinate system and a set of local coordinates, each relative to an individual layer. The origin of the global coordinate system will be at the free surface with the positive z-axis pointing down. The origin of a local coordinate system will be at the top of the layer, with the radial and azimuthal coordinates being the same for all of the coordinate systems.

We distinguish between the global and local vertical coordinates by using an unsubscripted or unsuperscripted z for the global coordinate and a superscripted $\zeta^{(p)}$ for local coordinates where p is the layer index. The depth of the bottom of the pth layer in global coordinates is $z = h^{(p)}$ whereas the thickness of the pth layer is $\xi^{(p)}, (z = h^{(p-1)} + \zeta^{(p)})$. We use this dual representation for all of the functions of z as well. Whenever a

function of z appears without a layer superscript it is understood that the argument will be in global coordinates and whenever a layer superscript does appear, then the argument of the function will be in local coordinates. Thus for some function, $f(z)$

$$f(z)\bigg|_{z = h^{(p-1)} + \zeta^{(p)}} = f^{(p)}(\zeta^{(p)})$$

The Basic Solution

We follow Ben-Menahem and Singh (1972) and write the Fourier transformed solutions of the elastic wave equations in the pth layer in terms of the vector cylindrical harmonics, **P**, **B**, and **C** as:

$$u_\alpha^{(p)}(r,\vartheta,\zeta^{(p)};\omega) = \sum_{m=-\infty}^{m=+\infty} \int_0^\infty \widehat{u}_{\alpha m}^{(p)}(r,\vartheta,\zeta^{(p)};\omega,k)\, k\, dk \tag{1a}$$

= radial, transverse and vertical components of the displacement in the pth layer

$$T_\alpha^{(p)}(r,\vartheta,\zeta^{(p)};\omega) = \sum_{m=-\infty}^{m=+\infty} \int_0^\infty \widehat{T}_{\alpha m}^{(p)}(r,\vartheta,\zeta^{(p)};\omega,k)\, k\, dk \tag{1b}$$

= radial, transverse and vertical components of the traction across a horizontal plane in the pth layer.

Where

$$\widehat{u}_{\alpha m}^{(p)}(r,\vartheta,\zeta^{(p)};\omega,k) = x_{1m}^{(p)}(\zeta^{(p)};\omega,k)\mathbf{P}_{\alpha m}(r,\vartheta;k) +$$
$$+ x_{2m}^{(p)}(\zeta^{(p)};\omega,k)\mathbf{B}_{\alpha m}(r,\vartheta;k) + x_{3m}^{(p)}(\zeta^{(p)};\omega,k)\mathbf{C}_{\alpha m}(r,\vartheta;k) \tag{2a}$$

and

$$\widehat{T}_{\alpha m}^{(p)}(r,\vartheta,\zeta^{(p)};\omega,k) = X_{1m}^{(p)}(\zeta^{(p)};\omega,k)\mathbf{P}_{\alpha m}(r,\vartheta;k) +$$
$$+ X_{2m}^{(p)}(\zeta^{(p)};\omega,k)\mathbf{B}_{\alpha m}(r,\vartheta;k) + X_{3m}^{(p)}(\zeta^{(p)};\omega,k)\mathbf{C}_{\alpha m}(r,\vartheta;k). \tag{2b}$$

We define the vector cylindrical harmonics as follows:

$$[\mathbf{P}_m(r,\vartheta;k)] = \begin{bmatrix} 0 \\ 0 \\ J_m(k\,r)e^{im\vartheta} \end{bmatrix} \tag{3a}$$

$$[\mathbf{B}_m(r,\vartheta;k)] = \begin{vmatrix} \dfrac{\partial J_m(k\,r)}{\partial(k\,r)}\,e^{i\,m\,\vartheta} \\[2ex] \dfrac{J_m(k\,r)}{(k\,r)}\,\dfrac{\partial e^{i\,m\,\vartheta}}{\partial\vartheta} \\[2ex] 0 \end{vmatrix} \tag{3b}$$

$$[\mathbf{C}_m(r,\vartheta;k)] = \begin{vmatrix} \dfrac{J_m(k\,r)}{(k\,r)}\,\dfrac{\partial e^{i\,m\,\vartheta}}{\partial\vartheta} \\[2ex] -\dfrac{\partial J_m(k\,r)}{\partial(k\,r)}\,e^{i\,m\,\vartheta} \\[2ex] 0 \end{vmatrix} \tag{3c}$$

The Greek subscripts are used here as tensor indices which range from one to three.

We wish to impose the boundary conditions of continuity of displacements and tractions at layer interfaces, zero tractions across the free surface, and no sources at $z = \infty$. Since we have expressed the solution in a separable form and since the vector cylindrical harmonics are orthogonal, in order for these boundary conditions to be met we must impose them on the z dependent integrand factors in equations (2). Thus we can express the boundary conditions by the following:

(1) Continuity of displacements at the layer interfaces:

$$x_{\alpha m}^{(p-1)}(\zeta^{(p-1)})\Big|_{\zeta^{(p-1)}=\xi^{(p-1)}} = x_{\alpha m}^{(p)}(\zeta^{(p)})\Big|_{\zeta^{(p)}=0} \tag{4a}$$
$$\text{for } 1 < p \leqq N$$

(2) Continuity of tractions at the layer interfaces:

$$X_{\alpha m}^{(p-1)}(\zeta^{(p-1)})\Big|_{\zeta^{(p-1)}=\xi^{(p-1)}} = X_{\alpha m}^{(p)}(\zeta^{(p)})\Big|_{\zeta^{(p)}=0} \tag{4b}$$
$$\text{for } 1 < p \leqq N$$

(3) Zero tractions at the free surface:

$$[X_m^{(1)}(0)] = [0] \tag{4c}$$

(4) The Sommerfeld radiation condition (no sources at infinity) applies to:

$$x_{am}^{(N)}(\zeta^{(N)}) \quad \text{and} \quad X_{am}^{(N)}(\zeta^{(N)}).$$
(4d)

We specify a point source in layer $p = s$ and at $r = 0$ and $z = z_o$, ($\zeta^{(s)} = \delta^{(s)}$). We shall solve the problem of forced vibrations by adding a particular solution to the homogeneous or unforced solution in the source layer. The form of the particular solution will be the same as equations (1) with the only difference being that the z dependent integrand factors will be different from those of the homogeneous solution. Now, the particular solution exists only in the source layer and in all the other layers only the homogeneous solution given by equations (1) exists. We can thus express the total solution in the source layer as follows:

$$u_{\alpha}^{(s)}(r,\vartheta,\zeta^{(s)};\omega) = \sum_{m=-\infty}^{m=+\infty} \int_{0}^{\infty} (\widehat{u}_{am}^{(s)} + {}^{P}\widehat{u}_{am}^{(s)}) \, k dk$$
(5a)

and

$$T_{\alpha}^{(s)}(r,\vartheta,\zeta^{(s)};\omega) = \sum_{m=-\infty}^{m=+\infty} \int_{0}^{\infty} (\widehat{T}_{am}^{(s)} + {}^{P}\widehat{T}_{am}^{(s)}) \, k dk.$$
(5b)

Where the particular solution integrand factors are denoted by a P superscript and are given by:

$${}^{P}\widehat{u}_{am}^{(s)}(r,\vartheta,\zeta^{(s)};\omega,k) = w_{1m}^{(s)}(\zeta^{(s)};\omega,k)\mathbf{P}_{am}(r,\vartheta;k) + $$
$$+ \, w_{2m}^{(s)}(\zeta^{(s)};\omega,k)\mathbf{B}_{am}(r,\vartheta;k) + w_{3m}^{(s)}(\zeta^{(s)};\omega,k)\mathbf{C}_{am}(r,\vartheta;k)$$
(6a)

and

$${}^{P}\widehat{T}_{am}^{(s)}(r,\vartheta,\zeta^{(s)};\omega,k) = W_{1m}^{(s)}(\zeta^{(s)};\omega,k)\mathbf{P}_{am}(r,\vartheta;k) + $$
$$+ \, W_{2m}^{(s)}(\zeta^{(s)};\omega,k)\mathbf{B}_{am}(r,\vartheta;k) + W_{3m}^{(s)}(\zeta^{(s)};\omega,k)\mathbf{C}_{am}(r,\vartheta;k).$$
(6b)

The boundary conditions given by equations (4) must be modified at the upper and lower source layer interfaces as follows:

(1) Continuity of displacements at the upper and lower source layer interfaces:

$$x_{am}^{(s-1)}(\xi^{(s-1)}) = x_{am}^{(s)}(0) + w_{am}^{(s)}(0) \tag{7a}$$

$$x_{am}^{(s+1)}(0) = x_{am}^{(s)}(\xi^{(s)}) + w_{am}^{(s)}(\xi^{(s)}) \tag{7b}$$

(2) Continuity of tractions at the upper and lower source layer interfaces:

$$X_{am}^{(s-1)}(\xi^{(s-1)}) = X_{am}^{(s)}(0) + W_{am}^{(s)}(0) \tag{7c}$$

$$X_{am}^{(s+1)}(0) = X_{am}^{(s)}(\xi^{(s)}) + W_{am}^{(s)}(\xi^{(s)}) \tag{7d}$$

We now define two sets of vertical eigenfunctions from the homogeneous solution z dependent integrand factors corresponding to the P-SV and SH waves as:

$$[^R E(z)] = \begin{bmatrix} x_{1m}(z)/k \\ x_{2m}(z)/k \\ X_{1m}(z)/k^2 \\ X_{2m}(z)/k^2 \end{bmatrix} \tag{8a}$$

$$[^L E(z)] = \begin{bmatrix} x_{3m}(z)/k \\ X_{3m}(z)/k^2 \end{bmatrix} \tag{8b}$$

Similarly we separate the P-SV and SH components of the particular solution z dependent integrand factors as follows:

$$[^R S_m^{(s)}(\zeta^{(s)})] = \begin{bmatrix} w_{1m}^{(s)}(\zeta^{(s)})/k \\ w_{2m}^{(s)}(\zeta^{(s)})/k \\ W_{1m}^{(s)}(\zeta^{(s)})/k^2 \\ W_{2m}^{(s)}(\zeta^{(s)})/k^2 \end{bmatrix} \tag{9a}$$

$$[^L S_m^{(s)}(\zeta^{(s)})] = \begin{bmatrix} w_{3m}^{(s)}(\zeta^{(s)})/k \\ W_{3m}^{(s)}(\zeta^{(s)})/k^2 \end{bmatrix} \tag{9b}$$

The R superscripts correspond to the Rayleigh wave solutions and the L superscripts correspond to the love wave solutions. In this paper we will only consider the P-SV case and will develop the SH case in a separate

study. With this in mind we drop the R superscript in order to minimize notational clutter. We also note that the azimuthal subscript, m, has been dropped from the eigenfunctions, $[E]$, since they are m independent.

The Eigenfunction Solutions and the Propagator Matrices

The eigenfunction solutions for a single layer are given by Ben-Menahem and Singh and are:

$$[E^{(p)}(\zeta^{(p)})] = [B^{(p)}(\eta^{(p)}, \eta'^{(p)})] [C^{(p)}(\nu^{(p)}, \nu'^{(p)}; \zeta^{(p)})] [\Delta^{(p)}] \qquad (10)$$

where $[\Delta^{(p)}]$ is a 4 component vector of constant coefficients that are adjusted to satisfy the boundary conditions, $[B^{(p)}]$ is a (4 X 4) matrix which is a function only of the horizontal phase velocity and the layer elastic parameters, and $[C^{(p)}]$ is another (4 X 4) matrix which is z dependent. The values of $\eta^{(p)}$ and $\eta'^{(p)}$ are the P and S wave vertical phase velocities and are:

$$\eta^{(p)} = \begin{cases} \dfrac{c}{\sqrt{1 - (c/\alpha^{(p)})^2}} & \text{for } c < \alpha^{(p)} \\[2ex] \dfrac{c}{i\sqrt{(c/\alpha^{(p)})^2 - 1}} & \text{for } c > \alpha^{(p)} \end{cases} \qquad (11a)$$

$$\eta'^{(p)} = \begin{cases} \dfrac{c}{\sqrt{1 - (c/\beta^{(p)})^2}} & \text{for } c < \beta^{(p)} \\[2ex] \dfrac{c}{i\sqrt{(c/\beta^{(p)})^2 - 1}} & \text{for } c > \beta^{(p)} \end{cases} \qquad (11b)$$

and $\nu^{(p)}$ and $\nu'^{(p)}$ are the P and S wave vertical wavenumbers and are given by:

$$\nu^{(p)} = \frac{\omega}{\eta^{(p)}} \qquad (12a)$$

$$\nu'^{(p)} = \frac{\omega}{\eta'^{(p)}}. \qquad (12b)$$

The C matrix can be expressed as follows:

$$[C^{(p)}(\nu^{(p)},\nu'^{(p)};\zeta^{(p)})] \; = \; \begin{vmatrix} P^{(p)}(\nu^{(p)},\zeta^{(p)}) & 0 & 0 & 0 \\ 0 & \dfrac{1}{P^{(p)}(\nu^{(p)},\zeta^{(p)})} & 0 & 0 \\ 0 & 0 & Q^{(p)}(\nu'^{(p)},\zeta^{(p)}) & 0 \\ 0 & 0 & 0 & \dfrac{1}{Q^{(p)}(\nu'^{(p)},\zeta^{(p)})} \end{vmatrix}$$

(13)

where

$$P^{(p)}(\nu^{(p)},\zeta^{(p)}) \; = \; \exp(\nu^{(p)}\zeta^{(p)}) \tag{14a}$$

and

$$Q^{(p)}(\nu'^{(p)},\zeta^{(p)}) \; = \; \exp(\nu'^{(p)}\zeta^{(p)}). \tag{14b}$$

The B matrix is given in the appendix.

We can rewrite equation (10) in terms of initial values of the eigenfunctions at the tops of the layers and in so doing we define the propagator matrix, $[A^{(p)}]$.

$$[E^{(p)}(\zeta^{(p)})] \; = \; [A^{(p)}(\zeta^{(p)})]\,[E^{(p)}(0)] \tag{15}$$

where from equations (10), (13), and (14) it is easy to show that:

$$[A^{(p)}(\zeta^{(p)})] \; = \; [B^{(p)}(\eta^{(p)},\eta'^{(p)})]\,[C^{(p)}(\nu^{(p)},\nu'^{(p)};\zeta^{(p)})]\,[B^{(p)}(\eta^{(p)},\eta'^{(p)})]^{-1}. \tag{16}$$

The propagator matrix allows us to compute eigenfunctions at the bottom of a layer in terms of eigenfunctions at the top of the layer so that in global coordinates:

$$[E(h^{(p)})] \; = \; [A^{(p)}(\xi^{(p)})]\,[E(h^{(p-1)})]. \tag{17}$$

We can start at any layer interface, p, and propagate the eigenfunctions to any other interface, q, (where $p < q$) by applying the boundary conditions expressed by equations (4) and by repeating equations (17) and in so doing we define the interlayer or total propagator matrix, $[\mathbf{A}^{(q,p)}]$.

$$[E(h^{(q)})] \; = \; [\mathbf{A}^{(q,p)}]\,[E(h^{(p)})] \tag{18}$$

The interlayer propagator matrix is defined as follows:

$$[\mathbf{A}^{(q,p)}] \;=\; \prod_{l=p+1}^{q} [A^{(q+p+1-l)}(\xi^{(q+p+1-l)})] \tag{19}$$

The Dispersion Function, Eigenvalue, and Ellipticity Computations

In order to compute the eigenvalues we need to apply the boundary conditions given by equations (4c) and (4d) of zero tractions across the free surface and the Sommerfeld radiation condition in the infinite half-space at the bottom of the stack. The Sommerfeld radiation condition in the half-space can be insured by setting two of the constant coefficients in $[\Delta^{(N)}]$ to zero, so that the upward propagating terms, $P^{(N)}$ and $Q^{(N)}$, are eliminated from the solution of the ODE in the half-space. More precisely, the Sommerfeld radiation condition requires that:

$$\Delta_1^{(N)} \;=\; \Delta_3^{(N)} \;=\; 0$$

and thus,

$$\begin{bmatrix} 0 \\ \Delta_2^{(N)} \\ 0 \\ \Delta_4^{(N)} \end{bmatrix} \;=\; [B^{(N)}]^{-1}\,[E\,(h^{(N-1)})]. \tag{20}$$

By using the interlayer propagator matrix in equation (20) and extracting the first and third rows we can define the $(2 \times 4)\ D$ matrix.

$$\begin{bmatrix} 0 \\ 0 \end{bmatrix} \;=\; [D^{(p)}]\,[E\,(h^{(p)})] \tag{21}$$

where

$$\left.\begin{aligned} D_{1j}^{(N-1)} &= ([B^{(N)}]^{-1})_{1j} \\ D_{2j}^{(N-1)} &= ([B^{(N)}]^{-1})_{3j} \end{aligned}\right\}\; \text{when } p = N-1 \text{ and } j = 1,2,3,4 \tag{22a}$$

and

$$\left.\begin{aligned} D_{1j}^{(p)} &= \sum_{k=1}^{4} ([B^{(N)}]^{-1})_{1k}\,\mathbf{A}_{kj}^{(N-1,p)} \\ D_{2j}^{(p)} &= \sum_{k=1}^{4} ([B^{(N)}]^{-1})_{3k}\,\mathbf{A}_{kj}^{(N-1,p)} \end{aligned}\right\}\; \text{when } N-1 > p \geq 0 \text{ and } j = 1,2,3,4. \tag{22b}$$

We evaluate equation (21) at the free surface and apply the remaining boundary condition of vanishing tractions at the surface which requires that:

$$E_3(h^{(0)}) = E_4(h^{(0)}) = 0$$

where $h^{(0)} = 0$ and thus:

$$\begin{bmatrix} D_{11}^{(0)} & D_{12}^{(0)} \\ D_{21}^{(0)} & D_{22}^{(0)} \end{bmatrix} \begin{bmatrix} E_1(0) \\ E_2(0) \end{bmatrix} = \begin{bmatrix} 0 \\ 0 \end{bmatrix}. \tag{23}$$

The Rayleigh wave dispersion function, $_R\mathbf{F}(\omega,k)$, is equal to the determinant of the (2 X 2) submatrix of $[D]$ shown in equation (23) and clearly equation (23) can only hold if:

$$_R\mathbf{F}(\omega,k) = D_{11}^{(0)}D_{22}^{(0)} - D_{12}^{(0)}D_{21}^{(0)} = 0. \tag{24}$$

We find the eigenvalues by varying ω and k until the dispersion function is zero. For a flat layered medium the eigenvalues will form discrete curves in the (ω,k) space, which are the Rayleigh wave dispersion curves, for values of c less than the S-wave velocity in the half-space and for values of c greater than the S-wave velocity of the half-space the eigenvalues will form a continuous spectrum. We consider the frequency to be the independent variable and the corresponding wavenumber eigenvalues, for a particular frequency, ω, and for the nth mode, to be $_Rk_n(\omega)$. Thus,

$$_R\mathbf{F}(\omega,{_R}k_n(\omega)) = 0 \tag{25}$$

In order to compute the ellipticity, $_R\varepsilon_n(\omega)$, we evaluate equation (23).

$$_R\varepsilon_n(\omega) = \left. \frac{E_2(0)}{E_1(0)} \right|_{\omega,{_R}k_n(\omega)} = -\frac{D_{11}^{(0)}(\omega,{_R}k_n(\omega))}{D_{12}^{(0)}(\omega,{_R}k_n(\omega))} = -\frac{D_{21}^{(0)}(\omega,{_R}k_n(\omega))}{D_{22}^{(0)}(\omega,{_R}k_n(\omega))}. \tag{26}$$

The Eigenvalue Numerical Instability

So far we have followed the traditional Thomson-Haskell matrix formulation which has been used for many years to compute Rayleigh

dispersion curves At this point we diverge from the traditional approach which suffers from numerical instabilities at frequencies consistent with body wave synthesis. Recently, Abo-Zena (1979) has described a method by which the Rayleigh dispersion function can be computed without loss of precision at arbitrarily high frequencies and, briefly, the method can be described as follows.

If one were to algebraically expand the elements of the D matrix in terms of the transcendental functions, P and Q, given by equations (14) and then use this expansion in computing the dispersion function from equation (24), one would find that a number of these expansion terms would exactly cancel. Unless this cancellation is done explicitly before the dispersion function computation is coded in a digital computer program, then the cancellation will be done numerically in the chain of arithmetic executed by the computer. Unfortunately, these terms which cancel grow exponentially with frequency and at high frequencies they are so large that the terms which do not cancel are lost in the computer word roundoff. This is the source of the numerical instability in the Thomson-Haskell formulation and ...Abo-Zena has explicitly canceled these terms so that they never appear in the computer code.

In order to do this in a straightforward manner, Abo-Zena defines the Y matrix which we give here in terms of the previously defined D matrix.

$$Y_{jk}^{(p)} = D_{1j}^{(p)} D_{2k}^{(p)} - D_{1k}^{(p)} D_{2j}^{(p)} \quad \text{for } j,k = 1,2,3,4 \tag{27}$$

The elements of the (4X4) Y matrix constitute all of the possible sub-determinants of the D matrix of order two and clearly the Y matrix is anti-symmetric. We also note that from equation (24) it is obvious that:

$$_R\mathbf{F}(\omega,k) = Y_{12}^{(0)}(\omega,k) \tag{28}$$

As we shall see the Y matrix is also handy for computing the eigenfunctions. The Y matrix can be computed recursively at each layer interface using the following relation.

$$[Y^{(p)}] = [A^{(p)}(\xi^{(p)})]^T [Y^{(p+1)}] [A^{(p)}(\xi^{(p)})] \qquad (29)$$

The key to Abo-Zena's method is the way in which he computes this recursion relation and we refer the reader to his paper for the details.

Although Abo-Zena's method as given in his paper works very well to cure the dispersion function numerical instability, it does so at considerable expense over the Thomson-Haskell method in terms of computer time. We have carried out the algebra given by Abo-Zena further and have come up with a much more efficient algorithm which also retains the numerical stability. We omit the details of this rather tedious derivation and give the algorithm in the appendix. We might also point out that although Abo-Zena claims that his method is successful when using single precision arithmetic, our experience in using his method on a broad variety of structures and frequency bands indicate that in general one would be advised to use double precision arithmetic. This becomes more important as the structure depth or the number of layers increase and it is especially important when computing the eigenfunctions.

The Eigenfunction Numerical Instability: The Problem and the Cure

In order to synthesize Rayleigh waves for buried sources one must compute the eigenfunctions and these computations also exhibit numerical stability problems. Normally, one would find an eigenvalue by zeroing the dispersion function as computed by Abo-Zena's method. This value is then used to compute the ellipticity so that the surface values of the eigenfunctions are defined. The total propagator matrix to the desired depth is then computed and this matrix is used in equation (18) to

compute the eigenfunctions at the desired depth.

We tried this straightforward approach and found that in many cases the eigenfunctions became numerically unstable and the problem is more pronounced as the frequency is increased. Basically, what is happening is that small roundoff errors in the four eigenfunctions are effectively amplified by subsequent propagator matrix multiplications until the errors get bigger than the correct values of the eigenfunctions. These errors can be thought of as unstable, drifting errors with respect to depth since there is no inherent mechanism in the computations to stabilize them. Thus the computed eigenfunctions at half-space depths generally no longer meet the Sommerfeld radiation condition.

In order to illustrate this problem we use as an example the only structure for which we could readily obtain an exact analytic expression for the eigenfunctions, namely an infinite, homogeneous half-space. Using the propagator matrix from the appendix and replacing the hyperbolic trigonometric functions with the exponential functions P and Q, we can write the first displacement eigenfunction as follows.

$$E_1(z) = \frac{P(z)}{2}(-(\gamma-1) + {}_R\varepsilon_1\varphi\gamma) + \frac{1}{2P(z)}(-(\gamma-1) - {}_R\varepsilon_1\varphi\gamma) + \frac{Q(z)}{2}(\gamma - {}_R\varepsilon_1\frac{(\gamma-1)}{\varphi'}) + \frac{1}{2Q(z)}(\gamma + {}_R\varepsilon_1\frac{(\gamma-1)}{\varphi'}) \tag{30}$$

Where we have dropped the layer index and,

$$P(z) = \exp(\frac{\omega z}{{}_Rc_1}\varphi)$$

$$Q(z) = \exp(\frac{\omega z}{{}_Rc_1}\varphi')$$

and ${}_R\varepsilon_1$ is the ellipticity for the fundamental mode and ${}_Rc_1$ is the eigen phase velocity which, of course, is frequency independent. Since the value of ${}_Rc_1$ is less than the S-wave velocity of the half-space, the

functions φ and φ' are real and positive and thus the exponential functions P and Q have real and positive arguments. If we replace the ellipticity with an analytic expression in φ, φ', and γ we find that we can reduce equation (30) to:

$$E_1(z) = -(\gamma-1)\frac{1}{P(z)} + \gamma\frac{1}{Q(z)}.$$ (31)

The cause of the eigenfunction numerical instability can be seen when one compares equation (30) with equation (31). The Sommerfeld radiation condition requires that the growing exponential solutions vanish which of course is the case with equation (31). This comes about because the terms which multiply the exponential functions P and Q in equation (30) are identically zero. In order to show this one must substitute an *explicit* analytic expression for the ellipticity which in general is impossible to derive but for this simple case is easy to derive. If, however, one were to code equation (30) in a computer program to compute the eigenfunction, then the terms which multiply the growing exponentials would be computed numerically and instead of being identically zero, they would be of the order of the computer word roundoff error. These small but finite terms would then be multiplied by the growing exponential functions and at some depth the eigenfunction error terms would overcome the correct decaying solutions. Since the arguments of the functions P and Q are directly proportional to frequency, this numerical becomes more pronounced for a given depth as the frequency increases.

One can see from equation (30) that the type of algebraic cancellation used by Abo-Zena to eliminate the dispersion function instability can only be realized with the eigenfunction computations if an explicit analytic solution for the ellipticity can be derived. In general such an expression cannot be derived and so in general we are stuck with using

equation (30) or a more complicated version for a buried layer.

We were able to solve this problem by adding an additional constraint on the eigenfunction computations. From equations (21) we can see that they constitute a linear system of two equations in the four eigenfunctions and thus we can solve for two of the eigenfunctions in terms of the other two. We can express the two traction eigenfunctions in terms of the two displacement eigenfunctions as follows:

$$
\begin{bmatrix} E_3(h^{(p)}) \\ E_4(h^{(p)}) \end{bmatrix} = -\frac{1}{Y_{34}^{(p)}} \begin{bmatrix} Y_{14}^{(p)} & Y_{24}^{(p)} \\ -Y_{13}^{(p)} & -Y_{23}^{(p)} \end{bmatrix} \begin{bmatrix} E_1(h^{(p)}) \\ E_2(h^{(p)}) \end{bmatrix}
$$
(32)

In our search through the literature it appears that Duncan (1965) came up with a similar relation to equation (32), but he did not use it in the manner we have here to control *eigenfunction stability*. This relation can be used to compute the ellipticity in terms of the elements of the Y matrix which gives,

$$
_R\varepsilon_n(\omega) = -\frac{Y_{14}^{(0)}(\omega, _Rk_n(\omega))}{Y_{24}^{(0)}(\omega, _Rk_n(\omega))} = -\frac{Y_{13}^{(0)}(\omega, _Rk_n(\omega))}{Y_{23}^{(0)}(\omega, _Rk_n(\omega))}.
$$
(33)

In order to apply equation (32) to the half-space example problem we must divide the half-space into a number of pseudo-layers all of which have the same elastic parameters. *The procedure we follow to compute numerically stable eigenfunctions is as follows:*

(1) We evaluate the Y matrix at each pseudo-layer interface.

(2) The ellipticity is computed from equation (33) which defines the surface values of the eigenfunctions.

(3) We compute the two displacement eigenfunctions at the next pseudo-layer interface using the first two rows of the pseudo-layer propagator matrix.

(4) Equation (32) is used to compute the two traction eigenfunctions at the pseudo-layer interface instead of using the last two rows of the propagator matrix.

(5) Steps 3 and 4 are repeated to the desired depth.

The reason this method works is that implicit in equation (32) are the interface boundary conditions *and* the Sommerfeld radiation condition at the bottom of the structure. Assuming a small error exists in the displacement eigenfunctions which could come about due to the amplification of roundoff errors by the growing exponential propagator terms, then equations (32) effectively introduce small compensating terms in the traction eigenfunctions so that the factors which multiply the growing exponential terms stay small. Without such a correction the error terms grow exponentially with depth until they overpower the correct solutions. This method introduces a "feedback" mechanism into the computations which controls the error and insures that it stays small with depth.

We graphically show how well this method works in figures 2 and 3. The half-space problem we have discussed is shown in figures 2a, 2b, and 2c, which are plots of the vertical displacement and normal traction eigenfunctions as a function of depth at a frequency of five hertz. The S-wave velocity for this half-space was four km/sec and Poisson's ratio was 0.25. For each of the eigenfunctions there are two traces, the left hand trace is the computed eigenfunction plotted on a linear scale and the right hand trace is the difference between the computed trace and the exact solution from equation (31) plotted on a logarithmic scale. Figure 2a shows the numerical instability due to the growing propagator term which causes the eigenfunctions to "blow up" at about five km depth. As

can be seen from the error plots this instability is due to amplification of the initial error of about 10^{-15} which is the double precision roundoff error. In figure 2b we have placed a pseudo-layer interface at five km depth and then applied the eigenfunction stabilization method described previously. Although the eigenfunctions do not "blow up" they clearly are in error around five km depth and they are showing signs of instability once again at about ten km depth. In this case we have allowed the error to become large before we applied the correction at five km, but even in the case where the eigenfunction computations are obviously in error the use of equation (32) forces stability. From this figure we can see that the pseudo-layer thickness must be less than five km and in figure 2c we have used 2.5 km thick pseudo-layers. In this case the error never gets large and the use of equation (32) at 2.5 km intervals keeps the error small. These figures show that this stabilization method is only accurate if the error is not allowed to become large, i.e. the pseudo-layer thickness is below some critical value which will be inversely proportional with frequency.

From a practical standpoint we will not be very interested in computing eigenfunctions for a half-space and so we show computed eigenfunctions for a more typical structure in figures 3a, 3b, and 3c. This particular structure is two five km thick layers over a half-space and the eigenfunctions correspond to a high order mode at five hertz frequency. In these figures we have omited the error plots since there is no exact solution to compare against. Once again we show the computed eigenfunctions using the normal approach in figure 3a and as with the half-space case they "blow up" at about five km. In figure 3b we have applied equation (32) at the structural layer interfaces at five and ten km, but as

before we might suspect that the errors have become too large for accurate computations of the eigenfunctions at and below five km depth. We add two pseudo-layer interfaces at 2.5 km and 7.5 km and the results can be seen in figure 3c. If we continue to add pseudo-layers to the structure and make the pseudo-layer thicknesses smaller the resulting eigenfunctions do not change from those shown in figure 3c and thus we conclude that these computed eigenfunctions are good approximations to the exact solutions.

The Forced Vibration Problem - Source Excitation

The source z-dependent integrand functions, given by equations 9a, have the same form as the eigenfunctions, given by equations 10, 11, 12, 13, and 14, everywhere except at the source depth where a discontinuity in at least one of the functions is required. We follow Harkrider (1964) and define the source jump vector, $[\Sigma_m^{(s)}]$, as follows.

$$[\Sigma_m^{(s)}] = [S_m^{(s)}(\delta^{+(s)})] - [S_m^{(s)}(\delta^{-(s)})] \tag{34}$$

where

$$\delta^{+(s)} = \delta^{(s)} + \varepsilon$$

$$\delta^{-(s)} = \delta^{(s)} - \varepsilon$$

$\delta^{(s)}$ is the vertical source location measured from the top of the source layer and ε is a positive infinitesimal. Using the source jump vector we can relate the source integrand components at the top of the source layer to those at the bottom by:

$$[S_m^{(s)}(\xi^{(s)})] = [A^{(s)}(\xi^{(s)})][S_m^{(s)}(0)] + [A^{(s)}(\xi^{(s)}-\delta^{(s)})][\Sigma_m^{(s)}] \tag{35}$$

Applying the boundary conditions as with the eigenfunctions we can solve for the total solution z-dependent integrand functions, $[F_m^{(0)}]$, at the surface.

$$\begin{bmatrix} D_{11}^{(0)} & D_{12}^{(0)} \\ D_{21}^{(0)} & D_{22}^{(0)} \end{bmatrix} \begin{bmatrix} F_{1m}(0) \\ F_{2m}(0) \end{bmatrix} = -[D^{(0)}][Z(z_o)]^{-1}[\Sigma_m^{(s)}] \tag{36}$$

where

$$[Z(z_o)] = [A^{(s)}(\delta^{(s)})][\mathbf{A}^{(s-1,0)}] \tag{37}$$

and is the total propagator matrix from the surface to the source depth. The total solution functions, F, become eigenfunctions when the source jump vector is zero. We can solve for the surface values of the F vector in terms of the Y matrix.

$$\begin{bmatrix} F_{1m}(0) \\ F_{2m}(0) \end{bmatrix} = \frac{1}{Y_{12}^{(0)}} \begin{bmatrix} M_{1m} \\ M_{2m} \end{bmatrix} \tag{38}$$

where

$$\begin{bmatrix} M_{1m} \\ M_{2m} \end{bmatrix} = \begin{bmatrix} -Y_{12}^{(0)} & 0 & Y_{23}^{(0)} & Y_{24}^{(0)} \\ 0 & -Y_{12}^{(0)} & -Y_{13}^{(0)} & -Y_{14}^{(0)} \end{bmatrix} [Z(z_o)]^{-1}[\Sigma_m^{(s)}] \tag{39}$$

We can now write the integral equation for the displacements at the surface due to a buried point source. From equations 1, 3, and 38 and only considering the Rayleigh contribution, this gives:

$$_R u_1(r,\vartheta,0;\omega) = \sum_m \int_0^\infty \frac{M_{2m}}{_R\mathbf{F}} \left(J_{m-1}(k\,r) - \frac{m}{k\,r} J_m(k\,r) \right) e^{im\vartheta} k^2 dk \tag{40a}$$

$$_R u_2(r,\vartheta,0;\omega) = \sum_m \int_0^\infty \frac{M_{2m}}{_R\mathbf{F}} J_m(k\,r) \frac{i\,m}{r} e^{im\vartheta} k\,dk \tag{40b}$$

$$_R u_3(r,\vartheta,0;\omega) = \sum_m \int_0^\infty \frac{M_{1m}}{_R\mathbf{F}} J_m(k\,r) e^{im\vartheta} k^2 dk \tag{40c}$$

where

$$_R\mathbf{F} = Y_{12}^{(0)}(\omega,k)$$

The way by which one evaluates the integrals given by equations 40 is one of the major topics in theoretical seismology and in this paper we will approximate the integrals with the residue contributions due to the Rayleigh poles along the real wavenumber axis. Normally this approximation

would give good results only for the surface waves, but we will show how this approximation can be made to give good results for body waves as well with a slight modification of the structure. Thus, considering only the residue contributions, we can write the solutions to equations 40 as follows.

$$_R u_1(r,\vartheta,0;\omega) \;=\; -\pi i \sum_n \sum_m \left\{ \frac{M_{2m}}{\dfrac{\partial_R \mathbf{F}}{\partial k}} \left(H^{(2)}_{m-1}(k\,r) - \frac{m}{k\,r} H^{(2)}_m(k\,r)\right) e^{\,i\,m\,\vartheta} k^2 \right\} \Bigg|_{k \,=\, _R k_n(\omega)}$$

(41a)

$$_R u_2(r,\vartheta,0;\omega) \;=\; -\pi i \sum_n \sum_m \left\{ \frac{M_{2m}}{\dfrac{\partial_R \mathbf{F}}{\partial k}} H^{(2)}_m(k\,r) \frac{i\,m}{r} e^{\,i\,m\,\vartheta} k \right\} \Bigg|_{k \,=\, _R k_n(\omega)}$$

(41b)

$$_R u_3(r,\vartheta,0;\omega) \;=\; -\pi i \sum_n \sum_m \left\{ \frac{M_{1m}}{\dfrac{\partial_R \mathbf{F}}{\partial k}} H^{(2)}_m(k\,r) e^{\,i\,m\,\vartheta} k^2 \right\} \Bigg|_{k \,=\, _R k_n(\omega)}$$

(41c)

The cylindrical Bessel functions become cylindrical Hankel functions of the second kind due to the extension of the integration path to $-\infty$ along with the symmetry properties of the integrands (see).

We can further reduce equations 41 to a compact form which does not involve the propagator matrix to the source, $[Z]$, but instead depends on the eigenfunctions evaluated at the source depth. This was done by Harkrider (1964) and we omit the details here.

$$_R u_\alpha(r,\vartheta,z;\omega) \;=\; -\pi i \sum_m \sum_n \left\{ \Lambda_n(\omega)\,[\Sigma^{\bullet}_{mn}(\omega)]\,[F_n(z_o;\omega)]\,_R \widehat{\Psi}_{\alpha mn}(r,\vartheta,z;\omega)\,_R k_n(\omega)^2 \right\}$$

(42)

where

$$_R \widehat{\Psi}_{\alpha mn}(r,\vartheta,z;\omega) \;=\; F_{1n}(z;\omega)\,\widehat{\mathbf{P}}_{\alpha mn}(r,\vartheta;\omega) + E_{2n}(z;\omega)\,\widehat{\mathbf{B}}_{\alpha mn}(r,\vartheta;\omega)$$

(43)

$$\Lambda_n(\omega) = \left. \frac{Y_{23}^{(0)}}{\frac{\partial_R \mathbf{F}}{\partial k}} \right|_{k = {}_R k_n(\omega)} \tag{44}$$

$$[\Sigma_{mn}^{\cdot}(\omega)] = \left[\Sigma_{3m}^{(s)} \; \Sigma_{4m}^{(s)} \; -\Sigma_{1m}^{(s)} \; -\Sigma_{2m}^{(s)} \right] \Big|_{k = {}_R k_n(\omega)} \tag{45}$$

and $\hat{\mathbf{P}}$ and $\hat{\mathbf{B}}$ are modified vector cylindrical harmonics evaluated at the eigenvalues and are given by:

$$[\hat{\mathbf{P}}_{mn}(r,\vartheta;k)] = \left. \begin{bmatrix} 0 \\ 0 \\ H_m^{(2)}(k\,r) \end{bmatrix} \right|_{k = {}_R k_n(\omega)} \tag{46a}$$

$$[\hat{\mathbf{B}}_{mn}(r,\vartheta;k)] = \left. \begin{bmatrix} \dfrac{\partial H_m^{(2)}(k\,r)}{\partial(k\,r)} e^{im\vartheta} \\ \dfrac{H_m^{(2)}(k\,r)}{(k\,r)} \dfrac{\partial e^{im\vartheta}}{\partial\vartheta} \\ 0 \end{bmatrix} \right|_{k = {}_R k_n(\omega)} \tag{46b}$$

The Locked Mode Approximation

So far we have described how numerically stable spectra of flat layered earth normal modes can be computed for a point source at arbitrary depth and for arbitrarily high frequencies. At this point we address the problem of how one can use the residue contributions to approximate the complete integral solutions given by equations (40). We start by first briefly describing the properties of the integrand surface in the complex wavenumber plane.

Many researchers have investigated the wavenumber integrand functions of equations (40) (e.g. Ewing, Jardeztky and Press [19??], Aki and Richards [1980]). These functions are four valued due to the dual valued square root functions of phase velocity, $\varphi^{(N)}$ and $\varphi'^{(N)}$, in the bottom halfspace (see the Appendix). Thus the Riemann surface will be four leaved and branch points occur where $\varphi^{(N)}$ or $\varphi'^{(N)}$ are zero. We define branch cuts as the loci along which the real parts of φ and φ' are zero. Figure 4 shows the branch points, branch cuts and pole locations for real frequency and assuming no attenuation. We have omitted the mirror image in the second quadrant since the integrand topography in this region is not important for evaluating equations (40).

Our approach to solve the wavenumber integrals is to deform the contour of integration so that it encircles the poles and then use the residue contributions to approximate the solutions and we show the deformed contour as Γ in figure 4. We can replace the integrals from 0 to $+\infty$ with integrals from $-\infty$ to $+\infty$ by replacing the Bessel functions with Hankel functions of the second kind (Hudson[1969]). The contribution of the integration path at $|k| = \infty$ vanishes so that the wavenumber integral equations (40) are equal to the residue contributions given by

equation (42) plus a branch cut integral contribution which can be seen in figure 4.

We could eliminate the branch cut integral contribution by continuing the integration contour onto the other Riemann sheets in which case the contour would encircle the lower two quadrants four times before it would close. We would find additional residue contributions on the other sheets which would be located off of the real axis and these are the so called "leaking" modes (Gilbert [19??], Aki and Richards [1980]). If we were to include these leaking mode residue contributions we would have a complete and exact modal solution of equations (40) without having to evaluate any line integrals. Unfortunately these leaking mode poles are very difficult to locate and without the development of some efficient and reliable searching scheme these residue contributions are practically impossible to compute.

If we ignore the leaking mode contribution, the resulting synthetic seismograms will be missing the early part of the coda, namely the P-wave arrivals and the early S-wave arrivals. This is because the cutoff phase velocity is the S-wave velocity of the bottom half-space and the modes that propagate at higher velocities are the leaking modes which we have neglected. We could move the bottom of the structure down for some fixed range and for a realistic earth model this would result in increasing the S-wave velocity of the bottom half-space. As the cutoff phase velocity increases the branch point would recede towards the origin in the complex wavenumber plane and leaking mode poles that were near the original branch point location would migrate towards the real axis and pass through the branch point as it recedes to appear on the real wavenumber axis. These modes would thus be converted from leak-

ing modes to trapped or locked modes as the S-wave velocity of the bottom half-space increases and the resulting synthetic seismograms would contain earlier arrivals.

The essence of the locked mode approximation is to place an unrealistically high velocity half-space at the bottom of the structure and we refer to this high velocity half-space as the cap layer. We then require that this cap layer be placed at a depth such that the earliest P-wave reflection from the top of the cap layer arrive after the seismic coda of interest. As the S-wave velocity of the cap layer increases to infinity the entire seismic coda, including the earliest P-wave arrivals, can be synthesized using only the locked mode residue contributions. In the limiting case we can impose a boundary condition of total reflectivity at the top of the cap layer which is equivalent to specifying zero displacements along this interface. This changes the layered half-space problem into a layered plate problem and it causes the wavenumber integrand function to be single valued. Thus for the layered plate problem no branch cuts exist, there is only one sheet to the Riemann surface, a finite number of poles are located on the real wavenumber axis, and an infinite number of poles are located on the negative imaginary axis. (We might point out that the locked mode approximation is basically the same as the box normalization method which is well known in quantum mechanics ([]).)

There are a number of problems with the locked mode approximation which we will discuss in detail in following sections where we will show with numerical results how and under what circumstances these problems can be overcome. The problems fall into three categories which we list below.

1. Spurious reflections off of the cap layer

2. Time wrap around of the synthetic seismogram in the time domain due to sampling in the frequency domain

3. The truncation effects due to cuting off the mode sum to some finite number of modes (phase velocity filtering)

Computational Procedures

We have implemented the locked mode method as described in this paper on a DEC PDP11/70 minicomputer using FORTRAN computer programs. This computer has an available core size of 64K bytes (1 byte = 8 bits) for program instructions and 64K bytes for data. A high speed, large volume disk is also necessary in order to handle the rather large intermediate data files (these files are sometimes in excess of several megabytes in size). Single precision floating point variables are 32 bits long and have a numerical precision of about 8 decimal digits and double precision variables are 64 bits long with a precision of 16 decimal digits.

Because of the limited core space for both data and program instructions, we divided the computations into five separate computer programs which communicate via four intermediate data files. A brief description of each program and the data necessary to run the program is given below.

1. The first program searches for poles over some specified phase velocity range and for some fixed set of frequencies. Normally the frequencies are equally spaced from zero to some upper cutoff frequency so that the resulting spectra can be transformed to the time domain using a fast Fourier transform program without using any sort of spectral interpolation. The other input parameters are the

structural parameters which consist of the P-wave velocity, S-wave velocity, density, and thickness of each layer. We assume no attenuation at this point. The output from this program is a data file which consists of the eigen phase velocities of all of the modes within the prescribed phase velocity window and at the prescribed frequencies. In order to avoid numerical problems we found it necessary to do all of the arithmetic in double precision. The eigenvalue search constitutes the major expense in computer time and it also required the greatest amount of time to develop.

2. The second program computes the amplitude term given by equation (44), the group velocity, and the imaginary shift of the eigenvalue due to structural attenuation for each mode-frequency. The input eigenvalues are read from the data file generated by the first program and the only other inputs are the values of Q for each layer and at each frequency (it is quite easy to account for frequency dependent Q). We assume that the shift in eigenvalues due to Q can be approximated using first order perturbation theory. Thus the real part of each eigenvalue remains constant and the first order shift is purely imaginary (Archambeau and Anderson []). We compute $\partial_R \mathbf{F}/\partial c$ numerically (we found this to be the cheapest method) at the original real eigenvalue and for real P and S wave velocities, we then compute the dispersion function at the real eigenvalue but using the complex P and S wave velocities for each layer, and finally we apply a first order Taylor's expansion of the dispersion function to compute the imaginary shift of the eigen phase velocity. Once again all of the arithmetic for this program is done in double precision.

3. The third program computes a set of eigenfunctions for each mode-frequency. The input parameters are the depths for which the eigenfunctions are to be evaluated. This is the first point in the computational procedure where the source-receiver geometry is constrained since the source and receiver locations must be at depths corresponding to the computed eigenfunctions. All of the arithmetic is done in double precision, but the variables on the output file are stored in single precision. We found that subsequent computations could be done in single precision without undue adverse effects.

4. The fourth program computes the receiver displacement spectra for a given set of receiver locations and source parameters using equation (42). Input parameters are the range, azimuth, and depth for each receiver, source depth, and the source jump vector for each mode-frequency and for each value of m , the azimuthal index. All three components of the receiver displacement vector are computed for each receiver and the spectra are written on an output file. Phase velocity filtering, group velocity filtering, and mode number filtering are done at this point. All of the computations for this program are done in single precision.

5. The fifth program allows for seismic instrument convolution, spectral amplitude filtering, and computes the resulting time domain signal for each component of each receiver. A fast Fourier transform subroutine is used to transform the filtered spectrum to the time domain. Graphics software is used in this program so that the resulting synthetic seismograms can be displayed.

The first three programs are basically source independent (with the exception of the source depth) and, for a given structure, only the last

two programs need be executed to account for changes in source parameters or source-receiver geometry.

III.   Seismic Signal Detection and Analysis for Event Discrimination

III. Seismic Signal Detection and Analysis for Event Discrimination

A sophisticated form of signal detection/
analysis has been developed (Archambeau, et al.,
1981a) and is now incorporated in a new computer
program. We generally refer to the pro-
cedures involved in this time series analysis approach as
multiple-pass dispersion filtering (see next section for
details). The entire approach is based on quasi-harmonic
decomposition of the time series, using narrow band filtering
techniques, and is described quantitatively by Archambeau,
et al., 1981b. The approach has great flexibility in that,
when three component seismic data is available, both polari-
zation and wave number filtering can be carried out jointly
with the dispersion filtering to achieve a high degree of
selectivity for signal detection and a large amount of signal
information for all the signals detected. For regional data,
where a large number of seismic phases arrive close to each
other in time, it is not only desirable, but quite necessary,
to isolate individual phases and obtain good (uncontaminated)
estimates of the spectral content of each, their individual
arrival times and sense of first motion, and, ideally, also
their polarization, dispersion and wave number vector orienta-
tions as functions of frequency.

The new computer program developed has the capability
of performing the entire complement of signal detection/
analysis procedures mentioned. In the present framework, we
are employing it to: (1) generate the signal data needed to
define discrimination variables and location parameters for
regional events, and (2) to investigate the robust character
of candidate discrimination variables, using both real and
synthetic seismic data, as functions of noise levels, event
type and magnitude and structural variations. Ultimately,
we also expect to use this program to automatically generate

all the required discrimination variables to be used in a multivariate discrimination procedure for both regional and teleseismic events.

Figures 1 through 3 provide an example of the testing of this program for signal isolation and spectral analysis using regional synthetic seismograms. The objective here is to verify that the filtering correctly isolates regional type signal pulses in the presence of noise and obtains proper spectral estimates for each known signal pulse in the wave-train. Figure 1 shows predicted ground motion as a function of distance from the source, in the near-regional distance range. The source was chosen, for this test, to be an explosion at great depth (10 km), so that the synthetic seismograms would be relatively simple. The method used to generate the synthetics is the locked mode approximation devised by Harvey, 1981. The phases arriving coherently across this distance range can quite easily be identified, so that at a given distance, it is possible to identify particular reflected, re-fracted and direct phases. (Phase identifications can also be checked by theoretical ray tracing through the model velocity structure used.)

Figure 2 shows the results of adding seismic noise to the synthetic seismogram at 50 km from the source (top trace) and then processing the resulting time series through the dispersion filter procedure. In this operation, only pulse-like signals with little or no dispersion (i.e., body waves) are selected as signals of interest. The procedure involves ultra-narrow band filtering and generation of envelope and instantaneous phase functions from which the energy arrival times (group arrival times) and the spectral amplitude and phase at these times are measured and associated with the center frequencies of the narrow band filters. The desired undis-persed pulses are then selected by a pattern search in the
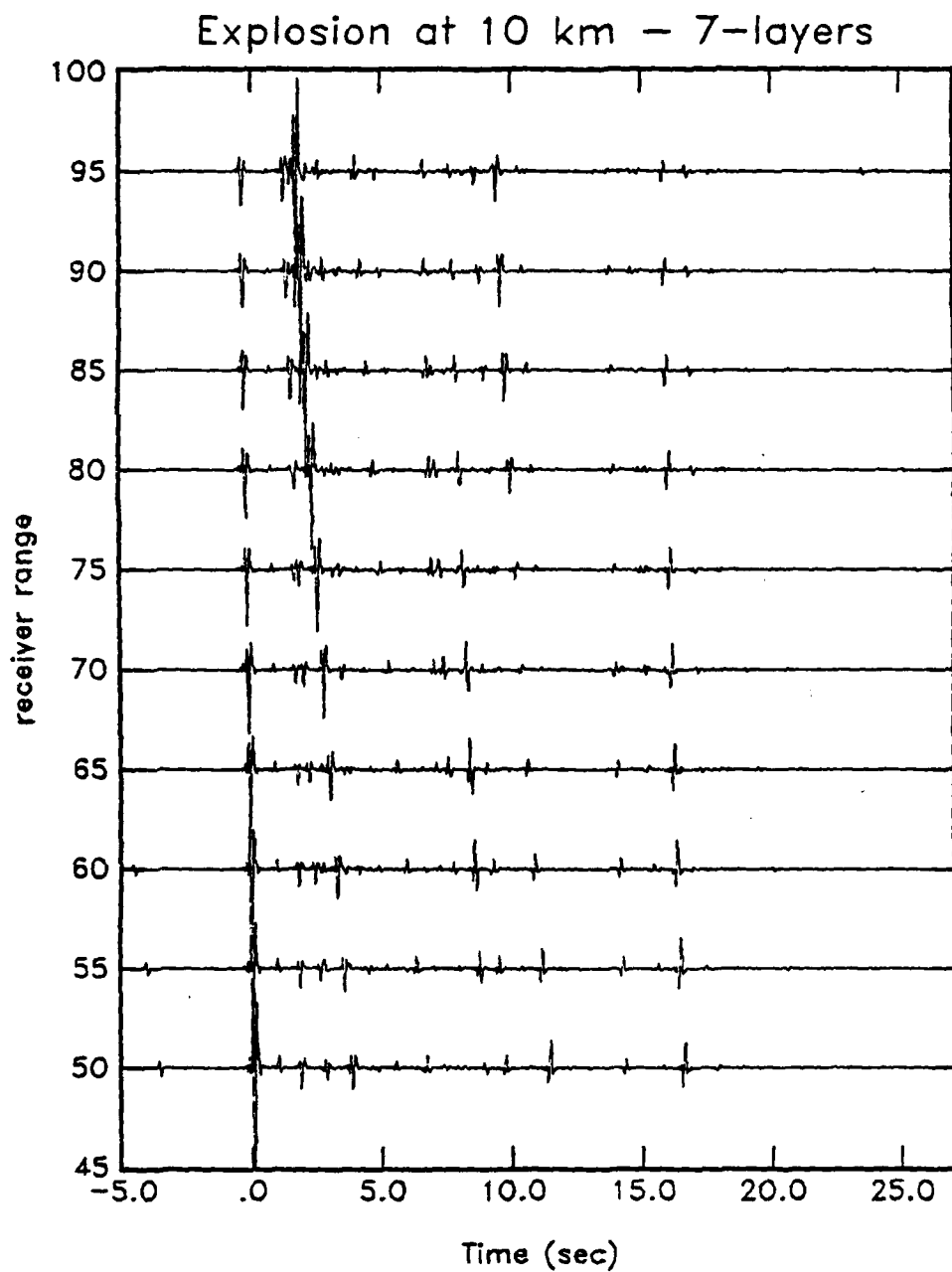
Figure 1. Synthetic near regional distance seismograms
generated by mode superposition, for testing
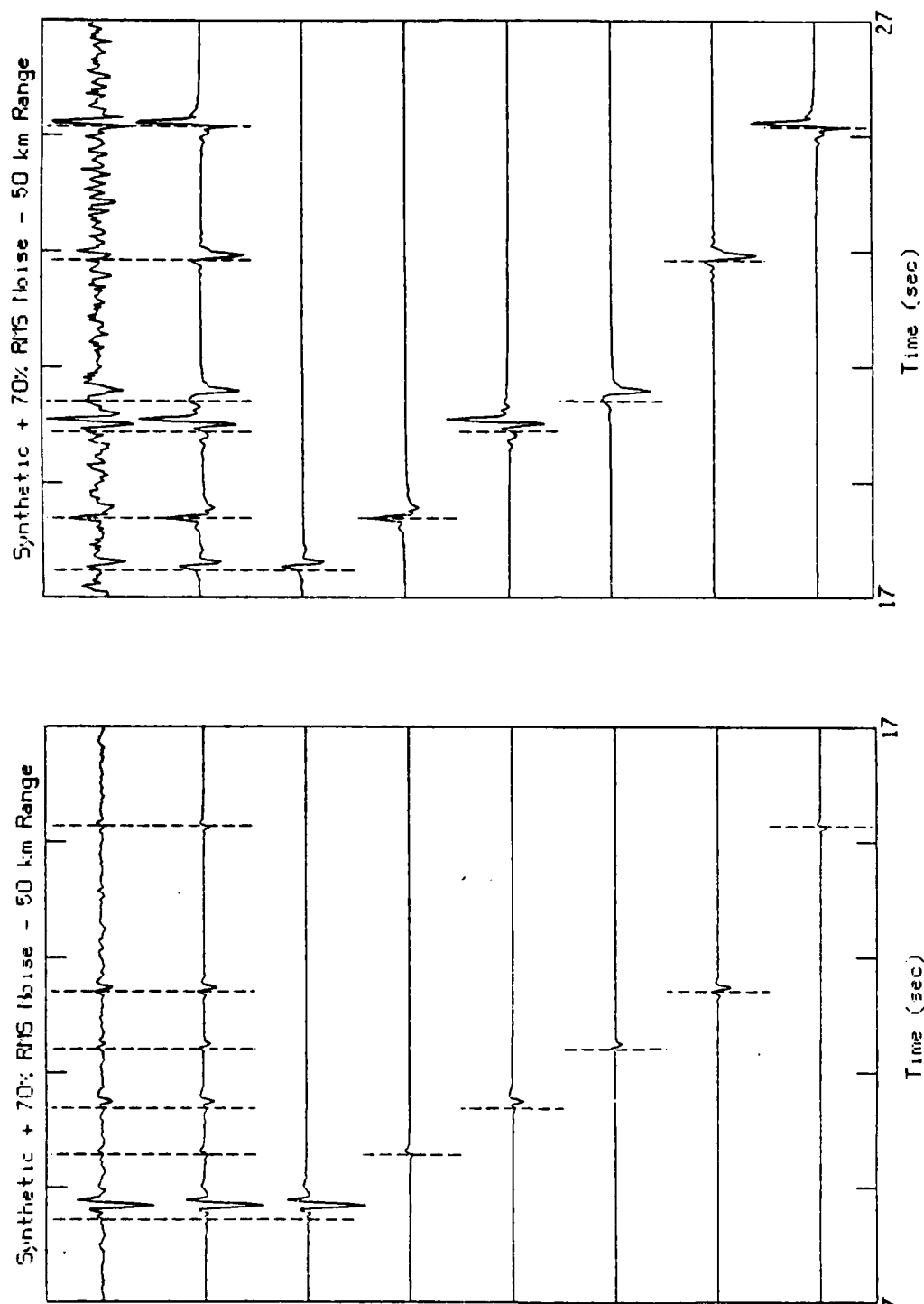of signal detection and analysis methods.

Figure 2.   Synthetic regional seismogram with seismic noise added for testing of
signal pulse isolation methods. The dotted lines denote automatically
determined signal pulse arrival times. The top trace is the original
data, the second trace is the superposition of the pulses obtained by
dispersion filtering and the remaining six traces are the isolated
pulse wave forms constructed from the pulse spectra estimated by QHD
methods. The synthetic seismogram corresponds to that shown in Figure
1 at a distance of 50 km.
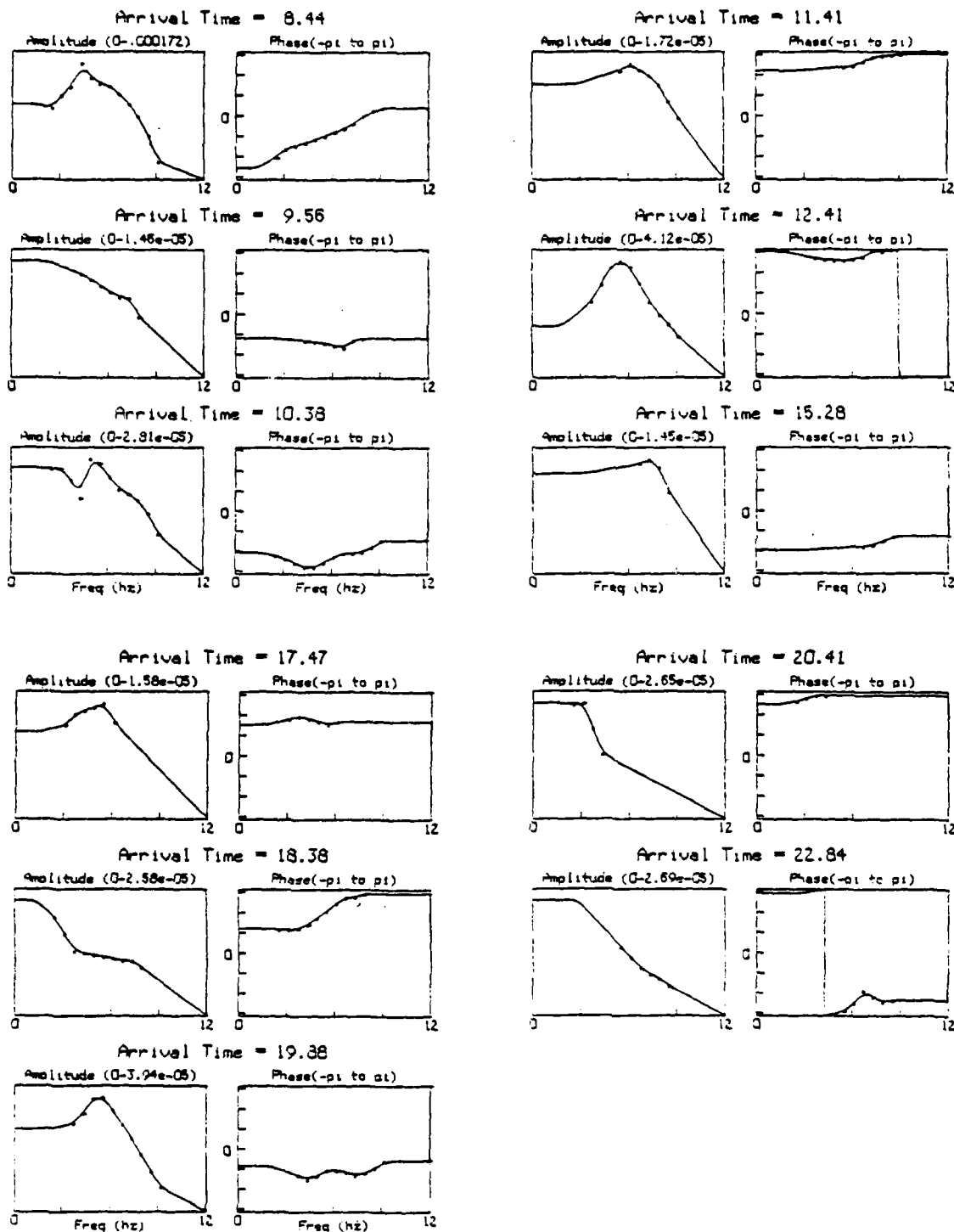
Figure 3. Signal pulse spectra as estimated by QHD filtering methods from the synthetic seismogram of Figure 2 The points are directly estimated from multiple narrow band filter output while the lines denote the interpolation-extrapolation of this data over the band 0 to 12 Hz.

frequency-time-amplitude parameter space, with those pulses having the proper dispersion and preselected frequency dependent signal-to-noise threshold level being selected. Pulses are selected, their spectra subtracted from the origin data and the resulting "reduced" origin spectrum is inverted to the time domain. The entire filtering and search process is then repeated. This procedure is continued until no new signal pulses are found. (This iteration procedure is the origin of the term "multiple-pass dispersion filtering.") Pulses obtained in this way may overlap in time, and it is possible to separate phases that are time shifted by only a fraction of their apparent period. On the other hand, if the pulses are significantly smaller than the uncertainty or resolution time of the narrow band filter, then they are automatically combined together (spectrally added) at the end of the iteration process to form a single pulse. The individual pulse spectra so isolated are then inverted to the time domain, as shown in the lower six traces in Figure 2. In the figure these may then be summed to give a single time series, as in the second from the top trace in the figure, which can be compared with the original. As can be seen from this comparison, the detection and isolation of the pulses by the filtering operations appears to be remarkedly accurate. This can also be verified by comparing the filtered output results with the original synthetic in Figure 1. Close examination shows that every significant pulse was detected and properly isolated with no false alarms. (One very weak arrival was, however, missed in the detection procedure, presumably due to its very low signal-to-noise ratio.)

Figure 3 shows the spectral estimates obtained for each of the pulses detected. That these spectral estimates are very reasonable estimates of the true spectra is apparent from the fact that when inverted to the time domain, they result in pulses that very closely match those of the pure synthetic, without noise.

In addition to the dispersion and spectral estimates of
the isolated pulses, it is also possible to obtain the "times
of arrival" of the phases. These are indicated by the dashed
lines in Figure 2, and the procedure is described and illus-
trated in a following section.

Figures 4 and 5 illustrate the application of the
procedure to a small regionally recorded earthquake from
Southern California. Only the first three seconds of the
time series is shown in Figure 5 and within approximately
a one second time interval five separate overlapping signal
pulses are detected. The separate pulse waveforms are shown
in the lower five traces, which have been inverted to the
time domain from the spectral estimates shown in Figure 5.
The sum of these pulses (second trace in Figure 4   is re-
markedly similar to the first second of the event recording.
The timing lines shown are computed in a manner designed to
indicate where the maximum of the early arriving energy occurs,
rather than at the signal pulse onset time.

Figure 5 lists the arrival times of the isolated
pulses and it is evident that they arrive within a few tenths
of a second from each other.

It is evident from these examples that we are in a
position to rapidly and accurately generate signal data,from
which event discrimination and yield or magnitude results may
be obtained. In particular, we clearly can measure frequency
dependent magnitudes over a wide band of frequencies for any
and all isolated phases. We can also automatically determine
arrival times and first motion data for all of the phases
quite reliably. We can, therefore, investigate spectral dis-
criminants for P_n, P_g, S_n, L_g, R_g, etc. and, as well, obtain
complexity measures, fault plane solutions and location and
source depth estimates using all the phase information in-
cluding S-P, pP, PP, etc.
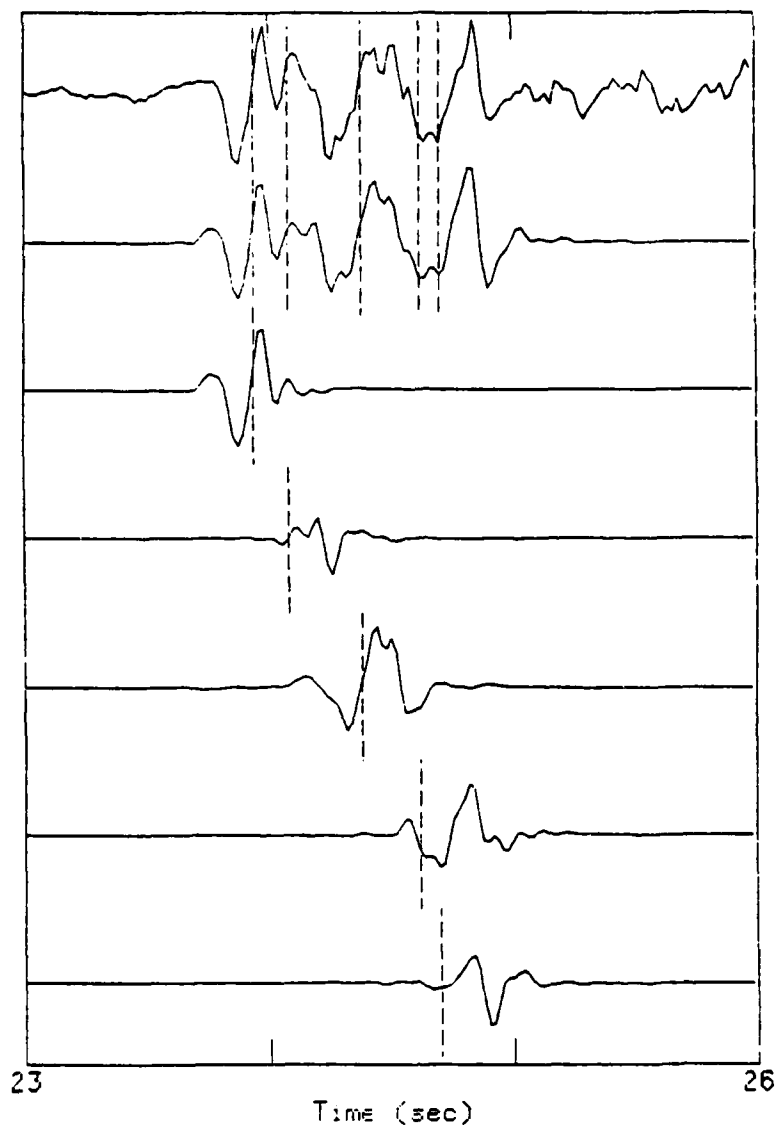
Figure 4.   Regionally recorded seismogram ($\Delta \sim 100$ km) and
signal pulses determined by multiple-pass QHD
methods employing dispersion filtering. The top
trace is the original earthquake data while the
lower traces are time series constructed from
the isolated pulse spectra. The second trace
is the superposition of the single pulse results.
The timing lines shown are determined automati-
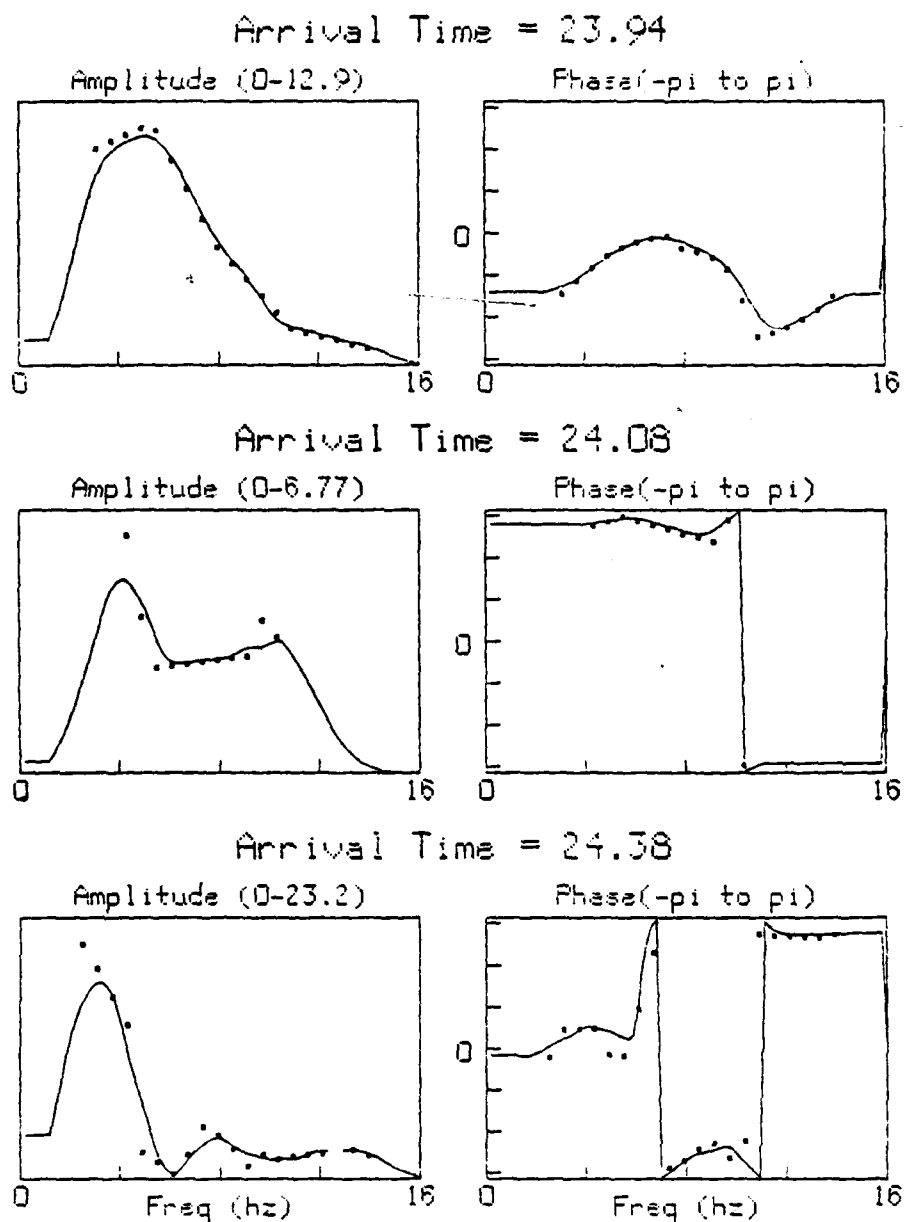cally from (weighted) mean group arrival times
for each pulse.

Arrival Time = 23.94

Amplitude (0-12.9)   Phase(-pi to pi)

Arrival Time = 24.08

Amplitude (0-6.77)   Phase(-pi to pi)

Arrival Time = 24.38

Amplitude (0-23.2)   Phase(-pi to pi)

Freq (hz)   Freq (hz)

Figure 5.   Signal spectra obtained by QHD analysis of the
             earthquake seismograms shown in Figure 4.   The
             points are directly observed spectral estimates
             from the envelope function maxima and the in-
             stantaneous phase at the envelope maxima times.
             These spectral estimates are used to construct
             the first three isolated time domain pulses
             shown in Figure 4.   The extrapolation criteria
             in the spectral domain requires zero spectral
             amplitude at zero frequency in order to obtain
             bandlimited results similar to those directly
             observed.

In this regard, we plan to form candidate discriminants, such as those mentioned earlier, and systematically test them against both real and synthetic regional seismic data.

In our applications to synthetic data, we expect to be able to verify, in considerable detail, the applicability and limitations of the various discriminants in a wide variety of situations by varying model structure, source type and noise conditions in a systematic manner. The realism of this approach can be gauged by noting how well complex regional seismograms can be predicted. For example, Figure 6 shows a layered model representing the crust-upper mantle in the region just east of the San Andreas fault in Southern California. Figure 7 shows the computed P-SV modes that are associated with this structure, by means of a phase velocity-frequency plot. Seismograms generated in the regional distance range from 300 to 450 km, from a shallow (1 km) depth explosion source, are shown in Figure 8. It is evident that the commonly observed complex features of the P_g wavetrain are present, as well as the simpler P_n phase. These seismograms are extremely similar to real data observed in the Southern California region, and it is clear that most, if not all, of the important characteristics of regional event data are represented. Thus, we can reasonably expect that definition of a robust discriminant based on tests with synthetic data of this sort will also apply to real data.

Southern California Structure
East of the San Andreas Fault
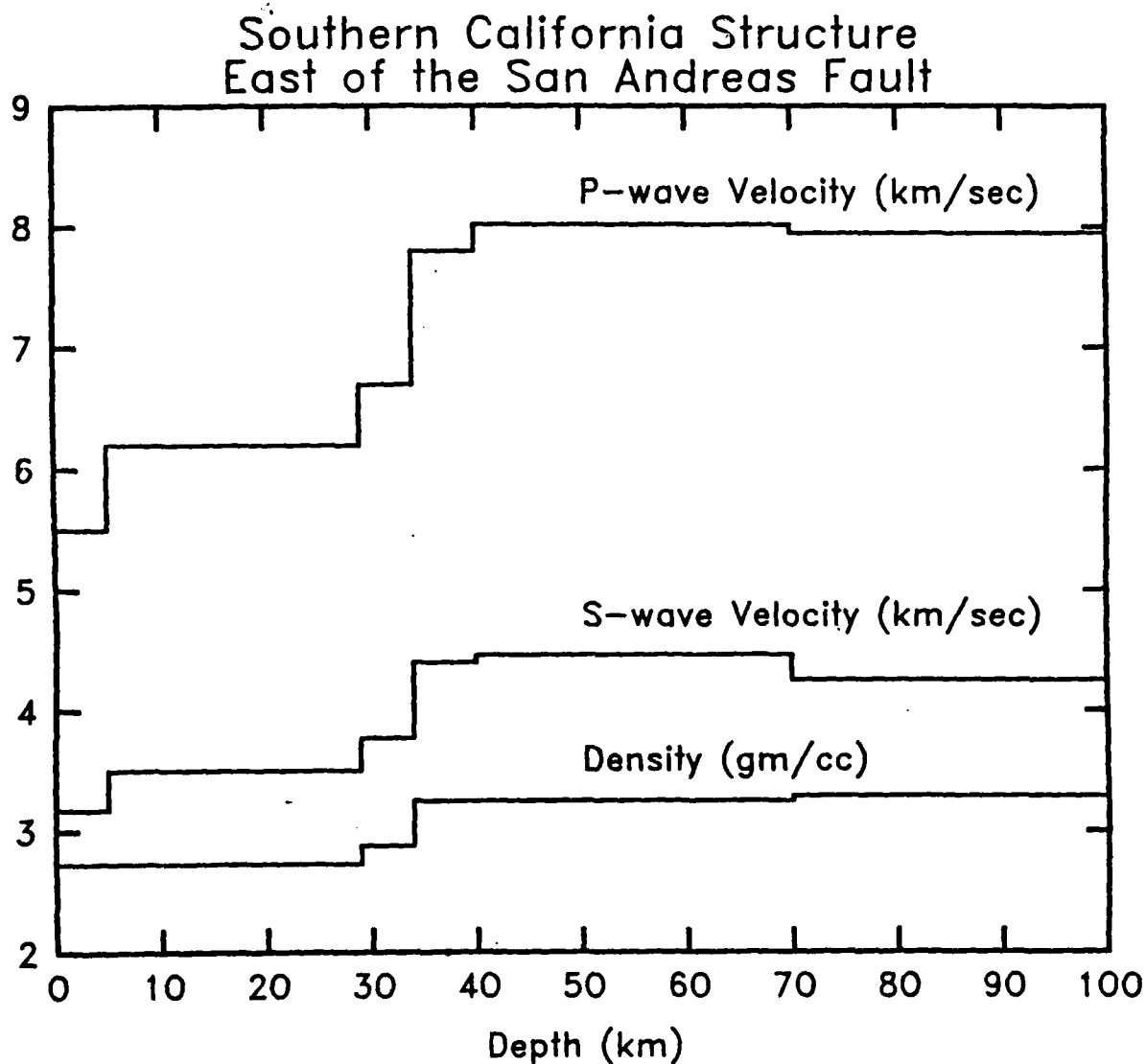
Figure 6.   Velocity-density structure representing the
Southern California region.
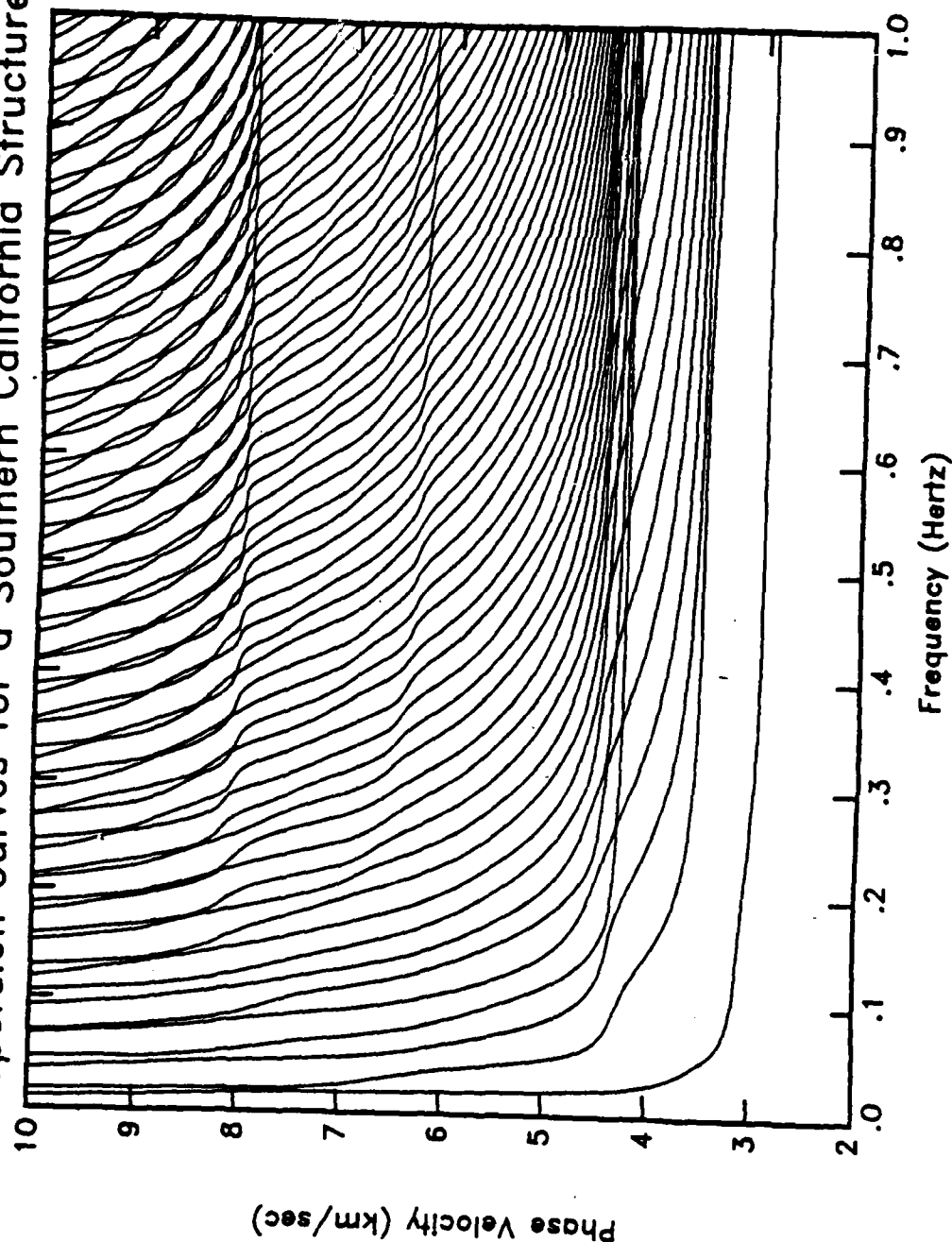
Figure 7. A section of the phase velocity dispersion curves for the Southern California structure. The prominent flattening of the higher mode curves near 4.6 km/sec, in the range near 6.2 km/sec and near 8.1 km/sec produce S, P_g and P_n body wave arrivals when the modes are summed.
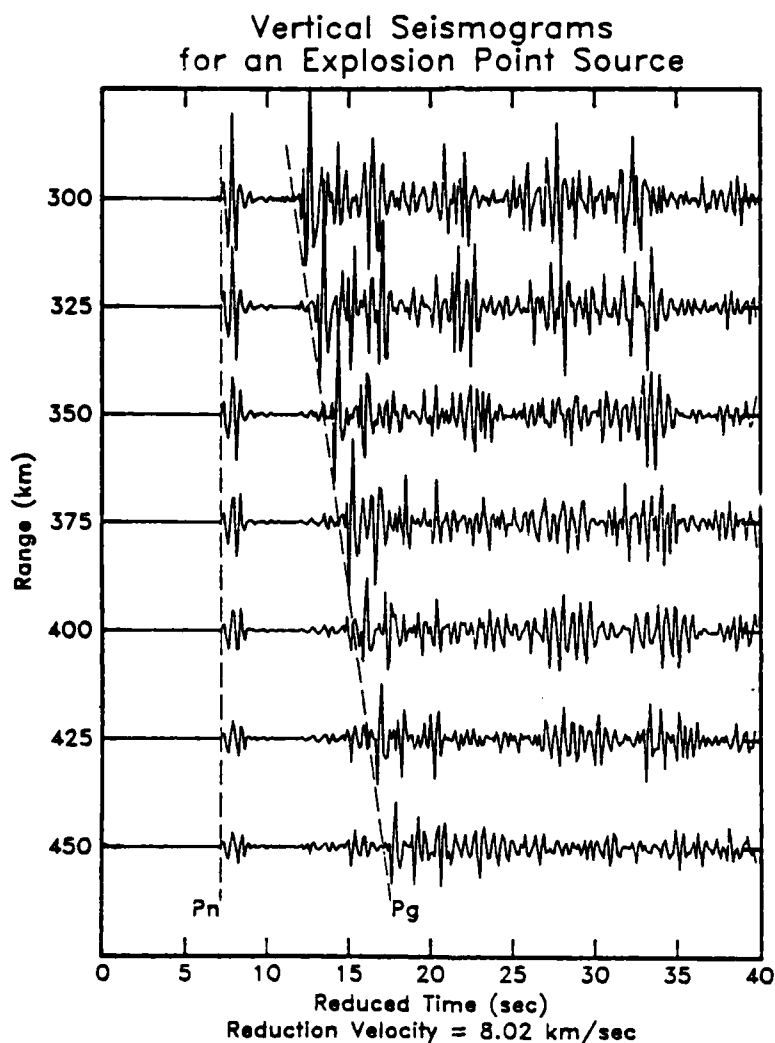
Figure 8. Regional synthetic seismograms generated by mode superposition for the Southern California area. The lines are theoretical travel times for P_n and P_g based on simple ray theory. The complex P_g wavetrain results from many higher mode contributions. Similar theoretical experiments show that a "P coda" is generated when thin, low velocity sedimentary layers are present near the surface. These synthetic seismograms are being used to define and test discrimination variables and methods.

Automated Signal Detection, Timing and Spectral Estimates Using Advanced QHD Methods

Inherently critical to the realization of an automated discrimination (and yield-magnitude estimation) procedure is the creation of a fast, sophisticated signal detection/isolation procedure and, coupled with it, related procedures for the accurate analysis of the signal data for spectral, waveform, and timing characteristics. The function of this system would then be to automatically provide the basic data to be used to define discrimination variables, such as those described in the earlier section.

In this section we will describe a currently operational, but newly developed, automatic system that is now being used to obtain the required signal and event detections and the basic signal date required for multivarient discrimination. The new system uses multiple-pass dispersion filtering as a principal method for the identification and isolation of signals, but also generates polarization and wave number data if three-component seismograms are available, and can use polarization and wave number filtering jointly with dispersion filtering to identify and extract signals from the time series. The entire approach is based on quasi-harmonic decomposition (QHD), coupled with amplitude pattern recognition in the time-frequency plane that can be created from the narrow band filter output used to perform the decomposition of the time series into a set of quasi-harmonic components. Specifically, energy arrival times are determined from the maxima in envelope functions generated from the narrow band filter set used. At these times, the envelope amplitude is proportional to the Fourier spectral amplitude at the center frequency of the filter for the signal (or noise) energy arriving, while the instantaneous phase, computed from the narrow band filter output at that time, is directly related to the Fourier

phase. Thus, for a large set of filters with different center frequencies, one can obtain a sample of the spectrum of the energy arriving within the time series window. This provides spectral data as a function of time throughout the time series. Further, when two or more displacement components are available, then the phase difference and amplitude ratios between the two components can be used to define and measure the polarization and azimuth/emergence angle (wave number vector orientation) associated with the wave field.

With such information it is possible to search for patterns in the group arrival time-frequency-amplitude parameter space for energy arriving with a particular dispersion characteristic and the required polarization, wave number vector and signal-to-noise ratio. For optimal estimates of the spectral and group arrival times, in the sense of maximum spectral accuracy and resolution in time, it is necessary to prefilter the time series with a matched filter having the inverse of the sought for amplitude and dispersion characteristics, so that in the resulting time series the signals of interest are pulse-like; that is they have rather flat spectra with little or no dispersion. In this case, all the signals of interest, including surface waves having initially strong dispersion, would have pulse-like character and the pattern search in the arrival time-frequency plane would always involve a search for undispersed energy arrivals over the frequency band covered bv the filter set.

An important feature of the analysis program
is a multiple-pass or iteration procedure. In this case,
pulse arrivals are selected throughout the time series using
the procedure indicated above. Then the pulse spectra esti-
mated from this "first pass" through the data are subtracted
from the spectrum of the entire time series. This reduced
spectrum is then inverted back to the time domain to produce
a "reduced" time series, wherein the previously detected
pulses have been removed. This new time series is then
reprocessed to generate new time varying spectral data and
the data is searched for additonal pulses satisfying the
fixed signal criteria. This process can then be repeated until
all "signals" have been detected.

Since there are normally overlapping arrivals in the
time series, it is common for one of the arrivals to over-
whelm the other or to interfere with it in such a way as to
make it violate the signal selection criteria on the first
pass. However, if the inteferring signal has been selected
and then removed (entirely or partially), it is usually the
case that the second signal can be detected and properly
identified, because of the reduction in interference. Further,
it is not possible to obtain totally precise spectral esti-
mates of any signal pulse on a single pass through the time
series, and so when the reduced spectra for the entire time
series is inverted to the time domain there is always a
residual part of the detected signal pulse remaining. This
residual is usually detected as "another" signal on the next
pass through the data, if it is above the background noise
level. Hence it is possible to recover more of the signal
by repeating the selection process on the reduced time series,
as well as to recover neighboring signals that were missed due
to interference effects.

Thus, the reduction procedure is repeated over and over again until no pulses satisfying the (fixed) signal criteria are found. At this stage the process terminates. However, because of the possibility of repeated detections of the same signal, as just described, it is necessary to consider detection associations designed to combine together (add) the spectra of pulses detected within the same small time window. The size of the window within which all detections are considered to be the same signal is taken to be proportional to the resolution time for the narrow band filters used.

Once all the associations are made, then the remaining distinct seismic pulse spectra can be synthesized into the time domain individually, to give each pulse waveform in complete isolation from the noise and other pulses detected. The superposition of the individual pulses then should give an "uncontaminated" seismogram, which can be compared to the original; in quantitative terms by a cross correlation.

Because the pulses can be completely isolated in the time domain, it is also possible to time them, that is to obtain the "time of first motion." The first motion time can be obtained by a variety of methods, but the most stable procedure is to form the individual pulse envelope functions and use the time of the first inflection in the envelope as the pulse arrival time. Further, the sense of first motion can also be simply obtained once the first motion time is determined, by measuring the algebraic sign of the displacement immediately after the first motion. These operations are included in the QHD program and are designed to provide automatic timing information for location purposes and fault plane solution data for network discrimination.

Figure 9 illustrates the multiple-pass dispersion filtering operation for a regionally recorded small earthquake. The multiple-pass, reduced time series are denoted

TIME (sec)
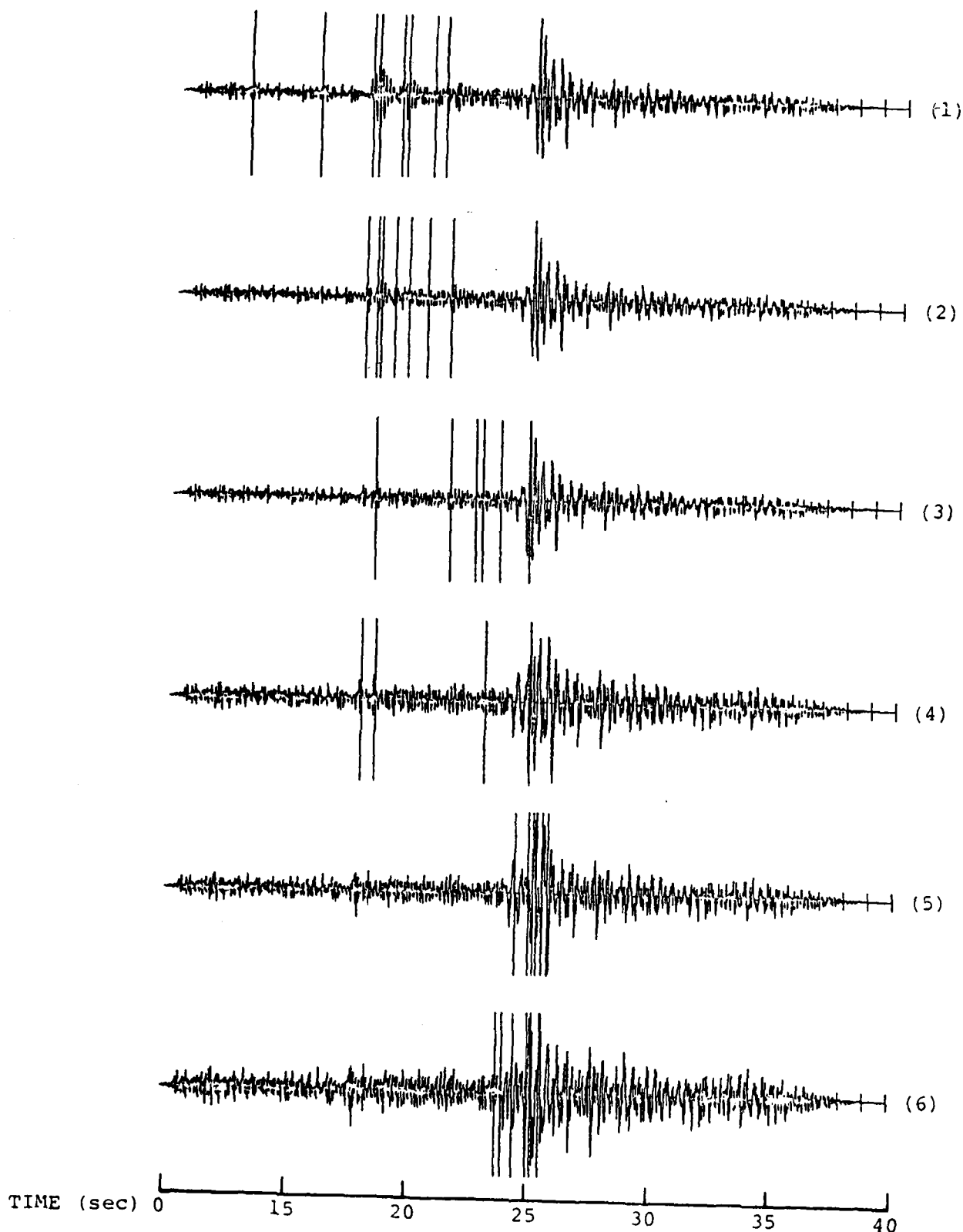
Figure 9. Multiple pass extraction of signal pulses using QHD procedures for a Caltech recorded small earthquake ($\Delta = 52$ km).

(1) through (6) in the figure, with (1), of course, being the
original seismogram. The first arrival from the event is near
the 17 second time point in record (1).. The multiple passes,
in this example, were designed to isolate the earliest arriving
pulses having nondispersive character — that is having body
wave characteristics. Thus, the multiple processing will first
find signals at the left of the figure and progressively work
to the right until all signals, satisfying the particular
criteria used here, are found.

The dotted lines in the figure denote first motion times
for each signal pulse detected. Clearly two "false alarms" are
obtained during the first pass, since they occur before what
we know to be the first arrival from the event. (These can be
eliminated, of course, by adjustment of the detection criteria
parameters.) On the other hand, the first arrival pulses are
properly detected, along with several clear late arrivals. The
reduced seismogram obtained by removing the detections obtained
in (1) is shown as trace (2), along with the additional pulse
detections. Similarly, trace (3) is the reduced seismogram
with all the detections of the first and second passes sub-
tracted. Again the detections obtained are shown, with the
additional detections appearing later in the seismogram. The
remaining traces are similarly reduced seismograms and show
progressively later pulse detections as the early signals are
reduced to noise level. (Since the seismograms are individually
normalized to unity for the largest amplitude, for plotting
purposes, it appears that the noise level increases from trace
(2) to trace (6). This, of course, really just means that the
signal level is being continuously lowered by the reduction
process toward the noise level.) The process automatically
terminated after the sixth iteration, with no remaining sig-
nals detected.

Figure 10 shows an expanded time scale representation
of the final results for the event shown in Figure 9. The

Time (sec)
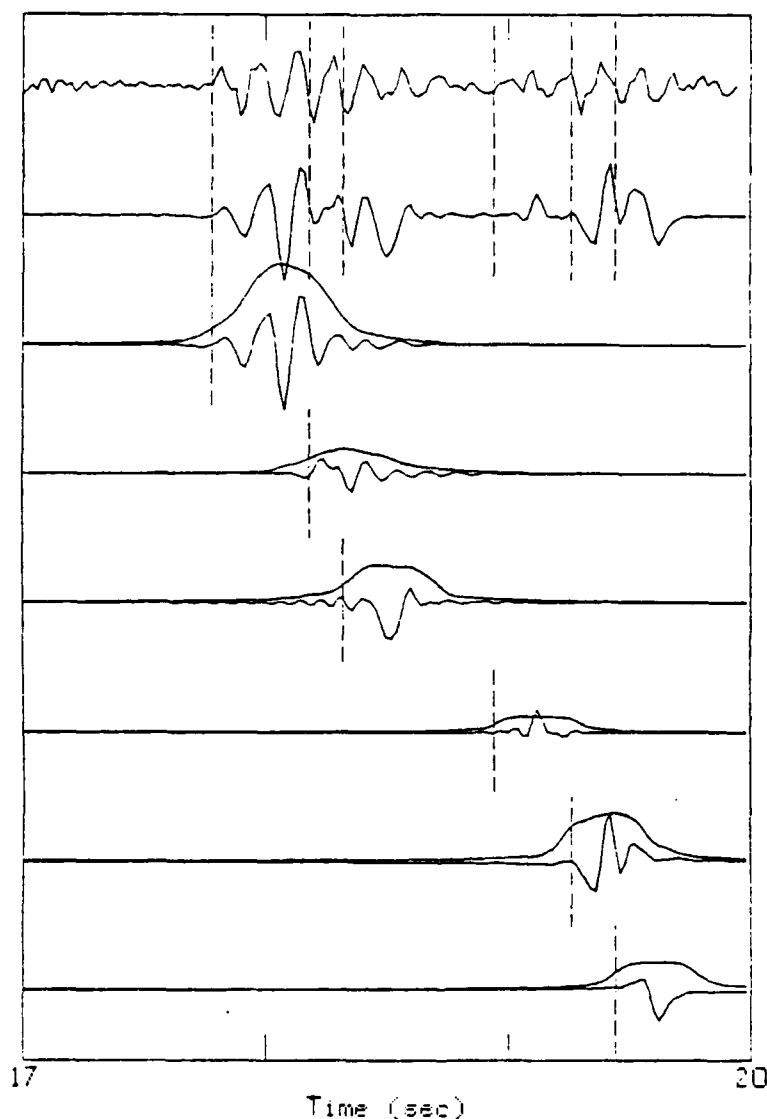
Figure 10. Automated pulse decomposition of an observed re-
gional distance range earthquake (top trace) using
QHD based dispersion filtering. The second trace
is a superposition of the single pulses obtained
by the decomposition method. The isolated pulses
are shown in the lower six traces. Also shown
with the single pulses are their individual enve-
lope functions, which are used to define the pulse
arrival times. The arrival time is taken to be at
the time of the (first) inflection point in the
envelope function. The variation of the signal
pulse amplitude immediately after this time is
then used to determine the "sense of first motion"
of the pulse.

Arrival Time = 17.78

Amplitude (0-321)   Phase(-pi to pi)

0   16   0   16

Arrival Time = 18.18

Amplitude (0-70.7)   Phase(-pi to pi)

0   16   0   16

Arrival Time = 18.32

Amplitude (0-96.6)   Phase(-pi to pi)

0   Freq (hz)   16   0   Freq (hz)   16
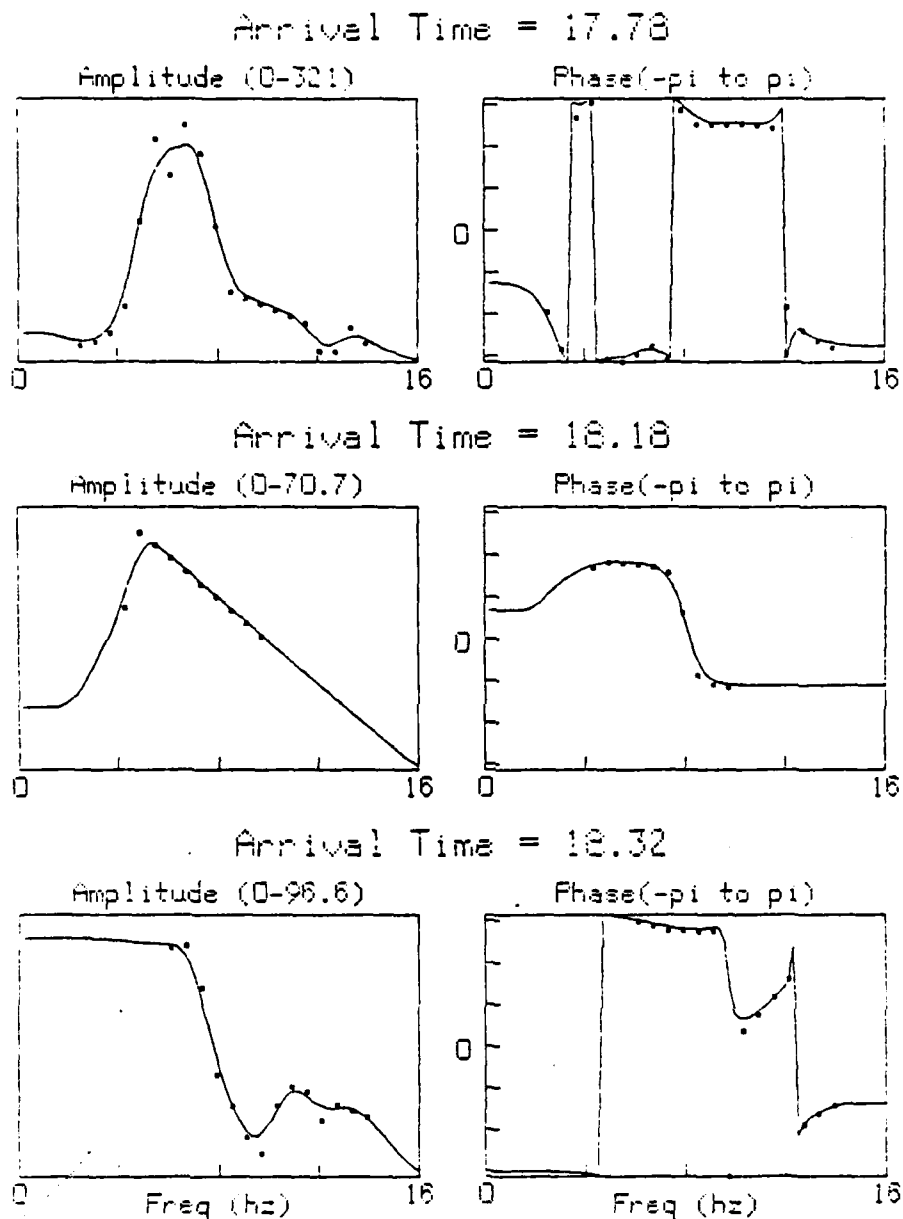
Figure 11.   Spectral estimates of isolated signal pulses from
             the California earthquake shown in Figure 10. The
             points correspond to spectral data obtained from
             the narrow band filters employed. The lines repre-
             sent interpolation-extrapolation of the data such
             that there is automatic smoothing and extrapolation
             to flat spectra near zero frequency (far field
             representation of the pulses).

first six signal pulses after the first arrival are shown,
along with the original seismogram (top trace) and the super-
position of the isolated pulses obtained (second trace from
the top). The envelope functions for the individual pulses
are also shown, along with the first motion timing lines that
are automatically determined from the envelope inflection
points.

Figure 11 shows the spectra for the first three pulses
shown in Figure 10. It should be noted that the program auto-
matically extrapolates the spectral data in such a way as to
give a far field representation for each pulse, and this is
not directly comparable to the original seismogram, which is
band limited. However, comparison of the top two traces in
Figure 10, nevertheless, shows strong similarity between the
original and the reconstructed seismograms.

As was implied earlier, and is demonstrated by this
example, the procedure is capable of separating very closely
time spaced pulses. This is evident from the arrival time
differences listed with each signal spectrum in Figure 11,
where signal arrivals are only separated by 0.4 and 0.14
seconds.

IV.   Theoretical Basis for Event Discrimination Using m_b vs M_s

In order to provide a theoretical basis for m_b vs M_s type discrimination we have generated synthetic seismograms at teleseismic distances from earthquake and explosion source models in representative earth structure models. The appropriate way to do this is to generate synthetic seismograms in the time domain and to directly measure magnitudes from the predicted signals at a large number of azimuths and distances and to obtain averages in the same manner as is done in generating observed magnitude data. We have used stress relaxation source models for the earthquakes. (e.g. Archambeau, 1964, 1968; Archambeau and Minster 1978) and explosion models based on numerical calculations (e.g. Cherry et.al. 1972) and imperically derived explosion source models based on near field observations (Mueller and Murphy, 1971).

Since the earthquake data to be analyzed will represent, in general, events occurring in both oceanic and continental tectonic environments, it is necessary to obtain theoretical results for earth structures representing both tectonic continental and oceanic upper mantle characteristics. We have used the continental structures for tectonic areas obtained by Archambeau, Flinn, and Lambert (1969) as well as a modified version of the anelastic Q structure obtained in this same study for the body waves. The surface wave anelastic structure was adopted from the MM8 model of Anderson and Archambeau (1964). The oceanic velocity model used was based on that given by Toksoz and Anderson (1962), with the Q model modified from the continental model in a manner consistent with the differences between island arc oceanic (see, Barazanzi et. al. 1975) and tectonic continental mantle velocity distributions. That is, the low Q zone was made to correspond to the low velocity zone in the model.

In addition to the necessity of generating synthetic time series for different mantle structures, it is also clearly necessary to vary the source depth and the failure zone orientation with respect to the free surface, inasmuch as these variations will have important effects on the magnitudes observed. Thus three "types" of events were considered: 45° thrust earthquakes, normal dip slip earthquakes and (90°) strike slip earthquakes. Theoretical seismograms were then generated for these basic event types at five separate depths (10 km, 15 km, 25 km, 35 km, and 45 km) in either an oceanic or a tectonic continental environment. In addition the rupture velocity was varied with depth since all the events used a rupture rate equal to .8 of the local shear velocity, which was different in the two structures used and different at different depths. Finally, of course since we wish to generate theoretical results relating body and surface wave magnitudes to stress drop and rupture zone dimensions, both of these source variables were varied for the different events. In particular, event length dimensions of 1 km, 2.5 km, 5 km, and 10 km were used with each event type, as well as event stress drops of .001 kb, .01 kb, .1 kb and 1 kb. All these variations of structure, event type, depth and failure parameters resulted in the generation of a very large number of synthetic seismograms of course.

The theoretical event magnitudes m_b and M_s were obtained from the synthetic seismograms using the conventional, and rather imprecisely defined, procedure for the measurement and computation of magnitudes. However, only the .05 Hz surface wave magnitude was obtained, in view of the variability of M_s with frequency, and so comparison of the theoretical results to observations requires the use of M_s data observed at .05 Hz. Since this has now become essentially standard observational procedure, this

presents no particular difficulties. Similarly, only the vertical component M_s was generat d, since this is now the standard measurement, but the radial component M_s value can be easily obtained by multiplication of the vertical amplitudes by the appropriate ellipticity factor.

The theoretical magnitude data generated by this rather massive computational effort is illustrated, in one particular form in Figure (12) through (14).

These figures show the theoretical body and surface magnitudes for the three basic event types as functions of depth, with event rupture dimension as a parameter, and for the two basic mantle structures used. The stress drop for the events was at a fixed 100 bar level. These three figures together constitute the entire theoretical m_b and M_s set for the events having a fixed 100 bar stress drop. For events with larger or small stress drops the magnitude scale is simply shifted linearly. That is, since source spectral amplitude scales linearly with stress drop, then for 1000 bar stress drop events the magnitude scale would change by the (base ten) log of the ratio of the 1000 to 100 bar stress drop magnitudes, or by one magnitude unit. Hence for 1 kb stress drop events, the magnitude scale can simply be increased by one unit and the proper predicted m_b and M_s values would be obtained. Hence these figures contain essentially all the magnitude information generated.

The important characteristics of these results, especially for the applications intended, are first that the body wave magnitude shows little variation with event hypocentral depth and essentially no variation between continental and oceanic structures. This is, of course, highly desirable for purposes of source property inversion and event discrimination based on these parameters. Second, as expected, the M_s results shown systematic
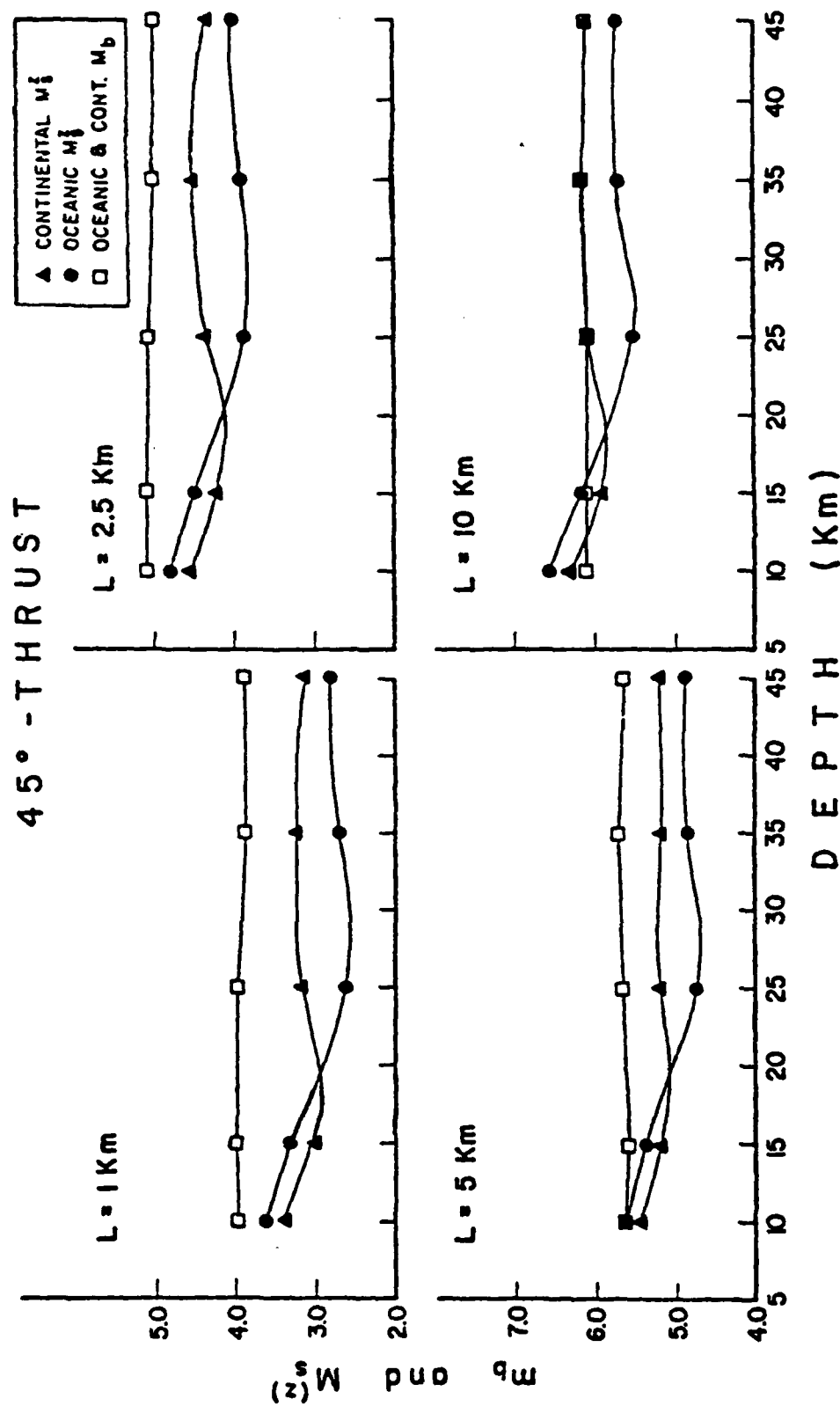
Figure 12. Theoretically computed m_b and M_s values for thrust type earthquakes of four different rupture dimensions (L = 1 to 10 km), located in different source structures and at variable focal depths.
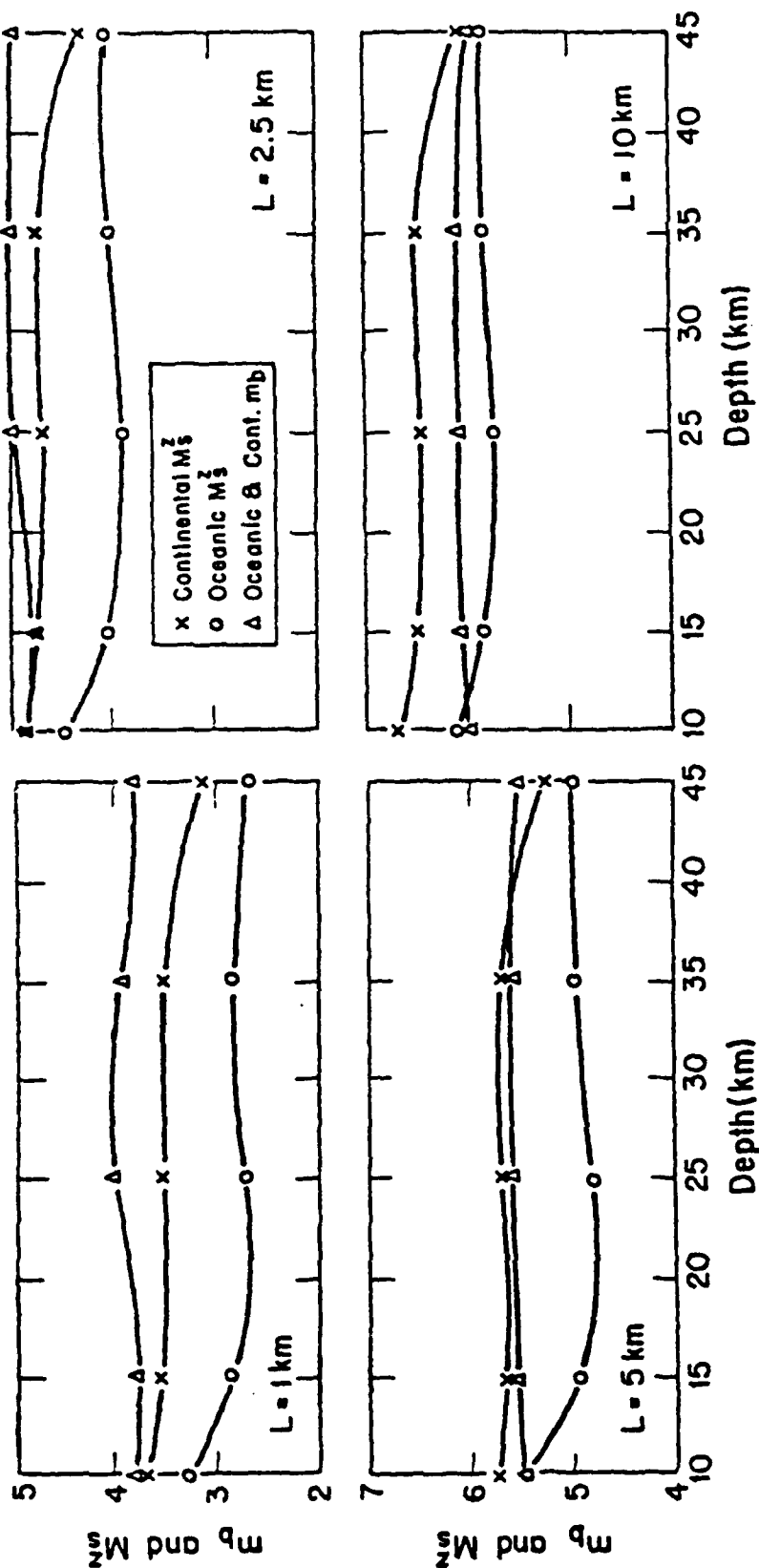
Figure 13. Theoretically computed m_b and M_s values for normal faulting earthquakes as a function of rupture dimension, source structure and focal depth.
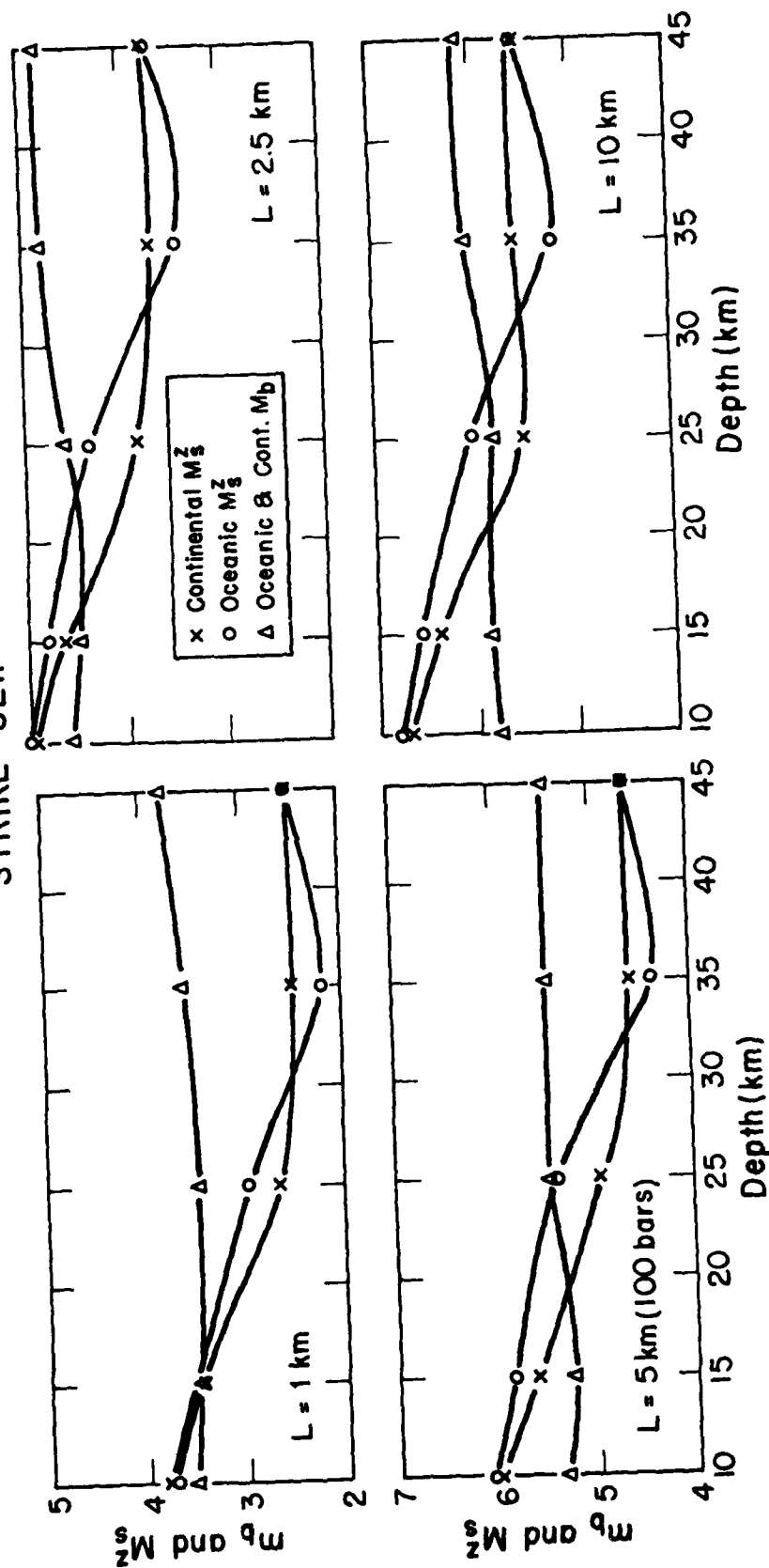
Figure 14. Theoretical m_b and M_s values for strike-slip earthquake faulting as a function of rupture dimension, source structure and focal depth.

differences in continental versus oceanic structure and a rather strong

variation with depth in the hypocentral depth range 0 to 20 km, in both

structures. However the M_s variation with event depth in the range from,

somewhat less than, 20 to 50 km is mild and the curves are, in fact, very

near flat at a constant M_s level. This is very important for source

parameter inversion using M_s data, since it is highly desirable that the

data be strongly dependent on only the source parameters of interest

(stress and rupture dimension) and essentially independent of depth in

particular, since hypocentral locations are usually uncertain to at least

20 to 30%. Thus, we see that because of the rather fortunate circumstance

that neither M_s nor m_b values are very sensitive to hypocentral depth in

the range from about 15 to 50 km, we can expect to largely avoid uncertainties

in stress estimates arising from source depth uncertainties for events in

this depth range. Thus only for events in the 0-20 km depth range is it

likely that depth is a critically important factor.

The appropriate form of the theoretical magnitude results is as a set

of theoretical curves in a plot of m_b versus M_s value. A set of continuous

curves of this sort can be easily generated by interpolating the (m_b, M_s)

results obtained, using fault dimension and stress drop as parameters for

the curves. The set of Figure (15) through (18) give examples of such

curves for 45° thrust and normal dip slip events along with observed data

from the Alaskan-Aleutian Arc region. The Appendix 3 contains the entire

set of theoretical m_b vs M_s curves for both oceanic (Island Arc) and Tectonic

Continental origins, for all the source types over the source depth range

0-45 km. The lines labeled 1 km 5 km, etc., are the loci of events in this

M_s vs m_b plane having constant rupture dimension, but variable stress drop.

The curves labeled .001 kb, .01 kb, etc., are the loci of events in the
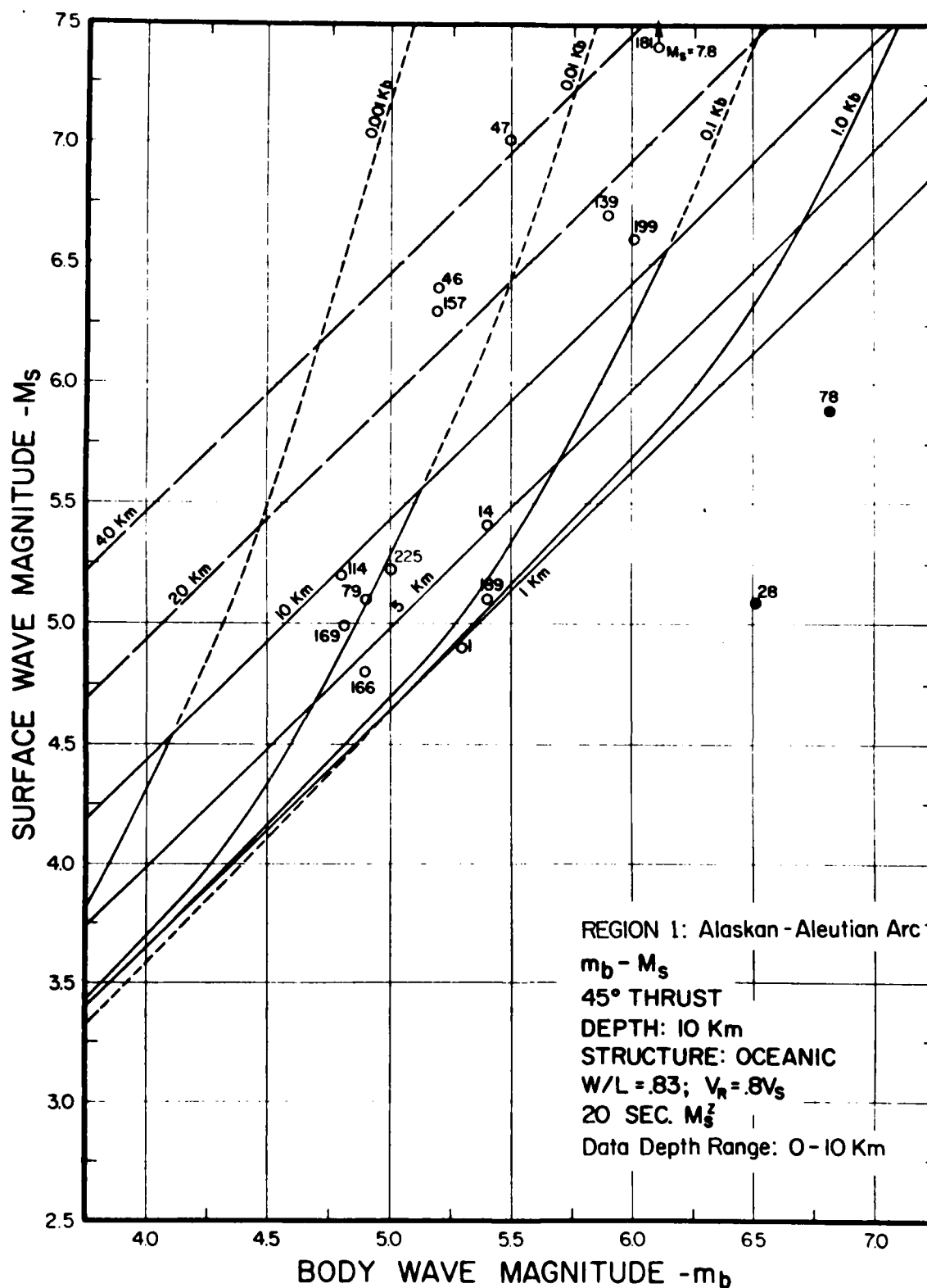
Figure 15. Surface wave magnitude M_S versus body wave magnitude m_b, showing event data in the depth range 0-10 km from the Aleutian-Alaskan region. The curves are theoretically predicted for thrust type events in this depth range and are used to estimate stress drop and rupture dimensions for the observed events. The solid circles are explosions.
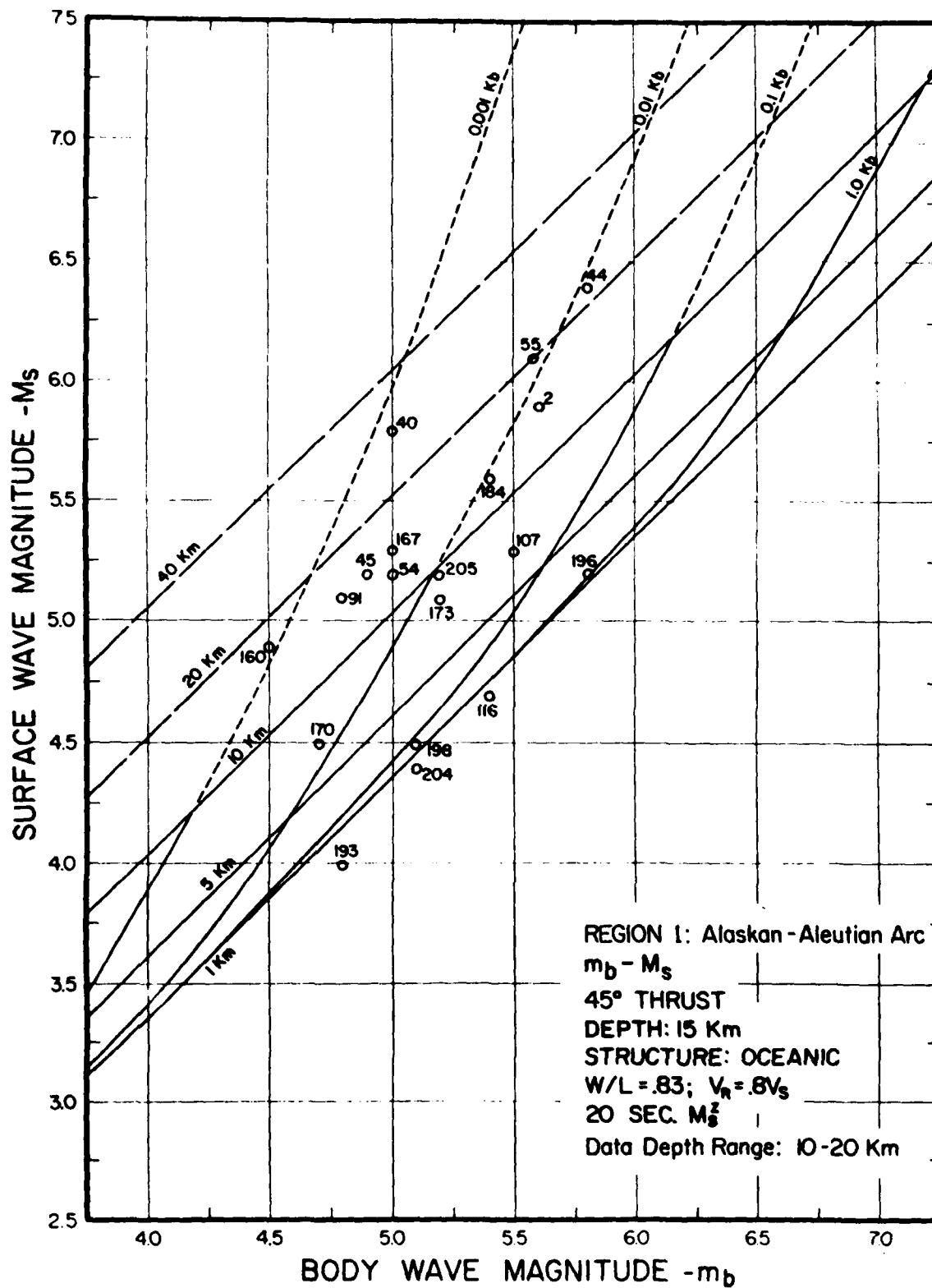
Figure 16. Surface wave magnitude M_s versus body wave magnitude m_b, showing event data in the Alaskan-Aleutian region for the depth range 10-20 km. The theoretical curves are for a 45° thrust event at 15 km with variable stress and dimension.
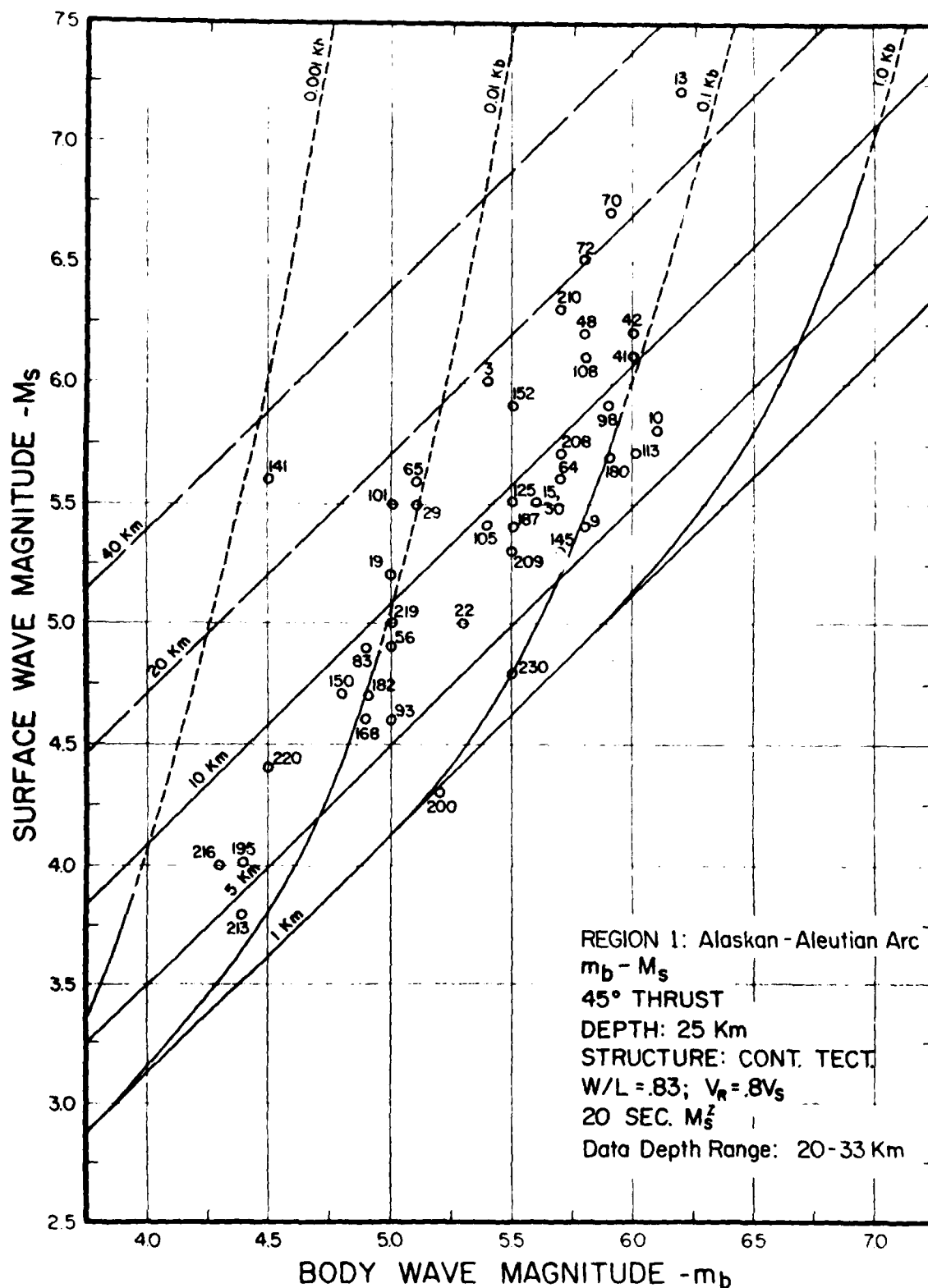
Figure 17. Surface wave magnitude versus body wave magnitude for events in the depth range 20-33 km. The theoretical curves are for events at 25 km in a continental tectonic type structure.
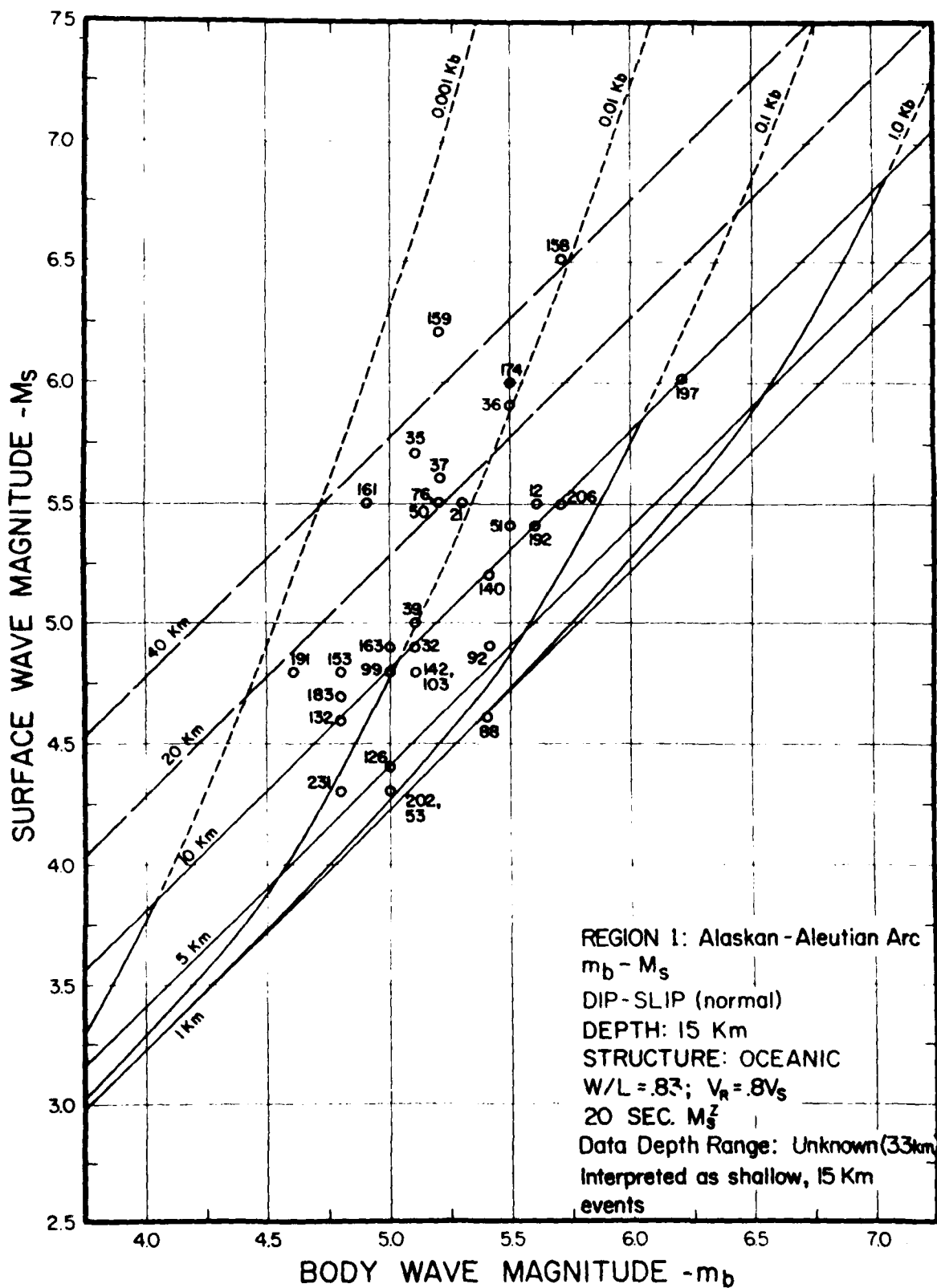
Figure 18. m_b-M_s data and theoretical curves for dip slip type events in the Alaskan-Aleutian region. Some of the smaller events indicate high average stress drops near 1 kilobar and small failure zone dimensions. The depths of these events are unknown but because of their location on the oceanic side of the trench they are interpreted as being shallow.

magnitude plane with constant stress drop but with variable fault dimension.
An important aspect of all the constant stress drop curves is their convergence
in the region of low magnitudes. Thus the separation of the "grid" defined
by these curves is not constant and, particularly for small magnitude, high
stress drop events, the convergence is such that estimates of stress will have
large uncertainty even for rather small uncertainties in the observed magnitude
values. This is particularly the case for uncertainties in m_b values for
events in this magnitude range. For events with depths between 20 and 50
km and with M_s values above about 4.5 however, the stress estimates should
be quite good average values, with only modest uncertainty due to magnitude
data and depth errors and bias (e.g., typically 20 to 30% uncertainties).

In addition to illustrating the nature of the theoretically predicted
grid of m_b versus M_s curves, from which estimates of stress and failure
dimensions can be obtained, Figure (15) through (18) show magnitude data
for the Alaskan-Aleutian region (Seismic Region 1). The data has been
separated into groupings with respect to event type and depth in order to
remove biasing of the source parameter estimates due to differences in the
magnitudes for events of different type and at different depths. The
distribution of the data in the m_b-M_s plane is typicaly of data world-wide
in that in the small to moderate event magnitude range, the average stress
drops range from about 1 bar to about 1 kbar, with the mean at about 60 bars.
The range of event maximum dimension is typically from slightly less than
1 km up to around 30 km, with only the large surface wave magnitude events
having dimensions larger than this. The mean event size in this data is
about 10 km. As can be seen, nearly all of the events are in the surface
wave magnitude range from 4.25 to 6.5 while the m_b values are essentially
all below 6.0.

An explanation of the stress drop range is based on the fact that the values obtained by this method are average stress drops corresponding to a spatial average of stress changes over the entire failure surface, or the average taken over a characteristic dimension of the order of the mean of the longest and shortest wave lengths of the seismic data used. In this case, for m_b and M_s data, this averaging dimension would be of the order of 50 km for events with fault lengths larger than 50 km and of the order of the fault length itself for the small events. We observe from the data distribution in Figure (15) through (18), that most of the very high stress drop events are of small dimension and that most of the very low stress drop events are associated with large faults. This strongly suggests that stress drop averages over a small fault will be much more strongly influenced by a high stress at the hypocenter and reflect this high stress in the average stress drop inferred from the m_b-M_s approach, while for the large faults the average is over essentially the whole failure region and the high static stress drop occurring at the hypocenter does not influence the average proportionately as much, so a low average is obtained. However the data show that the range of stress drops associated with events of fixed dimension is about one order of magnitude and this range may be due to strength variations or to the fact that the size of local stress concentrations can vary considerably.

The theoretical m_b vs M_s curves for explosions in various types of media have only been partially computed. However their form is suggested by those computed by Archambeau et. al. 1974 and by the explosion data points shown in Figure 15. In particular, explosions in any type of

event media are predicted, and observed, to occur to the right of the earthquake lines and data shown in Figure (15)-(18) . (That is, they are predicted to have relatively higher m_b and lower M_s than earthquakes.)

In terms of discrimination using source parameters, explosions have parameters characterized by small source dimension (L) and high (effective or apparent) stress drop ($\Delta\sigma$) compared to earthquakes. Therefore an appropriate discriminant based on measured source parameters is $\Delta\sigma/A$, with A representing failure zone surface area. For such a variable, one would expect the earthquake population to define a region with relatively low values of $\Delta\sigma/A$ compared to explosions. Certainly this is not surprising. The current theoretical results do however provide the means of forming such a discrimination variable and using it as a standard method for event discrimination.

References

Archambeau, C. B., General theory of elastodynamic source fields, Rev. Geophys., 6, 241-288, 1968.

Archambeau, C. B., E. A. Flinn and D. G. Lambert, Fine structure of the upper mantle, J. Geophys. Res., 74, 5825-5865, 1969.

Archambeau, C. B., The theory of stress wave rediation from explosions in prestressed media, Geophys. Jour. Roy. Astr. Soc., 29, 329-366, 1972.

Archambeau, C. B., D. G. Harkrider, and D. V. Helmberger, Studies of Multiple Seismic Events, ACDA Report ST-220. Calif. Inst. Tech., 1974.

Archambeau, C. B. and J. B. Minster, Dynamics in prestressed media with moving phase boundaries: A continuum theory of failure in solids Geophys. J. Roy. Astron. Soc., 52, 65-96, 1978.

Archambeau, C. B., M. Schnapp, and R. Goff (1981a), "Computer applications of quasi-harmonic decomposition to seismic signal detection and analysis," submitted to Geophys. J. Roy. Astro. Soc., 1981.

Archambeau, C. B., J. M. Savine, M. Schnapp, J. F. Masso, and K. Hamilton (1981b), "Methods of seismic detection and analysis based on quasi-harmonic decomposition (QHD)," submitted to Geophys. J. Roy. Astro. Soc., 1981.

Anderson, D. L. and C. B. Archambeau, The anelasticity of the Earth, J. Geophys. Res., 69, 2071-2084, 1964.

Anderson, D. L., A. Ben-Menahem and C. B. Archambeau, Attenuation of seismic energy in the upper mantle, J. Geophys. Res., 70, 1441-1448, 1965.

Anderson, D. L. and R. S. Hart, The Q of the Earth, J. Geophys. Res., 83, 5869-5882, 1978.

Barazangi, M., W. Pennington and B. Isacks, Global study of seismic wave

attenuation in the upper mantle behind island arcs using pP waves,
J. Geophys. Res., 80, 1079-1092, 1975.

Cherry, J. T., C. B. Archambeau, G. A. Frazier, A. J. Good, K. G. Hamilton
and D. G. Harkrider, The teleseismic radiation field from explosions:
Dependence of seismic amplitudes upon properties of materials in
the source region, Systems, Science and Software Report SSS-R-72-1193,
Contract No. DASA 01-71-C-0156, 1972.

Harvey, D., Seismogram synthesis using normal mode superposition: The
locked mode approximation method, Geophys. J. Roy. Astron. Soc.,
in press, 1981.

Minster, J. B., Elastodynamics of failure in a continuum, Ph. D. Thesis,
California Institute of Technology, Pasadena, California, 1974.

Mueller, R. A., and J. R. Murphy, Seismic characteristiscs of underground
nuclear detonations, Bull. Seis. Soc. Amer., 61, 1675-1692, 1971.

Appendix 1

Tectonic Generation of Anomalous Radiation from Explosions

Tectonic Generation of Anomalous Radiation from Explosions

by

Charles B. Archambeau

Introduction

Our current understanding of "tectonically generated"
seismic effects is that whenever the medium is stressed in
any manner (overburden, tectonic stresses, etc.) an explosion
which creates a cavity and shatter zone will induce an
"anomalous" motion in the medium, which is due to the relaxa-
tion of the initial stress in the medium around the fracture
zone. Anomalous seismic radiation is defined to be that part
of the seismic field that does not arise solely and directly
from the isotropically occurring conversion of the explosive
shock wave into an elastic compressional wave. That is, any
part of the field not corresponding to a pure isotropic com-
pressional source.

Not all of the observed anomalous radiation from explo-
sions need arise from stress relaxation effects, since aniso-
tropy and other local inhomogeneities (including the free
surface of the earth) can give rise to similar effects.
Kisslinger (1976) and Bache (1976b) have reviewed the likely
processes for production of the observed anomalous radiation.
It is doubtful that the seismic perturbations due to effects
other than "tectonic" are nearly sufficient to account for
the observed anomalous radiation (see Toksoz and Kehrer, 1972;
Archambeau, 1972; Bache, 1976a); especially the anomalous
radiation associated with long period surface waves.

Physical Processes of Stress Relaxation

The explosion induced stress relaxation has generally
been associated with tectonic stress relaxation, but it should

be emphasized again that <u>any</u> stress in the solid medium, what-
ever its origin, will cause a radiation effect (e.g., litho-
static stress). It is generally agreed, however, that stresses
of tectonic origin are most likely to be responsible for the
larger effects observed. What is currently less clear is
whether the stress relaxation is due to the creation of a
nearly spherical shatter zone (e.g., Archambeau, 1972;
Archambeau and Sammis, 1970), or whether it is largely due to
"triggering" of an earthquake — that is associated with induced
faulting corresponding to material failure having a strongly
asymmetrical, or linear, pattern (e.g., Aki and Tsai, 1972).
In the latter case, shatter zone induced relaxation occurs,
but in addition failure along a preexisting, or newly created,
long linear fracture is also thought to occur and would
generate additional "anomalous" radiation, especially at
the lower frequencies. The distinction between these
mechanisms has importance for discrimination as well as yield
estimation in that, if stress relaxation due to triggered
faulting occurs, then much larger perturbation of the low fre-
quency radiation would be expected than would be the case for
shatter zone induced radiation. For triggering then, one
might expect perturbations that would make accurate yield
determinations using M_s highly uncertain — for example, the
surface waves from triggering of a modest sized thrust earth-
quake could easily completely cancel or overwhelm the explosion
generated surfaces at all azimuths in the period range around
20 seconds. Further, the M_s value for the explosion plus
earthquake could, in many cases, be earthquake-like, making
discrimination by m_b-M_s problematic. The size and nature of
the effects of triggering would be difficult to accurately
predict or to correct for, since not only would information
regarding stress drops be necessary, but knowledge of the loca-
tion and orientation of the fault plane and rupture rate would
be required. On the other hand, if the physical mechanism is

simply stress relaxation around the roughly spherical shatter zone created by the explosion, then it is likely that the perturbations in the seismic radiation would be relatively smaller at low frequencies and more easily predicted and corrected for; in that the origin and geometry of the failure zone, as well as its formation rate, would be known quite well. Further, the size of the shatter zone is predictable and related to the explosion yield. (Prediction of the size, or radius, of the shatter zone is not normally available from either scaling law or empirical data, or from numerical code calculations. However, it could be obtained in these ways. In this regard, see the recommended research section below.) Finally, the tectonic and/or lithostatic stress levels in the shallow depth range for average explosions can be reasonably estimated, especially if earthquakes from the area can be studied, and a correction for stress relaxation effects on surface wave observations could then be made, probably with reasonable confidence. (Such a correction would, of course, entail uncertainties and surface wave based yield estimates would have to be compared with body wave yield estimates.) In any case, research would be required in order to develop the basis for any such correction and to determine its accuracy.

Of the two possible mechanisms for tectonic release, it seems most likely that both processes have occurred in the past. However, the simple spherical shatter zone relaxation process has probably been the mechanism giving the anomalous seismic radiation observed from most underground explosions, with triggering occurring for only a few events (about five percent or less of the total). This estimate is based on a variety of physical evidence (i.e., aftershock locations versus time, location of the "anomalous event", near field strain observations, etc.), plus the fact that the anomalous surface wave radiation can be adequately explained by spherical shatter zone induced stress relaxation for explosions with

F factors* less than around one. (When F ≃ 1, the seismic
energy of tectonic origin is about the same as that from the
pure explosion.) Even for explosions where F factors
considerably larger than one are observed, it is not certain
that large scale faulting is required. In any case, it is
likely that triggering is quite rare.

Characteristics of Observed Anomalous Body and Surface Wave Radiation from Explosions and Predictions from Explosion Induced Tectonic Release

Some typical examples of the nature of the anomalous
radiation from explosions are shown in the following figures.
The effects are most pronounced for surface waves and in this
discussion such effects are emphasized. Nevertheless, body
waves are perturbed as well, but the effect on body wave
magnitudes m_b are much less than the effect on the surface
wave magnitude M_s; so long as m_b is measured from the first
cycle of the P wave motion or is measured spectrally by
narrow band filtering using the group arrivals within 1 to
1.5 seconds of the direct P wave first motion.

An example of the effects of tectonic release on the
first arriving compressional waves from an explosion is shown
in Figure 1 (Archambeau, et al., 1974). The event modeled
is Handley (1.1 megaton) at a teleseismic distance. The
tectonic release mechanism modeled is stress relaxation
around the roughly spherical explosion generated shatter zone,
where the initial prestress is taken to be 65 bars and
homogeneous. This is a modest prestress level, and levels
of from two to three times this value would not be unlikely.
The orientation of the prestress was pure shear in the

---

*An approximate relation between the F factor, used to
characterize the anomalous, or tectonic, component of the
radiation relative to the direct explosion component is
(Toksoz, et al., 1965): $E_{tect.}/E_{expl.} = 4/3\ F^2$.

(a) DIRECT P WAVE FROM EXPLOSION (P_E)

(b) SURFACE REFLECTED P WAVE FROM EXPLOSION (pP_E^p)

(c) DIRECT P WAVE FROM TECTONIC RELEASE (P_T)

(d) REFLECTED P WAVE FROM TECTONIC RELEASE (pP_T)

(e) SURFACE CONVERTED S TO P WAVE FROM TECTONIC RELEASE (sP_T)

(f) COMPOSITE FIRST MANTLE ARRIVAL SERIES
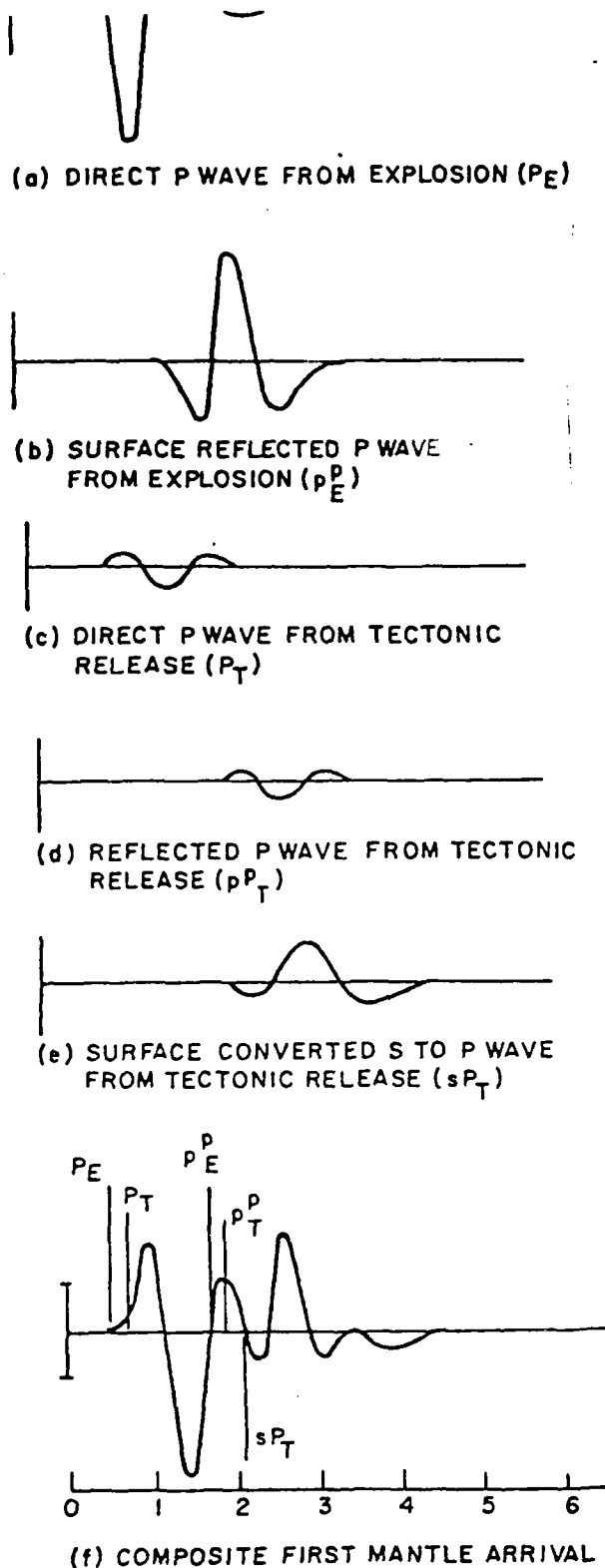
Figure 1. Theoretical compressional (P) wave phases generated by the Handley explosion and associated tectonic release. The Handley event (1100 kt) modeled by the explosion source model T-1. Prestress (σ_{13}) for tectonic release taken to be 65 bars, shatter zone radius R_0 = 750 meters. Earth structure CIT 109-- Low Q model. Distance 4066 km, azimuth 30°. Vertical component LRSM short period seismometer, source depth 1.2 km.

horizontal plane, so that relaxation of stress around the shatter zone is equivalent to a strike-slip double couple point source. For a homogeneous prestress, the stress relaxation around a spherical shatter zone is such as to always produce pure quadrupole radiation - that is a simple double couple equivalent. The figure shows the time domain pulse contributions to the overall P wave train and the important point is that the direct P wave from tectonic release is much smaller than the explosion generated P wave. On the other hand the tectonic S wave is comparable to the explosion P wave, but only contributes upon reflection at the free surface so that it influences the wave train at later times. The ratio of P to S wave production by tectonic release of this type scales is:

$$\frac{A_p}{A_s} \alpha (\frac{V_s}{V_p})^3$$

where A_p and A_s are the amplitudes of tectonic P and S waves, and V_p and V_s are the P and S wave velocities in the source region. In general then, we expect the tectonic P wave to be of the order $3\sqrt{3}$ down in amplitude from the S wave. If we consider explosions with F factors near unity, so that the tectonic energy released is nearly the same as the explosive energy converted to seismic radiation, such as in the example in Figure 1, then the tectonic P wave will be five times smaller than the direct explosive P wave (i.e., the energy of both sources is about the same but 80% of the tectonic source energy is contained in the S waves produced). The example in Figure 1 illustrates this relationship. Thus, as noted earlier, if the body wave magnitude measurement is confined to the first cycle of P wave motion, then the effects of tectonic release will be minimized. A similar conclusion was reached by Bache (1976a) from a series of modeling experiments in which P waves from a number of explosions were studied, with tectonic release effects included to achieve detailed fits to the observations.
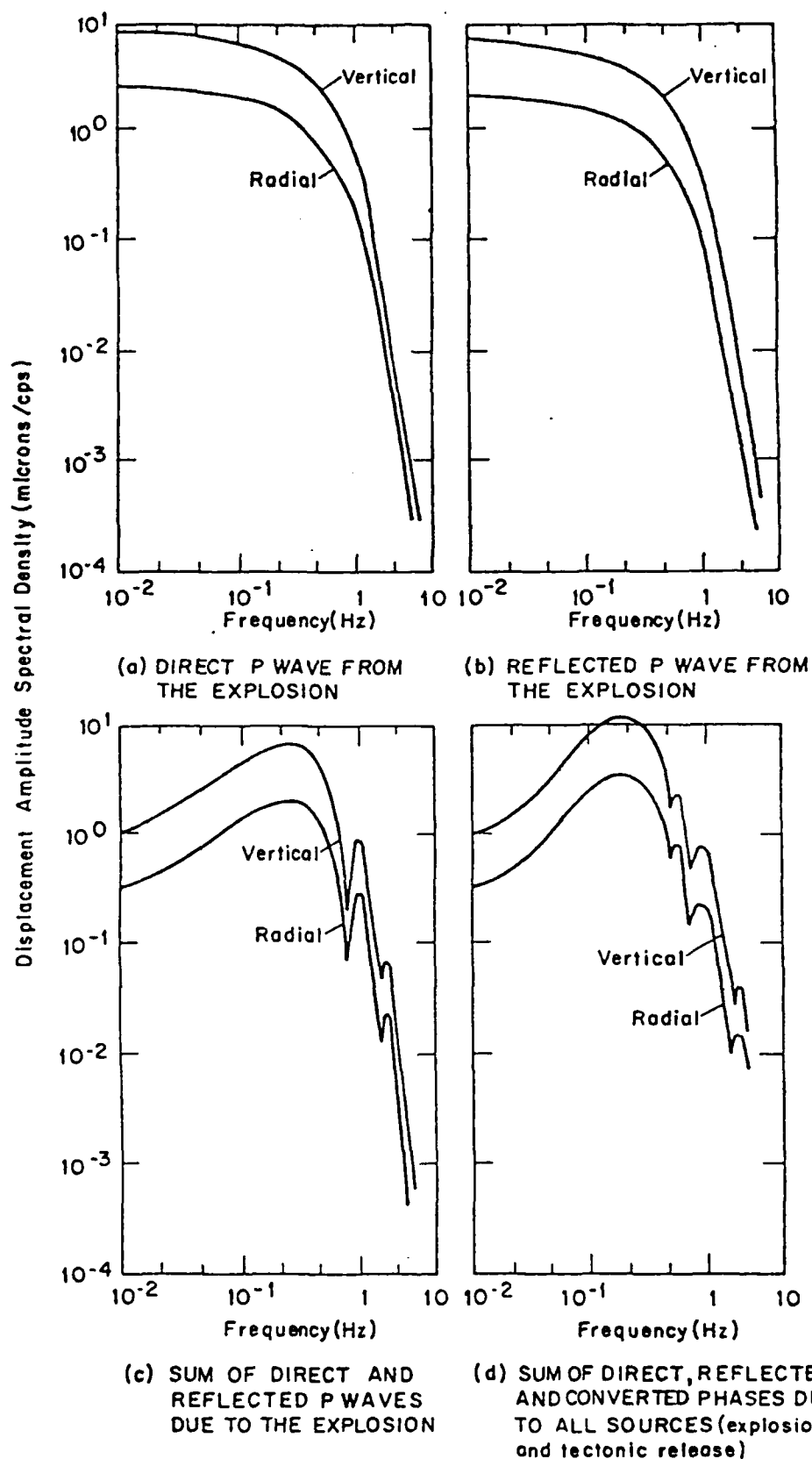
Figure 2: Theoretical spectra of explosion generated compressional arrivals from the Handley event at a distance of 4066 km and azimuth of 30°. CIT 109 Low Q model, explosion model T-1, source depth 1.2 km. Vertical and radial refer to the two components of the vector field at the earth's surface with radial denoting the horizontal component in the radial direction from the source point.

Figure 2 shows the spectra of the waves represented in Figure 1, with the last inset (d) showing the spectral perturbation resulting from tectonic effects. It should be emphasized that the composite spectrum shown in (d) is for the entire P wave train. If spectral methods are used, say narrow band filtering methods, to obtain a spectral magnitude for the first arrival pulse (i.e., the first cycle of the P wave train), then the result obtained would look like inset (c), rather than (d). Figure 3 shows the character of the entire predicted P wave train, including multiple mantle arrivals to be expected in the distance range near 4000 km, for the explosion above compared with explosion plus tectonic release. Finally Figure 4 shows a comparison with an observation, from the underground test Bilby. The predicted seismogram for the P wave train is remarkably similar to that observed, and this kind of agreement is not unusual. It is clear however, that the effect of tectonic release on the P waves is not large and that an explosion by itself could fit the observations adequately, especially when uncertainties in structure and the predicted explosive source function itself are taken into account. This is also illustrated in Figure 3 by the small differences between the theoretical seismograms with and without tectonic release.

The predictions of seismic radiation from tectonic release have usually assumed a uniform prestress condition in the medium prior to the creation of the explosive shatter zone, with the exception of the treatment employing a stress relaxation cut-off at some radius (R_s) in order to approximate the effects of a stress concentration in the medium (e.g., Archambeau, 1970, 1972). When a uniform prestress (extending to infinity) is used and a spherical shatter zone is created, then the radiated field is pure quadrupole and its far field spectrum is flat from zero frequency to a corner frequency,
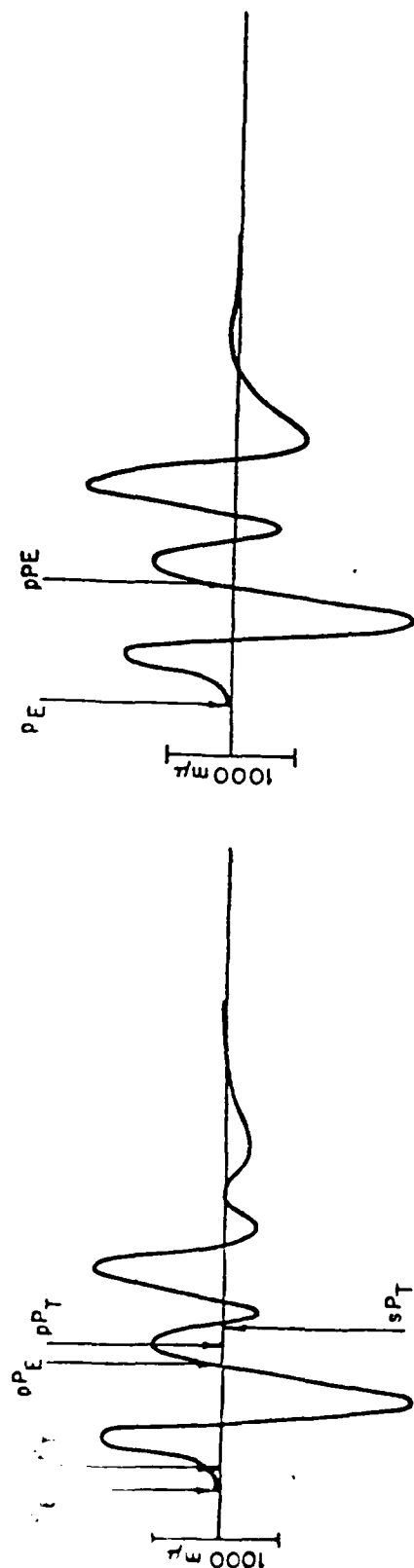
(a) FIRST MANTLE ARRIVAL, EXPLOSION PLUS TECTONIC RELEASE

(b) FIRST MANTLE ARRIVAL, EXPLOSION ONLY
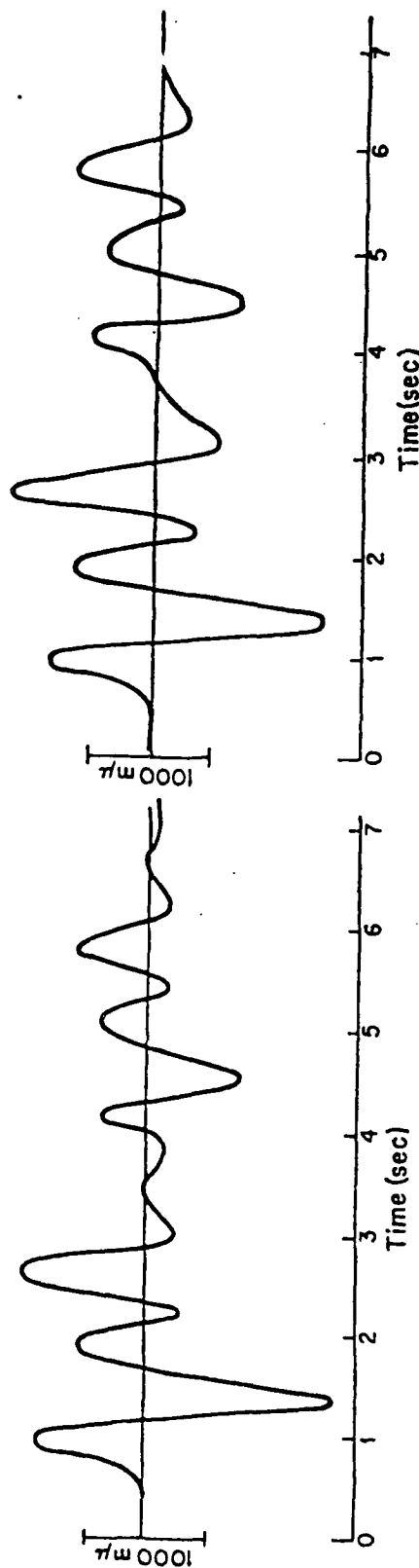
(c) FIRST AND SECOND MANTLE ARRIVALS, EXPLOSION PLUS TECTONIC RELEASE

(d) FIRST AND SECOND MANTLE ARRIVALS, EXPLOSION ONLY

Figure 3: Comparison of theoretical signals at 4066 km from Handley (1100 kT) explosion model with and without tectonic release. Explosion model was T-1, tectonic release based on 65 bar pure shear prestress (σ_{13}) and shock generated shatter zone of 750 meters in radius, source depth 1.2 km.
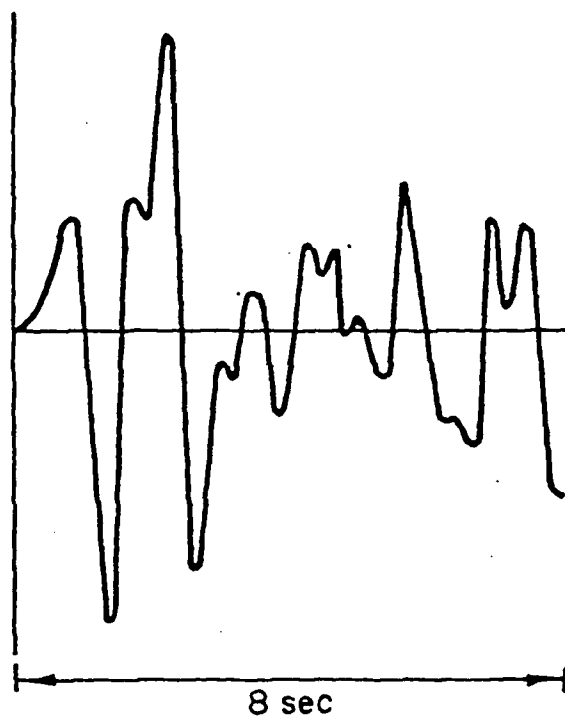
(a) OBSERVED(BILBY)
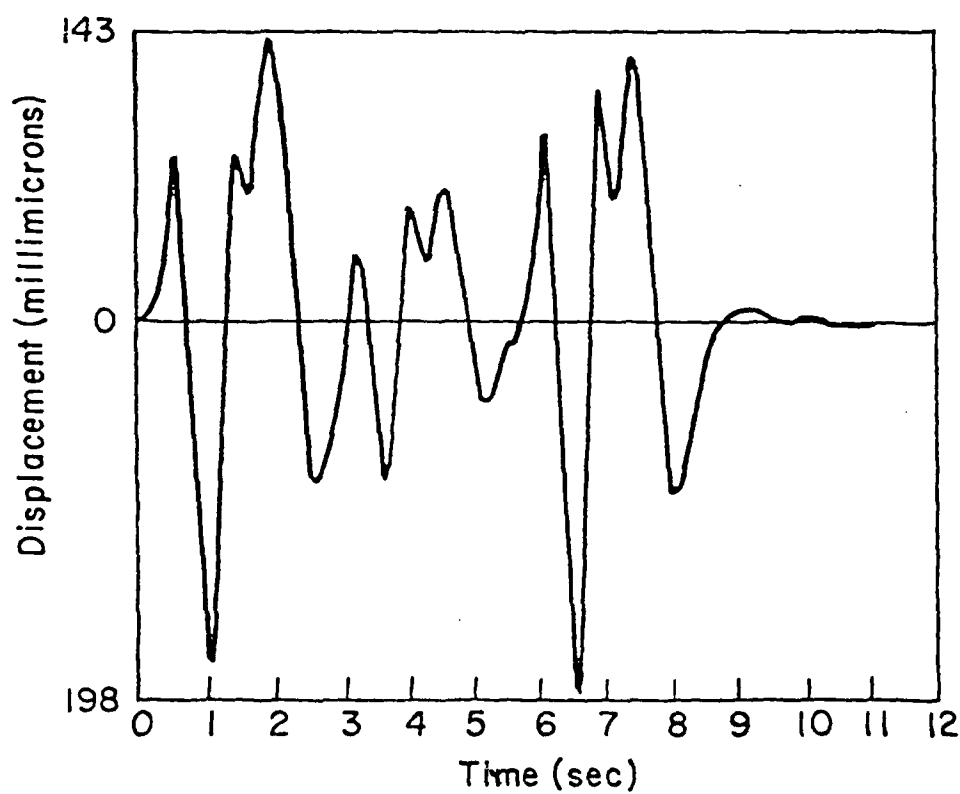
(b) THEORETICAL (MODEL T-3)

Figure 4: Comparison of observed and theoretical seismograms for the Bilby event at HNME, 4066 from ground zero.

of tectonic release (e.q., Archambeau and Sammis, 1970;
Archambeau, 1972; Aki and Tsai, 1972; Toksoz and Kehrer,
1972). The only question seems to be precisely what mechanism
of tectonic release is responsible, as noted earlier.

One line of evidence concerning the process involved
in tectonic release is furnished by direct comparison of
seismic radiation from an explosion and an earthquake occurring
in the same region. One such pair, the Fallon earthquake
(m_b = 4.4, depth 15 km) and the Shoal underground nuclear
explosion test (m_b = 4.9; test medium, granite; F = .58)
was studied in some detail by Lambert et al., 1972. These
events were separated by only a few tens of kilometers so
that the average tectonic environment, as measured by the
long period surface waves, should be comparable. Figure 10
shows one of the striking differences between true earthquake
long period radiation and the anomalous long period radiation
from explosions. In particular, the ratio of Love to
Rayleigh wave (L/R) spectral amplitudes strongly increases
with increasing period for the earthquake, while the same
ratio is essentially constant for explosions. The L/R
spectral ration for the underground test Bilby (m_b = 5.8,
test medium, tuff, F = .5) is also shown, for comparison
with another (much larger) explosion event, and it also
shows a very different period variation for L/R. The con-
clusion to be drawn is that the source of the anomalous ex-
plosion radiation, which is totally responsible for the Love
wave excitation, must be quite different from a small earth-
quake, like the Fallon event. In particular it must be
less efficient as a long wave length radiator than is a
small earthquake and thus a smaller source dimension is implied.
The tectonic stress relaxation induced by shatter zone creation
is a source of relatively small characteristic dimension that
produces quadrupole long period radiation with considerable
SH wave production. Hence, it is a most likely model for the
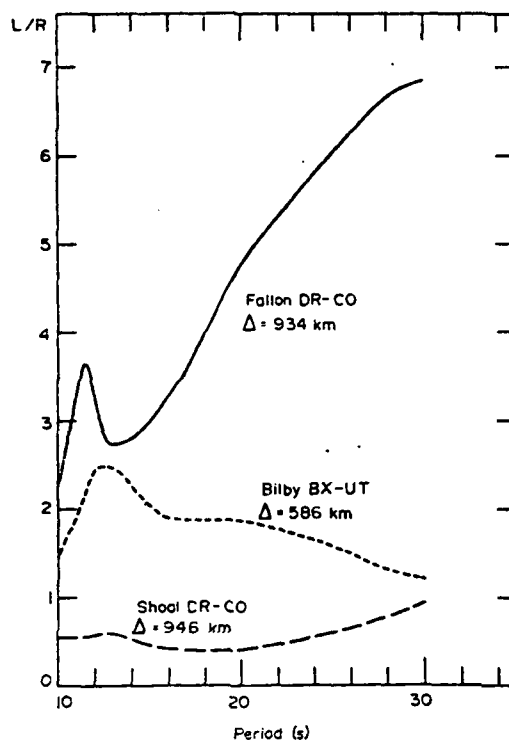
FIG. *A* The variation of L/R with period for the BILBY and SHOAL explosions and the Fallon earthquake, in the distance range near 800 km. L/R for the earthquake is larger than 2·0 and increases with increasing period. This difference in behaviour is a consequence of the much larger source dimension associated with the earthquake.
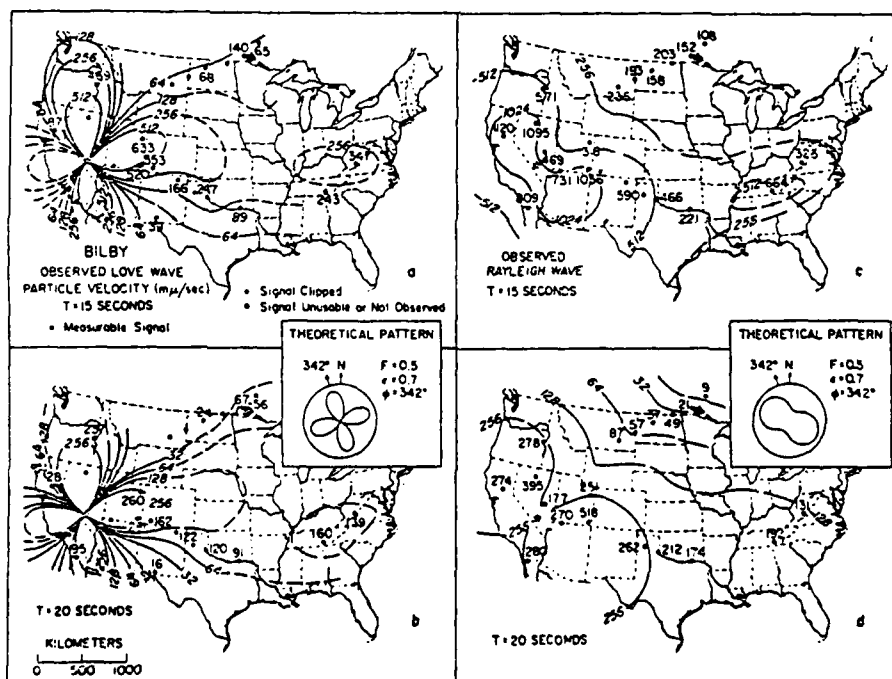
FIG. *11* Radiation patterns of Love and Rayleigh waves from BILBY at periods of 15 and 20 s. The insets show the theoretical pattern shapes obtained as a fit to the observations, using superposed monopole and quadrupole point sources with fixed relative excitation of quadrupole to monopole of $F = 0·5$, with quadrupole 'strike' $\phi = 342°$. The point source equivalents are the same for both Love and Rayleigh waves. The factor $\varepsilon = 0·7$ is the particle orbit ellipticity factor for the Rayleigh waves, which depends on the structure used in the theoretical calculations.

anomalous explosion source component. Figure 11 shows the
form of the observed radiation patterns for Love and Rayleigh
waves at periods T = 15 sec and 20 sec. The insets are the
theoretically predicted surface wave patterns based on tectonic
release due to the explosion produced spherical shatter
zone, plus the pure explosion monopole field (Lambert et al.,
1972). The prestress orientation used is such as to be
consistent with the predominently strike slip mechanism
associated with the Fallon earthquake, while the magnitude of
the initial stress required to fit the amplitude of both
the Rayleigh and Love waves was 65 bars (Archambeau and
Sammis, 1970). The (mean) prestress level seems entirely
reasonable. Thus the "shatter zone model" seems consistent
with the observations of surface wave radiation, in that the
values of prestress magnitude and orientation required to
fit both Love and Rayleigh wave observations are compatable
with the tectonics of the region.

Figures 12 and 13 show how well this model simultaneously
fits the long period surface wave radiation for the Shoal
and Bilby explosions. Here observed L/R ratios at several
stations (where the maximum observed surface wave amplitudes
are near 15 seconds) are compared to the predicted ratio at
different azimuths. The agreement is very good, considering
the probable lateral refraction effections to be expected.
Similar analysis for numerous other explosions, for example
by Toksoz and Kehrer, 1972, shows similar results.

Hence it would appear that the production of seismic
radiation by spherical shatter zone induced (tectonic) stress
relaxation can explain the anomalous long period surface
wave observations, and the P and S wave train complications
as well, in the great majority of observed cases. Particularly
for the long period surface waves, which are relatively
unaffected by small dimensional high stress concentrations,
it should be possible to estimate the magnitude of the
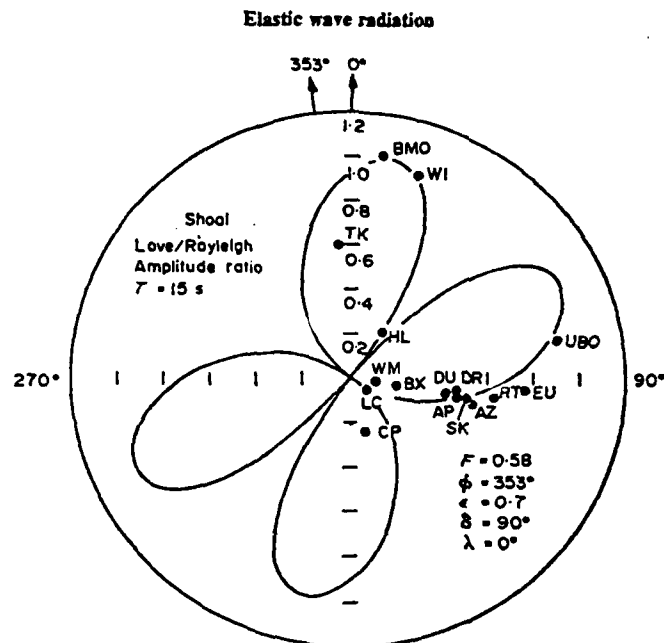
FIG. 12. The theoretical L/R ratio for SHOAL, at 15-s period, as a function of azimuth and using the source parameters indicated. Observations at various azimuths where signal-to-noise ratios where high are indicated and identified by abbreviated station symbols. This also shows the nature of the L/R azimuth variation (which is nearly identical to that for BILBY) and that a single equivalent source fits both Love and Rayleigh wave radiation for this event.
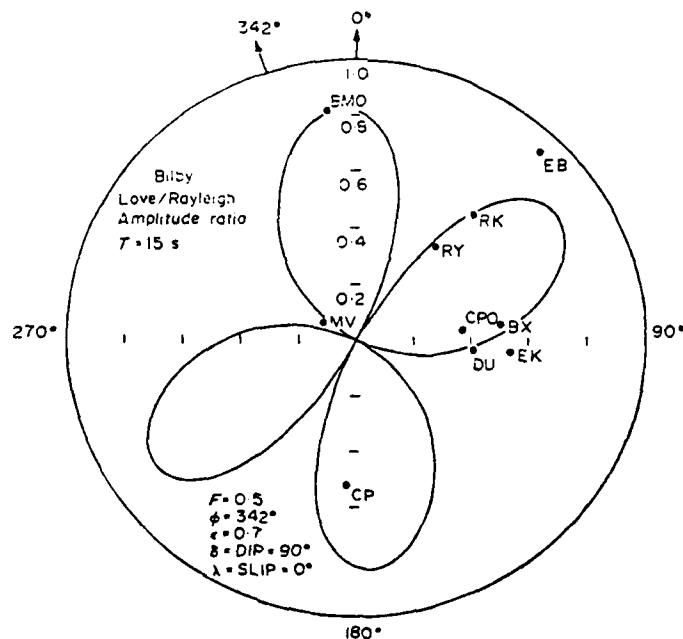
FIG. 13. The theoretical L/R for BILBY, at $T = 15$ s, as a function of azimuth using the source parameters indicated. The observed ratio at a number of stations with good signal-to-noise ratios for both Love and Rayleigh waves are shown at their appropriate azimuths. This also shows the nature of the L/R azimuth variation, and it is clear that a single equivalent source fits both Love and Rayleigh wave radiation for this event.

anomalous effects (perturbations) to be expected. On the other hand the body wave perturbations are much more difficult to predict, because of their dependence on details of the spatial dependence of the prestress, but the large effects can be avoided if only the first cycle of the P wave train is used in the event analysis.[*]

Figure 14 (Archambeau et al., 1974) shows, among other things, the effects of tectonic stress on m_b and M_s for explosions in granite, covering the yield range from 1 KT to 1000 KT, where shatter zone stress relaxation is assumed. The propagation path is appropriate to NTS, so that the upper mantle includes a well developed low velocity and low Q zone. For this reason the theoretical m_b values are some-what lower than would be expected in a non-tectonic region, but are, on the average, what appear to be appropriate for NTS and the Basin and Range Geologic Province. The circles represent predictions of m_b and M_s values[**] from the explosions alone, without tectonic release. The measurements at these points are made from the synthetic seismograms, using the first cycle of the P wave train (denoted $m_b^{(1)}$) and the Rayleigh wave vertical component at 20 seconds. The "error bars" (upward vertical lines and horizontal lines attached to each circle) indicate the possible increase in M_s if the Airy phase is measured and, for m_b, the increase to be expected

---

[*] The situation for the prediction of anomalous effects in this context is similar to the situation described by Bismark concerning Prussia and Austria; to paraphrase: "The situation (for long period surface waves) is serious but not hopeless, the situation (for short period body waves) is hopeless but not serious."

[**] The superscript "R" is used on M_s in the figure to identify the M_s measurement as being associated with the Rayleigh wave. This was employed because a superscript "L" was used for the similar magnitude measurement from Love waves. This notation is unnecessary here as M_s will always be the standard magnitude from the Rayleigh wave.
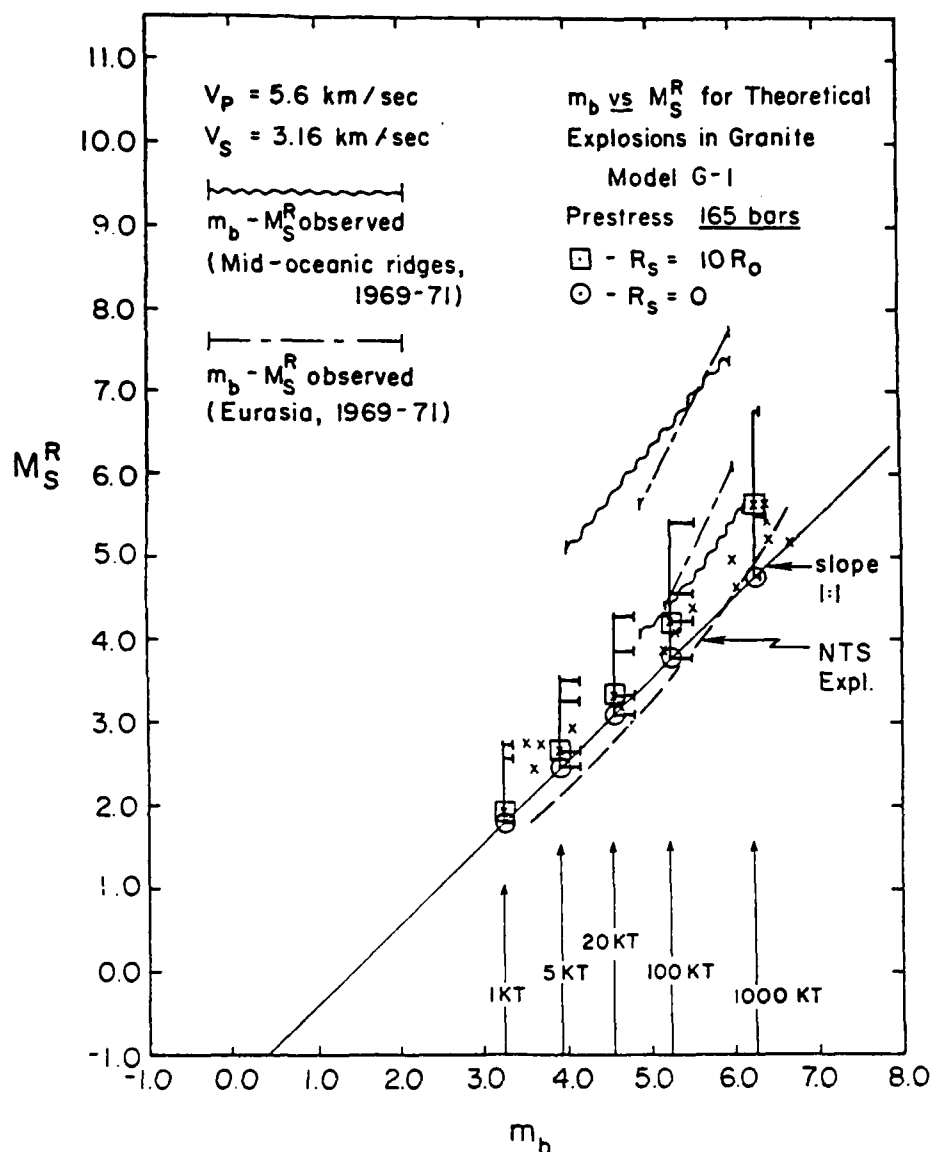
Fig. 14. Rayleigh surface wave magnitude as a function of body
wave magnitude for explosions in granite (model G-1).
The circles denote theoretical values of $m_b(1)$ and M_s
for zero prestress, the squares for 165 bar prestress.
The horizontal lines indicate the range of possible m_b
values, the vertical lines indicate the range of possible
M_s values. The large variation in M_s arises from the
possibility of measuring an Airy phase. The variation
in m_b arises from the possibility of measuring the 2nd
or 3rd cycle in the P wave train rather than the first.
The upper and lower bound lines for earthquake data are
shown for comparison along with the mean NTS explosion
magnitude line. The X symbols are individual NTS
explosions defining the extreme upper range of observed
M_s values for explosions from Nevada. The yields of
the theoretical explosions are indicated along the m_b
scale.

if the larger of the second or third cycle in the P wave
train is used to measure m_b. The squares correspond to the
m_b and M_s values that would be obtained with 165 bars prestress.
The M_s value here is not, however, an average over the whole
radiation pattern, but the largest M_s that could be measured.
It is therefore an upper bound on the (positive) perturbation
in M_s that can occur for this kind of tectonic stress release.
Naturally the "error bars" are dragged along with the point
in the m_b - M_s plane and the upper horizontal bar is associated
with the limit M_s measured from the Airy phase. The horizontal
extent of the bar indicates the perturbation possible in
m_b due to "cycle selection". The prestress orientation was
taken to be such that the radiation quadrupole corresponded
to a "strike-slip" equivalent double couple. For other
choices of prestress orientation, the maximum, and average
M_s as well, could be much reduced instead of being increased.
(e.g., A thrust equivalent could probably cancel or even
reverse the directly generated explosion Rayleigh waves.)
In any case the figure illustrates the size of the effects
for a particular case, and they are significant for M_s.
They are not very large for m_b and indeed the variations in
m_b don't change much with prestress in this special case.
However, the calculation was done with essentially uniform
prestress and when stress concentrations are present, as they
almost certainly would be in actuality, the m_b variations
could be much larger. Note also that the $m_b^{(1)}$ values are
essentially identical with and without prestress, as shown
in the figure. (i.e., The circle and square points are
only displaced vertically, showing only a perturbation in
M_s at 20 seconds.) While there actually were slight changes
in the $m_b^{(1)}$ values for the two cases, they were too small
to be shown on this plot. However, with stress concentrations
present they could be considerably larger.

Also shown on the figure are lines indicating earthquake populations for different regions, and points (x) denoting some of the more anomalous NTS explosions (generally those having high M_s values relative to their m_b values). Note that some of these events fall close to the extreme values for M_s perturbations due to this kind of tectonic release. Comparing them with the earthquake population limit lines shows that they could be confused with earthquakes on the basis of the m_b-M_s discrimination criteria alone. Finally, for general reference, the mean line for explosions at NTS is also shown.

Summary: State of Knowledge and Research Needs

The previous discussion is, in effect, a summary of what is considered to be the current state of knowledge. In addition, it is to be hoped that the uncertainties and ambiguities are reasonably well covered. By way of a summary, then, it seems most useful to briefly state the essential conclusions to be drawn, albeit with some being rather tenative, and to then list areas of research that could provide the necessary details for very firm conclusions.

The principal conclusions and results are:

(1) Stress relaxation effects can be expected in any material capable of sustaining long term non-hydrostatic stress. The largest effects will occur in the (known) regions of high tectonic activity. That is, large effects would be expected at plate margins in and near intrusive zones and generally where loading of the crust is evident, such as near large river deltas. Because of the likelihood of high stresses in seismically quiet zones along plate boundaries, it is probable that seismic gaps are areas of special importance.

(2) It appears that most of the well documented anomalous effects in the seismic radiation field from explosions (large SH wave production, observed especially at long periods from 10-25 seconds; strong perturbations in the long period Rayleigh type surface waves, azimuthally dependent increase in complexity of the short period P waves) are due to tectonic stress relaxation in the vicinity of

the roughly spherical shatter zone created by the explosive shock wave. However, there may be, at least in some cases, strong asymmetries in the fracture zone around an explosion; especially when the medium is highly stressed and/or existing stress loaded faults are nearby. In this case triggering of an earthquake is said to have occurred. However, the likelihood of this occurrence is judged to be small and to have rarely occurred in the past on a large scale. Nevertheless, it is possible that future tests could be so arranged so as to maximize the likelihood of such an occurrence. When an earthquake at or very near the test point is induced, discrimination and especially yield estimation, would be considerably more difficult.

(3) Long period surface wave radiation is strongly perturbed by tectonic release effects within the whole measureable low frequency band (i.e., from approximately 5 sec. to 60 sec. in period). The perturbations in the observed Rayleigh wave forms can be such as to add to, or subtract from, the explosive generated Rayleigh wave depending on the orientation and magnitude of the prestress in the vicinity of the explosion. The magnitude of this effect can be very (unacceptably) large. In those cases where Love waves are significant, so that tectonic release is involved, then yield estimation using M_s can only be made after correction of the Rayleigh wave measurement using the observed Love wave to deduce the size and configuration of the tectonic source. Such a correction would be much more reliable, when spherical shatter zone induced tectonic release is involved, than it would be if actual earthquake triggering is involved.

(4) Short period perturbations in the wave train can be expected to be very complex due to dependence on stress concentration effects and local complex structure. However, the perturbations should be small to moderate for the first cycle of the P wave motion, while being significantly larger for the later part of the P wave train. Body wave magnitude measured from the first P wave cycle should, therefore, be minimally perturbed by stress relaxation effects and the complexities of local structure. Further, corrections to the first cycle of the P wave for tectonic affects could conceivably be made for purposes of yield estimation.

REFERENCES

Aki, K. and Y. B. Tsai (1972), "Mechanism of Love-Wave Excitation by Explosive Sources," JGR, 27, pp. 1452-1475, March.

Archambeau, C. and C. Sammis (1970), "Seismic Radiation from Explosions in Prestressed Media and the Measurement of Tectonic Stress in the Earth," Reviews of Geophysics and Space Physics, 8, August.

Archambeau, C. B. (1972), "The Theory of Stress Wave Radiation from Explosions in Prestressed Media," Geophys. J. R. Astr. Soc., 29, pp. 329-366.

Archambeau, C. B., D. G. Harkrider and D. V. Helmberger (1974), "Studies of Multiple Seismic Events," ACDA Final Report, Contract ACDA/ST-220.

Bache, T. C. (1976a), "The Effect of Tectonic Stress Release on Explosion P-Wave Signatures," BSSA, 66, pp. 1441-1457, October.

Bache, T. C. (1976b), "The Seismological Evidence for the Triggering of Block Motion by Large Explosions," DNA Report, Contract No. DNA001-76-C-0072, December.

Kisslinger, C. (1976), "A Review of the Mechanisms of Induced Seismicity," Eng. Geol., 10, pp. 85-98.

Lambert, D. G., E. A. Flinn and C. B. Archambeau (1972), "A Comparative Study of the Elastic Wave Radiation from Earthquakes and Underground Explosions," Geophys. J. R. Astr. Soc., 29, pp. 403-432.

Stevens, J.L. (1980), "Seismic Radiation from the Sudden Creation of a Spherical Cavity in an Arbitrarily Prestressed Elastic Medium," Geophys. J. Roy. Astron. Soc., in press.

Toksoz, M.N., D.G. Harkrider and A. Ben-Menahem (1965), "Determination of Source Parameters by Amplitude Equalization of Seismic Surface Waves: Part 2. Release of Tectonic Strain by Underground Nuclear Explosions and Mechanisms of Earthquakes," J. Geophys. Res., 70, pp. 907-922.

Toksoz, M. N. and H. H. Kehrer (1972), "Tectonic Strain Release by Underground Nuclear Explosions and Its Effect on Seismic Discrimination," Geophys. J. R. Astr. Soc., 31, pp. 141-161.

Appendix 2

Regional Attenuation Effects on P Waves and Effects
of Attenuation on Surface Waves

Regional Attenuation Effects on P Waves and Effects of Attenuation on Surface Waves. Charles Archambeau

Introduction.

The effects of attenuation for both surface and body waves can be described, most appropriately, in terms of intrinsic dissipation functions $Q_\alpha(r, f)$ and $Q_\beta(r, f)$ for the earth. Here Q_α and Q_β are Q functions for compressional and shear wave losses respectively, and both are functions of radius and frequency[+]. They are also functions of the other spatial coordinates, but it is easier and actually most appropriate to define different Q models for different geologic provinces. It is quite clear from observational results for body waves (e.g., Archambeau, Flinn and Lambert, 1969) that much of the dissipation of P waves takes place in the low velocity zone. Therefore high attenuation is correlated with high heat flow and large P delays, these in turn characterizing geophysical-geological provinces. In particular, shield areas with low heat flow and negative P-delays show low attenuation, while active tectonic provinces with high heat flow and positive P-delays show high attenuation. All of these effects are clearly related to the depth span and intensity of the low velocity zone. These correlations are clearly shown form the studies of pP pulses from earthquakes in trench zones (e.g., Barazangi, Pennington and Isacks, 1975), as well as from teleseismic P wave observations from explosions (e.g.,

---

[+]Q_α and Q_β can be related to each other under the assumption that dissipation in pure compression is very small relative to losses in shear. Then, for typical mantle elastic velocities, $Q_\alpha \simeq 9/4\, Q_\beta$. For details see Anderson et al., 1965.

Der et al., 1975; Der and McElfresh, 1976). Thus, for body wave magnitudes, one expects variations in m_b which are directly related to the geologic provinces of the source and receiver. In particular, sources in tectonic provinces will show reduced m_b values at 1 Hz relative to the same sources in shield regions. Since tectonic provinces show, in general, highly variable low velocity zone thicknesses and correspondingly variable heat flow values and P delays, one can also expect variability in the m_b reduction, from quite large reductions to rather small reductions, depending on precisely where the source is located.

Similar statements can be made about surface wave attenuation relative to Geological-Geophysical provinces. That is, the strongest attenuation occurs within the low velocity zone and strong surface wave attentuation is correlated with regions of high heat flow, large P (and S) wave delays and tectonic activity. For shorter period surface waves not penetrating the low velocity zone however (i.e., for periods less than 30 seconds), the attenuation is not as large as for longer period surface waves (i.e., the observed Q is about 300 compared to observed Q values of around 100 for surface waves in the period range 30-200 seconds) and there is less regional dependence in attenuation (e.g., Solomon, 1972). However, Mitchell, 1975, has shown that for rather short period surface waves, near 5 seconds, the attenuation is quite strongly regionally dependent. Nevertheless, he finds that for the longer periods up to 30 seconds, there is little regional dependence. This very short period regional dependence in attenuation is probably more related to scattering than to anelastic effects, in that tectonically active provinces usually show larger near surface lateral variability in velocity structure than do the more stable provinces.

Thus M_s values based on 20 second Rayleigh waves do not show strong regional "Q-bias".

The frequency dependence of the anelastic dissipation has only recently been considered in any great detail. Originally Archambeau et al., 1969, showed that P_n phases in the Western U.S. were attenuated such that the high frequencies required higher Q_α values than the lower frequencies - that is, the Q_α appeared to increase with frequency in the frequency range from .5 to 3 Hz. These direct observations were also in agreement with the observation that Q_α (and Q_β) models obtained from low frequency surface waves had lower Q_α values, essentially everywhere in the mantle, when compared to the Q_α model obtained from high frequency (1 to 3 Hz) body wave observations. The upper mantle Q_α models that have been obtained from low frequency surface wave and free oscillation data and from high frequency body wave data are shown in Figure 1. The model SL8 is from the analysis of free oscillation data by Anderson and Hart , 1978; the model MM8 is from surface wave data inversion by Anderson et al., 1965; and the model AFL is from body wave data inversion by Archambeau et al., 1969. Each model applies only to the frequency range covered by the data used to obtain it. The trend of these results is toward high Q values with increasing frequency of the data used in this inversion.

Solomon, 1972b, proposed a frequency dependent intrinsic Q for the mantle involving activated processes that satisfied the observed long period surface wave dispersion quite well. Liu and Archambeau, 1975 and 1976, showed that this model fit the total set of surface wave and free oscillation data quite well and that it predicted relatively large shifts in the dispersion (group velocity versus frequency) and free oscillation periods,
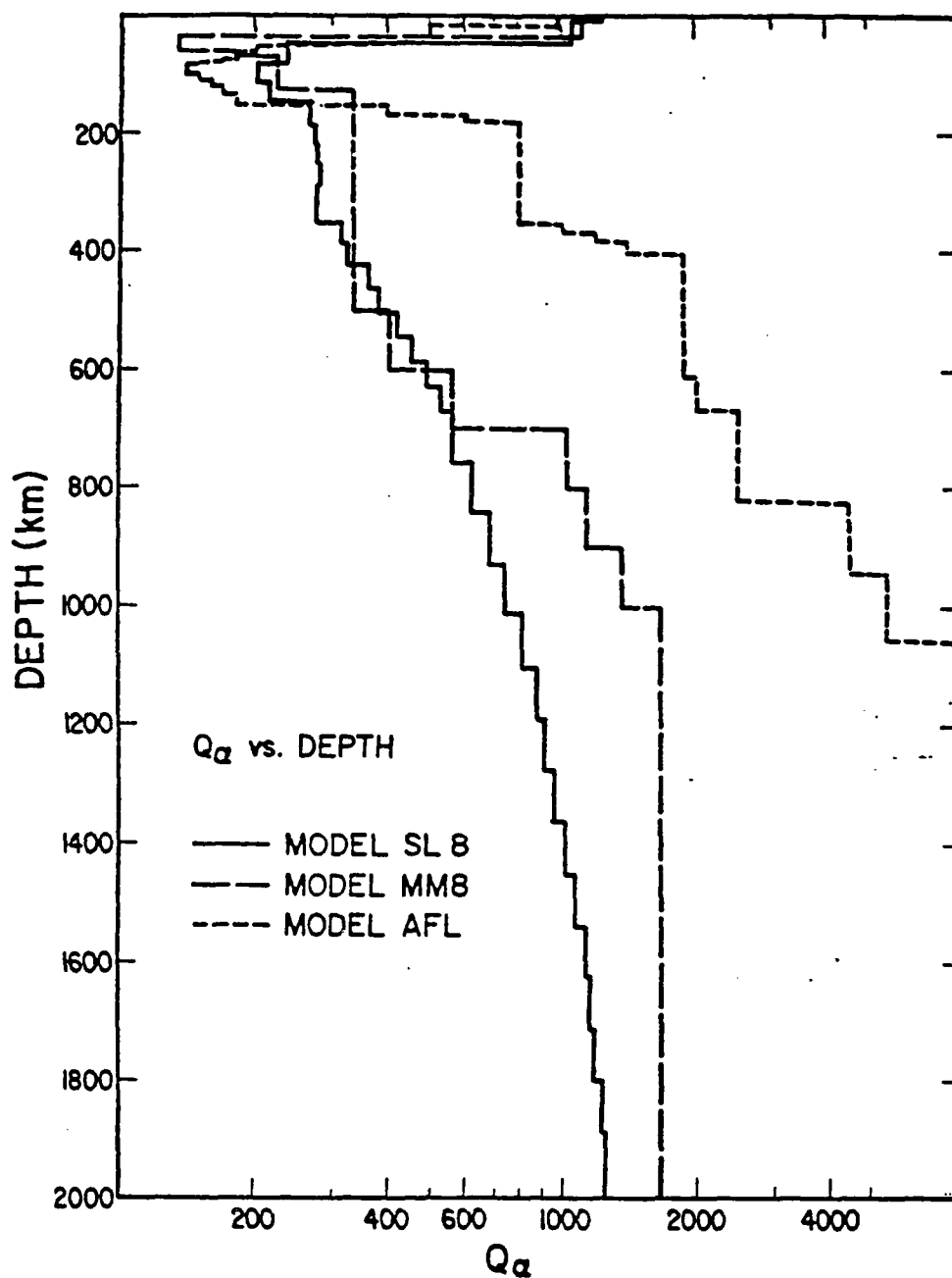
Figure 1. Q_α-vs-depth. Models SL8 and MM8 were derived from free oscillations and surface waves, respectively. Model AFL was derived from P body waves in the range 1-5 Hz. Note that Q tends to increase with the frequencies in the data set.

showing that the effective velocity structure sensed by low frequency waves
is different than that for higher frequency waves. Liu et al., 1976,
expanded upon these results and proposed an absorption band intrinsic
Q model that consisted of a distribution of activated processes, each with
a different characteristic relaxation time corresponding to a superposition
of many absorption processes acting to dissipate energy. This model was
also shown to be compatible with observations of surface wave and free
oscillation dissipation. The absorption and Q model amounts to an ex-
tension of Solomon's model, wherein many activated processes are allowed
rather than one or two, and is more realistic in terms of the known micro-
physics of crust-mantle materials.

Currently this kind of intrinsic Q model is being used to constrain
the frequency dependence of the intrinsic Q in the earth, in order to
invert for both the depth dependence and the shape of the absorption band
at each depth (and hence the intrinsic frequency dependence of Q_α and
Q_β). Figure 2, from Lundquist, 1980, shows the form of the absorption
band models being used. Such an absorption band applies at each depth in
the earth and varies with temperature pressure, material chemistry and
phase state. The parameters τ_1 and τ_2 are low and high frequency
"relaxation times" corresponding to the half amplitude points on the
"Q-filter" in the frequency domain. These parameters are treated as unknowns
and are obtained, as functions of depth, by inverting the observed attenuation
data.

The Q models shown in Figute 1 have very poor resolution of Q variations
in the crust, mainly because little or no very short period surface wave data
was used for the inversion with the surface wave and free oscillation data
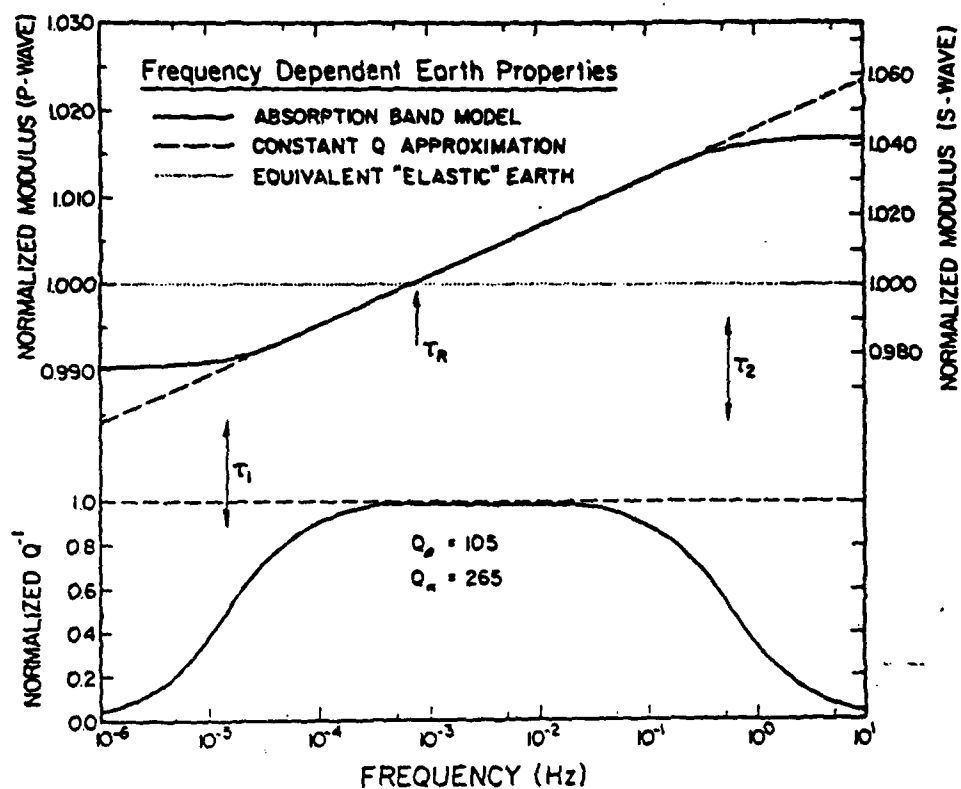
Figure 2. Frequency dependent Earth properties-vs-frequency. The normalized modulus is a direct measure of dispersion, and the absorption band is a direct measure of per-cycle attenuation. Note that the difference between dispersion for constant Q and absorption band Q is small but that the difference in implied attenuation is very large for $\omega > 1/\tau_2$.

and, in the case of the body wave derived model, the sampling of the crust using teleseismic P waves was minimal. Mitchell, 1980, has however studied relatively short period surface wave propagation in the Eastern U.S. (with periods from 1 to 40 seconds) and obtained crustal Q_β models in some detail. He has also shown that the intrinsic Q_β can be best described by a frequency dependent Q-function of the form:

$$Q_\beta(\omega, r) = Q_\beta(r)\omega^\zeta$$

with ζ between .3 and .5 for the period range 1 to 40 seconds. Here again it appears that the intrinsic Q increases with increasing frequency, however such a conclusion based on the fits given by Mitchell may be premature. In any case his models show a Q_β average of about 250 in the upper crust (0-15 km) and near 1000 for the lower crust (15-40 km). These values are significantly higher than the Q_β values in the low velocity zone of the upper mantle, where $Q_\beta \simeq 50-100$ is appropriate.

It is clear that the effects of attenuation on surface wave magnitudes, measured at 20 seconds, are not as extreme as are attenuation effects on body wave magnitudes. First, there is little observed regional variation in attenuation in this period range. Second, the attenuation is not very large, that is the Q of the crust, while of course variable in both frequency and with depth, is quite high. Thus, corrections in M_S for attenuation could be made and they would not be very large. It is of course important that M_S be measured at 20 seconds.

Frequency Dependent Q Models for Teleseismic P waves and Mantle Surface Waves

The best (i.e. only) first order frequency dependent Q model for the upper mantle has been obtained by Lundquist, 1980. The model uses

an absorption band intrinsic Q of the type shown in Figure 2. The model

is obtained by first taking the previously determined low frequency Q models

(the MM8 and SL8 models in Figure 1) and the high frequency model AFL in

Figure 1 as appropriate Q variations in the mantle in the frequency ranges

for which they are defined. That is, the frequency dependent

model is constrained to give, to first order at least, the SL8 model at

very low frequencies and the AFL model at high frequencies, near 3 Hz.

The observed Q models in Figure 1 turn out to imply that there is one

absorption band model for the mantle beneath the low velocity zone, having

regular properties varying with depth in a manner consistent with the

temperature-pressure variations in the earth in this depth range, and a

separate, very different, kind of absorption band which appears to be

confined to the low velocity zone. The absorption band for the low

velocity zone appears to be narrow (i.e., τ_1 and τ_2 relatively close in

value) while the lower mantle absorption band appears to be very broad

(i.e., τ_1 very large and τ_2 near .1 sec). The second absorption

band associated with the low velocity zone may be a consequence of a

partial melt state within the zone. In any case it is confined to this

zone and therefore varies with the extent and intensity of the low velocity

zone.

Using such a rough double absorption band Q model as a starting point,

the frequency dependent Q model can be refined by adjusting the various

absorption band parameters (in particular the "high and low" frequency

relaxation times τ_2 and τ_1 plus the maximum Q^{-1} level of the absorption

band at each depth) to fit frequency and time domain observations. In particular,

Lundquist adjusted the starting double absorption band model to be such that

when attenuation corrections are applied to observed earthquake and explosion

P wave spectra, then corrected source spectra had high frequency asymptotic

behavior of the form $1/\omega^2$ or $1/\omega^3$, as is expected from source theory

considerations. Further, he used the resulting, somewhat refined, Q model

to predict time domain synthetic P wave forms and further adjusted the

model to achieve detailed fits to the first cycle of the P wave train from

explosions. (Only the first cycle of the P wave train is reasonably well

predicted by currect explosions models. Further, it is relatively free

from uncertainties introduced by near source structure, tectonic release

and spall phase production.)

The net result was that the initial double absorption band model, in-

ferred from the low and high frequency Q models of Figure 1, fit the observations

from NTS explosion events very well, with little adjustment necessary.

Thus this model closely corresponds to the free oscillation model SL8 at low

frequencies and the body wave model AFL at high frequencies and predicts

the behavior of a mantle Q at other frequencies such that both spectral and

time domain observations are well satisfied. Figure 3 shows the properties

of this double absorption band model (solid line) as a function of depth and

frequency in the earth. The upper inset indicates the apparent Q_α in the

crust, which is poorly resolved but is high, as indicated. The next inset

shows the typical form of the double absorption band in the low velocity

zone. The dotted line shows the single absoprtion band that would exist if

the low velocity zone were absent, so that the departure of the solid line

from the single absorption band Q_α indicates the effect of the second

absorption band associated with the low velocity zone. At greater depths the

variation in the absorption band is such that the maximum level of Q_α for
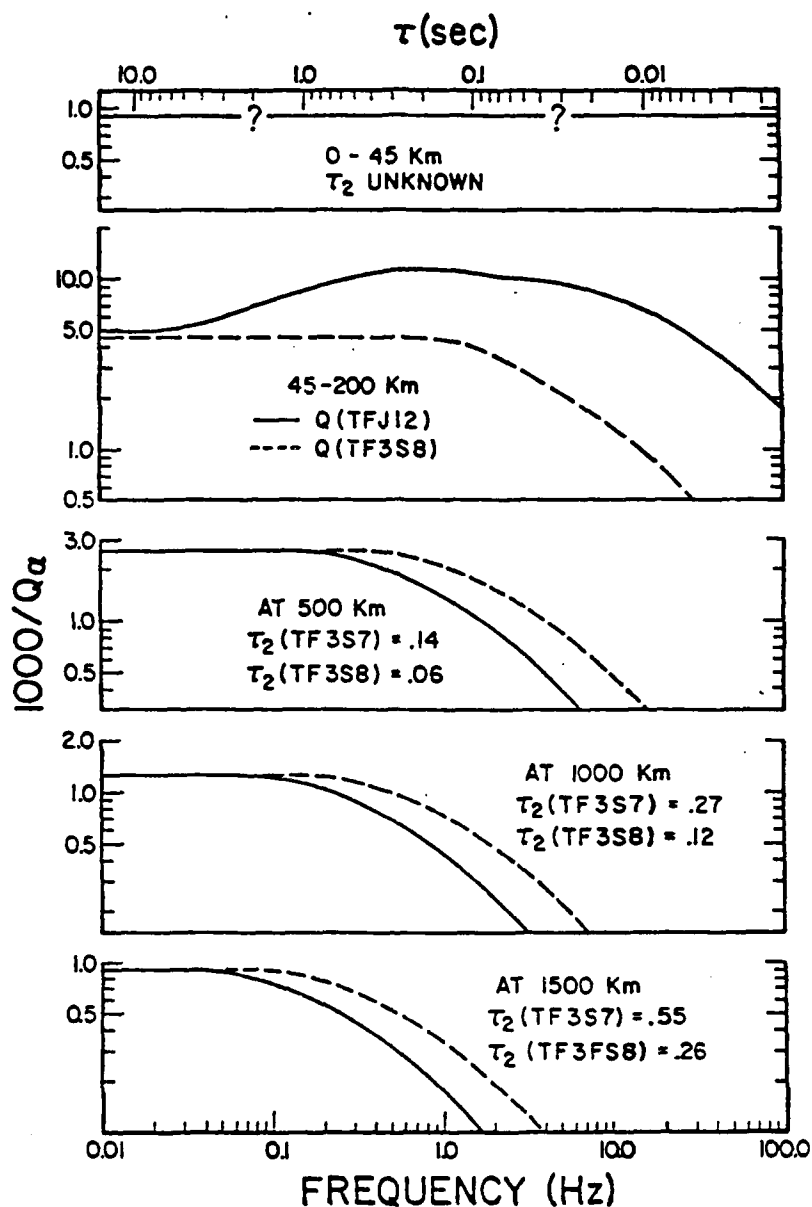
Figure 3. Absorption bands in the Earth-vs-frequency and depth. The dashed line represents the single absorption band model, TF3S8, and the solid line represents the double absorption band model, TFJ12. At low frequencies, both models converge to Q^{-1}(SL8), and model TFJ12 converges to Q^{-1}(AFL) at 3 Hz.

the band increases ($1/Q_\alpha$ decreases) and the relaxation time τ_2 increases; both uniformly in a manner controlled by the temperature-pressure increases with depth.

On the other hand, for non-tectonic regions, the Q_α variation with depth and frequency was found to be somewhat different than for the Basin and Range region. In particular, using explosion data from Novaya Zemlya, so that a stable platform region was sampled, the Q_α variation with depth was intermediate between the single absorption band variation shown by the dotted line in Figure 3 and the double absorption band model for the Basin and Range. (See Lundquist, 1980 for details.) This appears to be due to a less intense and thinner low velocity zone for the stable platform region and a correspondingly more depth confined and less intensive second absorption band in the 45-200 km depth range. This of course again implies regional variations in attenuation, but specifically that this variation is controlled by the presence or absence of the second absorption band. Further, because of the nature of this absorption band, in particular its frequency band width, the frequency dependence of the absorption can be quite different from region to region.

The consequences of this kind of Q model, in terms of t^* (total travel time divided by the effective Q over the path of the wave), are shown in Figure 4 for the double absorption band model. Clearly t^* is quite strongly frequency dependent.

These results have a number of important implications. First it seems evident that t^* should not be used in modeling work, but rather the Q_α or Q_β models should be used and modeling should be done in the frequency domain in order to properly account for both the depth and frequency dependence of the Q and for the different apparent "elastic" velocities sensed by waves of different frequency. Second, high frequency seismic energy is
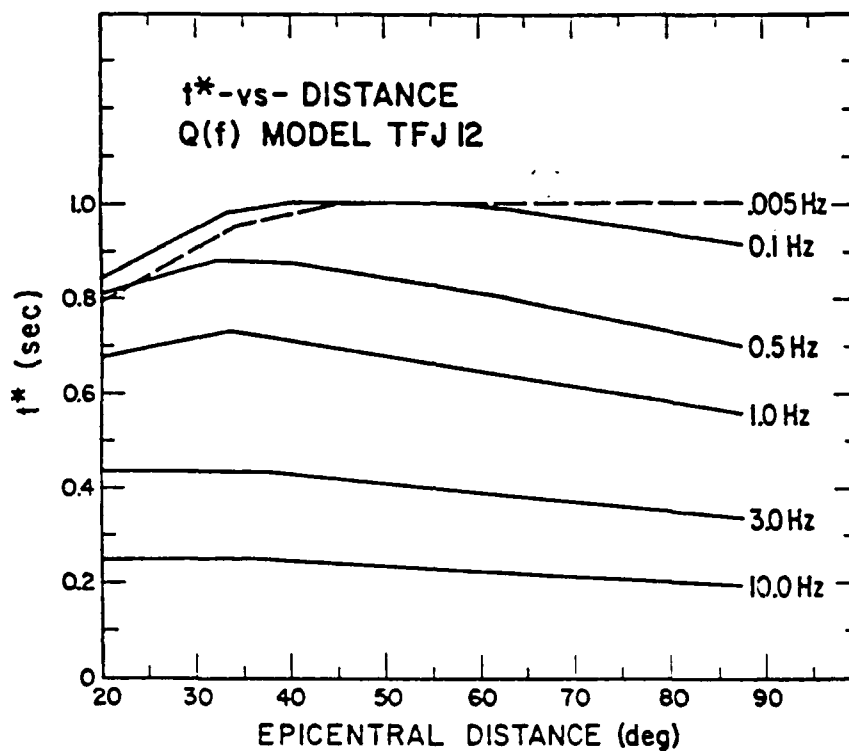
Figure 4. t*-vs-distance for selected frequency. The velocity model used is QM2, and the Q model.is the double absorption band model, TFJ12. t*(TFJ12) converges to t*(AFL) at 3 Hz and converges to t*(SL8) as frequency decreases.

propagated with much less attenuation than was previously supposed (by some
at least). Finally, the efficiency of the high frequency propagation may
be highly variable from province to province and will be correlated with the
extent and intensity of the low velocity zone.

Effects of Attenuation on Surface Waves

The Q models derived from body waves can be used to predict the
attenuation of surface waves and vice-versa. Obviously combinations of
surface and body wave data can be used to infer Q_α and Q_β as well, and
either can be predicted from the results. Therefore the Q_α models
discussed in the previous section can be used to infer Q_β (from a relation
such as $Q_\alpha \simeq 9/4\ Q_\beta$), and the resulting model can be used to predict, to
first order at least, the expected surface wave attenuation. Lundquist's
model is , in this regard, adequate for the prediction of the longer period
surface wave attenuation (T > 40 sec) but is not well enough defined in the
crust to give very accurate predictions for shorter period surface waves.
Inasmuch as the 20 second period fundamental model Rayleigh wave, in particular,
is of major interest in view of its use in M_s calculations, it is necessary
to consider high resolution crustal Q models, such as are being obtained
by Mitchell (1980). It seems sufficient here to only refer to Mitchell's work
and to recall the general comments made earlier in the introduction. In
particular, that a slight frequency dependence is inferred in Q_β , with the
Q_β increasing with increasing frequency; that the mean Q_β in the crust is
relatively high, and that regional dependence of the attenuation of surface
waves in the range $5 \lesssim T \lesssim 40$ sec is small. All in all it does not appear
that crustal surface wave attenuation is particularly difficult to deal with
for purposes of M_s corrections, to obtain yield estimates and for discrimination.

More difficult, and much larger, are corrections in M_s for tectonic effects and probably for lateral variations in structure. Uncertainties in these latter effects completely overwhelm any correction uncertainties due to anelasticity effects.

Summary: State of Knowledge and Research Needs.

The essential conclusions of this report are:

(1) Frequency dependent Q models appear to be required in both the crust and upper mantle. Absorption band models, with the Q magnitude and frequency dependence varying with depth appear to be physically realistic and to satisfy the available data.

(2) A single absorption band appears to be appropriate for the entire mantle exclusive of the low velocity zone. Within the low velocity zone, when present, a second narrow absorption band appears to existand accounts for the increased attenuation and different frequency dependence of the attenuation in tectonic regions. This second absorption band is the likely mechanism for variablility of body wave absorption from region to region.

(3) High frequency seismic body waves propagate with relativly great efficiency from (and within) regions not having a well developed low velocity zone. Tectonic zones will typically absorb much more of the high frequency energy and this will generally result in lower m_b values. For this reason m_b should be measured "spectrally" (i.e., by narrow band filtering at 1 Hz with the first cycle of the P wave train selected) to avoid measuring m_b at different effective periods, and Q corrections should be made in order to account for differences in the regional Q structure.

(4) Surface waves in the 5-40 sec period range are not attenuated strongly by the crustal Q and there is no strong regional dependence in the attenuation in this period range. For longer periods there would,

however, be some fairly significant regional variations due to the variations in the low velocity zone. Because of the inferred high Q of the crust, especially for high frequencies, it is also implied that near regional range body waves (out 200 km or so from a source) will be weakly attenuated and high frequencies should be propagated efficiently in all cases. In regions with little or no low velocity zones (V_p), the range of efficient high frequency propagation could be much greater-perhaps out to 15° or greater.

Some research that could provide needed detail and better quantify the first order models so far obtained, includes:

(1) Simultaneous matching of explosion event body wave seismograms in the near, regional and teleseismic distance ranges with the objective of eliminating uncertainties in the source function, so that Q models could be obtain that were relatively free from trade-off problems with the source function.

(2) Use long period surface waves and high resolution analysis methods for station to station analysis of attenuation to obtain Q models that would be free from source trade-off problems. This approach would also give regional Q models.

REFERENCES

Anderson, D.L. and C.B. Archambeau, The Anelasticity of the Earth, J. Geophys. Res., 69, 2071-2084, 1964.

Anderson, D.L., A. Ben-Menahem and C.B. Archambeau, Attenuation of Seismic Energy in the Upper Mantle, J. Geophys. Res., 70, 1441-1448, 1965.

Anderson, D.L. and R.S. Hart, The Q of the Earth, J. Geophys. Res., 83, 5869-5882, 1978.

Archambeau, C.B., E.A. Flinn and D.G. Lambert, Fine Structure of the Upper Mantle, J. Geophys. Res., 74, 5825-5865, 1969.

Barazangi, M., W. Pennington and B. Isacks, Global Study of Seismic Wave Attenuation in the Upper Mantle Behind Island Arcs Using pP Waves, J. Geophys. Res., 80, 1079-1092, 1975.

Der, A.A. and T.W. Elfresh, P-Wave Spectra of the Salmon Nuclear Explosion, Bull. Seism. Soc. Am., 66, 1609-1622, 1976.

Der, Z.A., R.P. Masse and J.P. Gerski, Regional Attenuation of Short-Period P and S Waves in the United States, Geophys. J. Roy. Astron. Soc., 40, 85-106, 1975.

Liu, H.-P. and C.B. Archambeau, The Effect of Anelasticity on Periods of the Earth's Free Oscillations (Toroidal Modes), Geophys. J. Roy. Astron. Soc., 43, 795-814, 1975.

Liu, H.-P. and C.B. Archambeau, Correction to 'The Effect of Anelasticity on Periods of the Earth's Free Oscillations (Toroidal Modes)', Geophys. J. Roy. Astron. Soc., 47, 1-7, 1976.

Liu, H.-P., D.L. Anderson and H. Kanamori, Velocity Dispersion due to Anelasticity: Implications for Seismology and Mantle Composition, Geophys. J. Roy. Astron. Soc., 47, 41-58, 1976.

Lundquist, G.M., Constraints on the Absorption Band Model of Q, J. Geophys. Res., in press, 1980.

Mitchell, B.J., Regional Rayleigh Wave Attenuation in North America. J. Geophys. Res., 80, 4904-4916, 1975.

Mitchell, B.J., Frequency Dependence of Shear Wave Internal Friction in the Continental Crust of Eastern North America, preprint, 1980.

Solomon, S.C., On Q and Seismic Discrimination, Geophys. J. Roy. Astron. Soc., 31, 163-177, 1972a.

Solomon, S.C., Seismic Wave Attenuation and Partial Melting in the Upper Mantle of North America, J. Geophys. Res., 77, 1483-1502, 1972b.

Appendix 3

Theoretical m_b vs M_s Curves for Earthquake Sources

A. Theoretical m_b *vs* M_s curves for Thrust, Dip Slip and Strike slip events
    in Basin and Range type *continental-tectonic structure.*

Figure 1-a.   Thrust (45°) events at a depth of 10 km.

Figure 1-b.   Thurst (45°) events at a depth of 15 km.

Figure 1-c.   Thrust (45°) events at a depth of 25 km.

Figure 1-d.   Thrust (45°) events at a depth of 35 km.

Figure 1-e.   Thrust (45°) events at a depth of 45 km.

Figure 2-a.   Dip slip (normal) events at a depth of 10 km.

Figure 2-b.   Dip slip (normal) events at a depth of 15 km.

Figure 2-c.   Dip slip (normal) events at a depth of 25 km.

Figure 2-d.   Dip slip (normal) events at a depth of 35 km.

Figure 2-e.   Dip slip (normal) events at a depth of 45 km.

Figure 3-a.   Strike-slip events at a depth of 10 km.

Figure 3-b.   Strike-slip events at a depth of 15 km.

Figure 3-c.   Strike-slip events at a depth of 25 km.

Figure 3-d.   Strike-slip events at a depth of 35 km.

Figure 3-e.   Strike-slip events at a depth of 45 km.
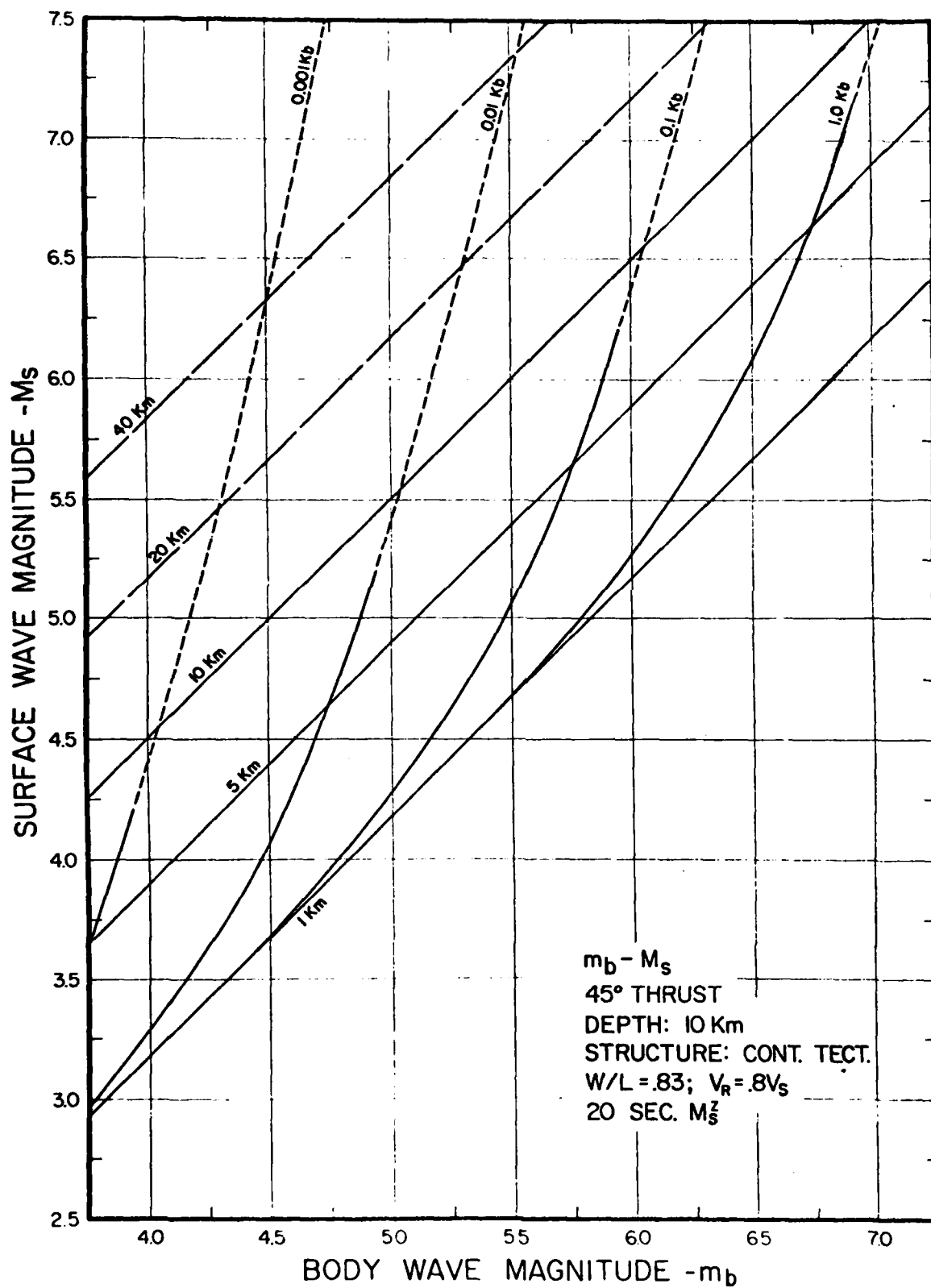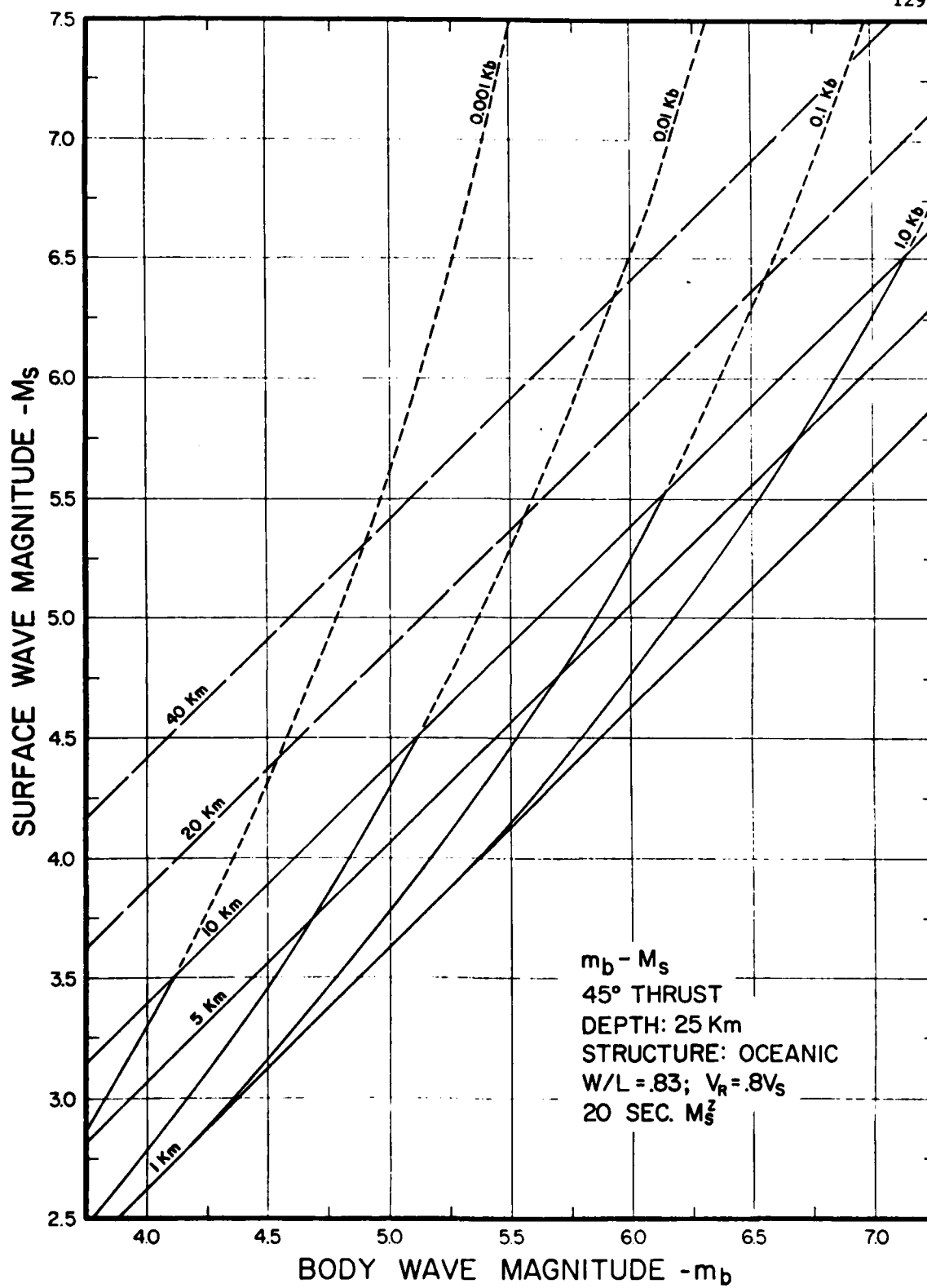
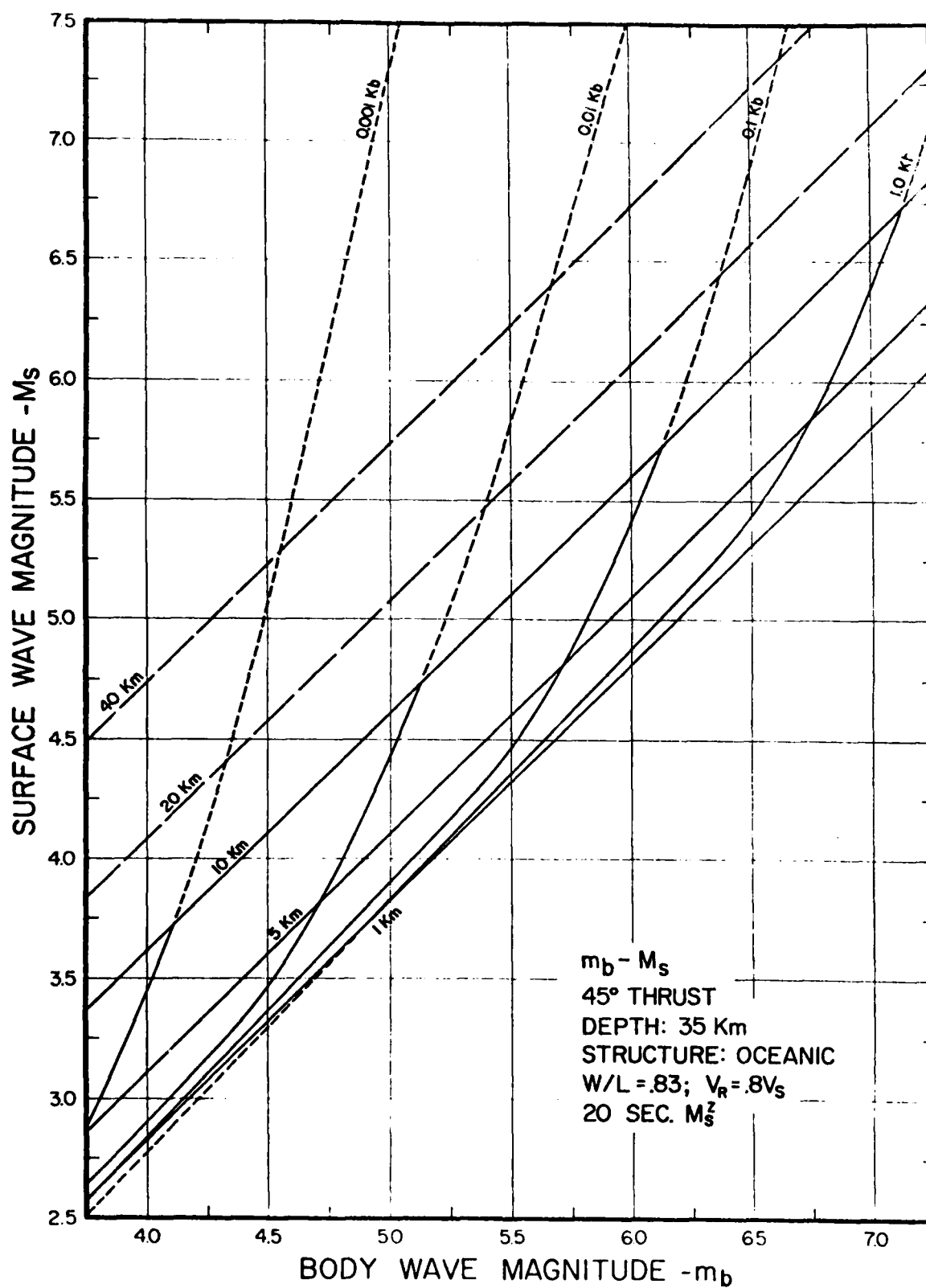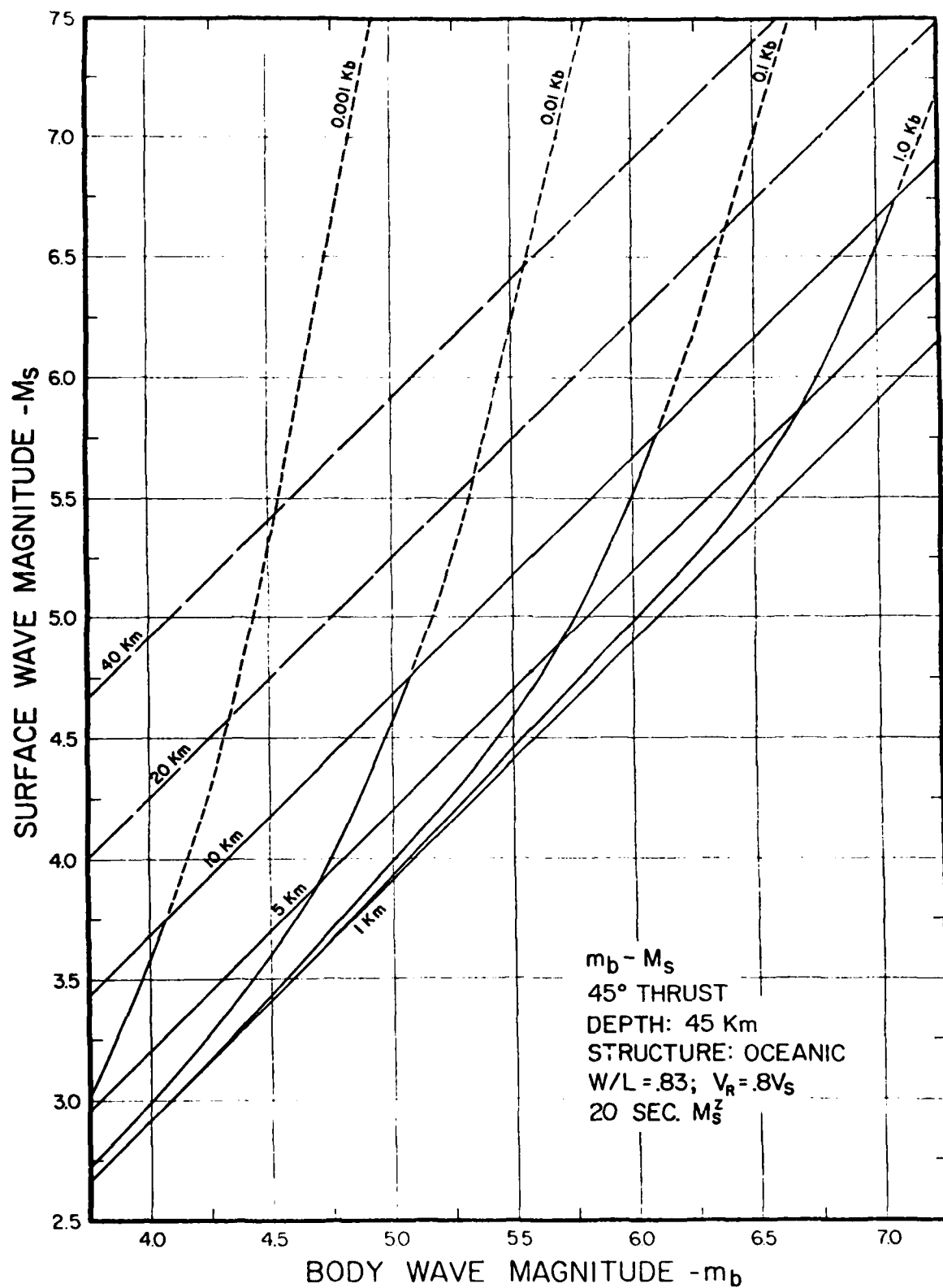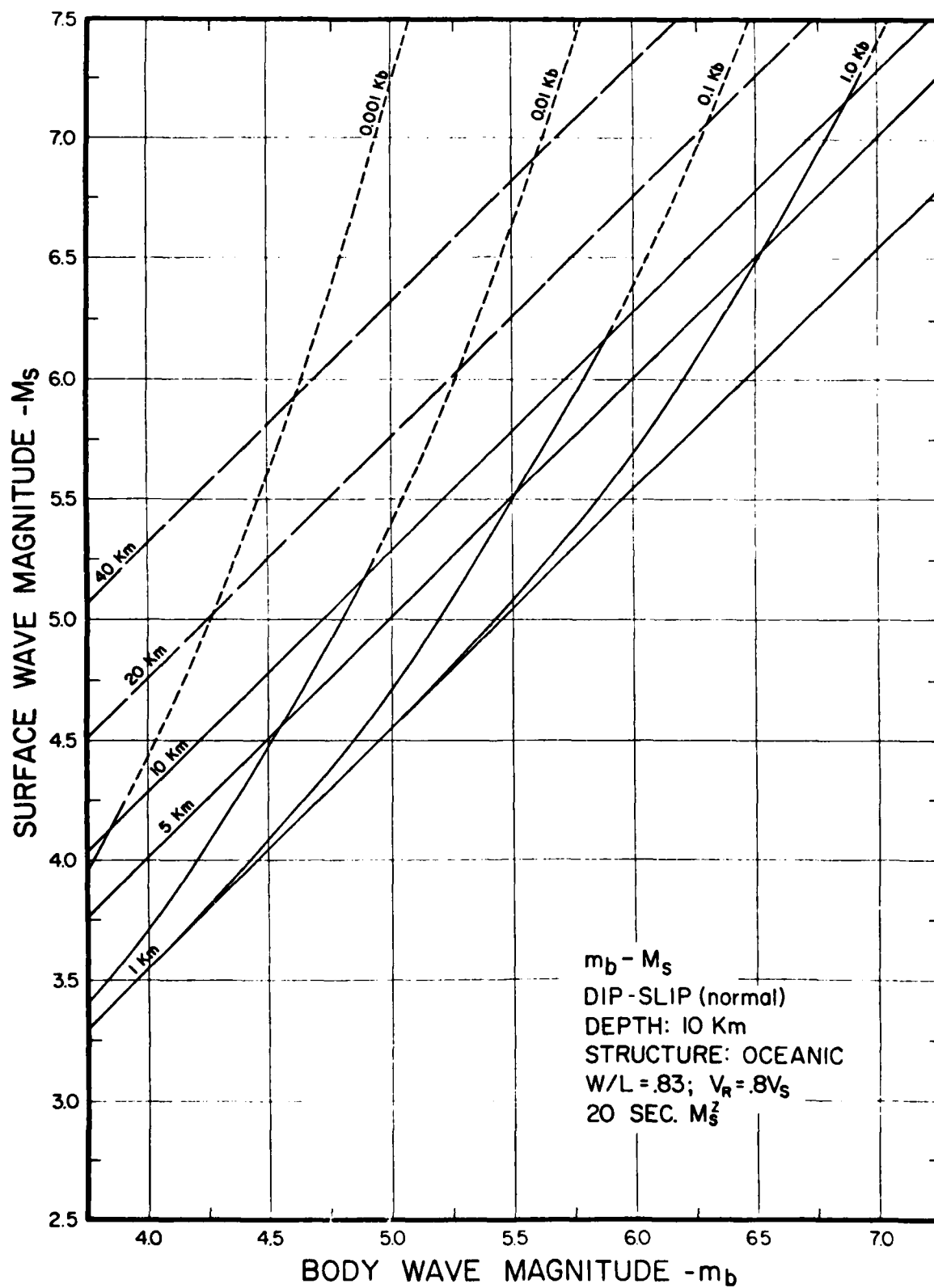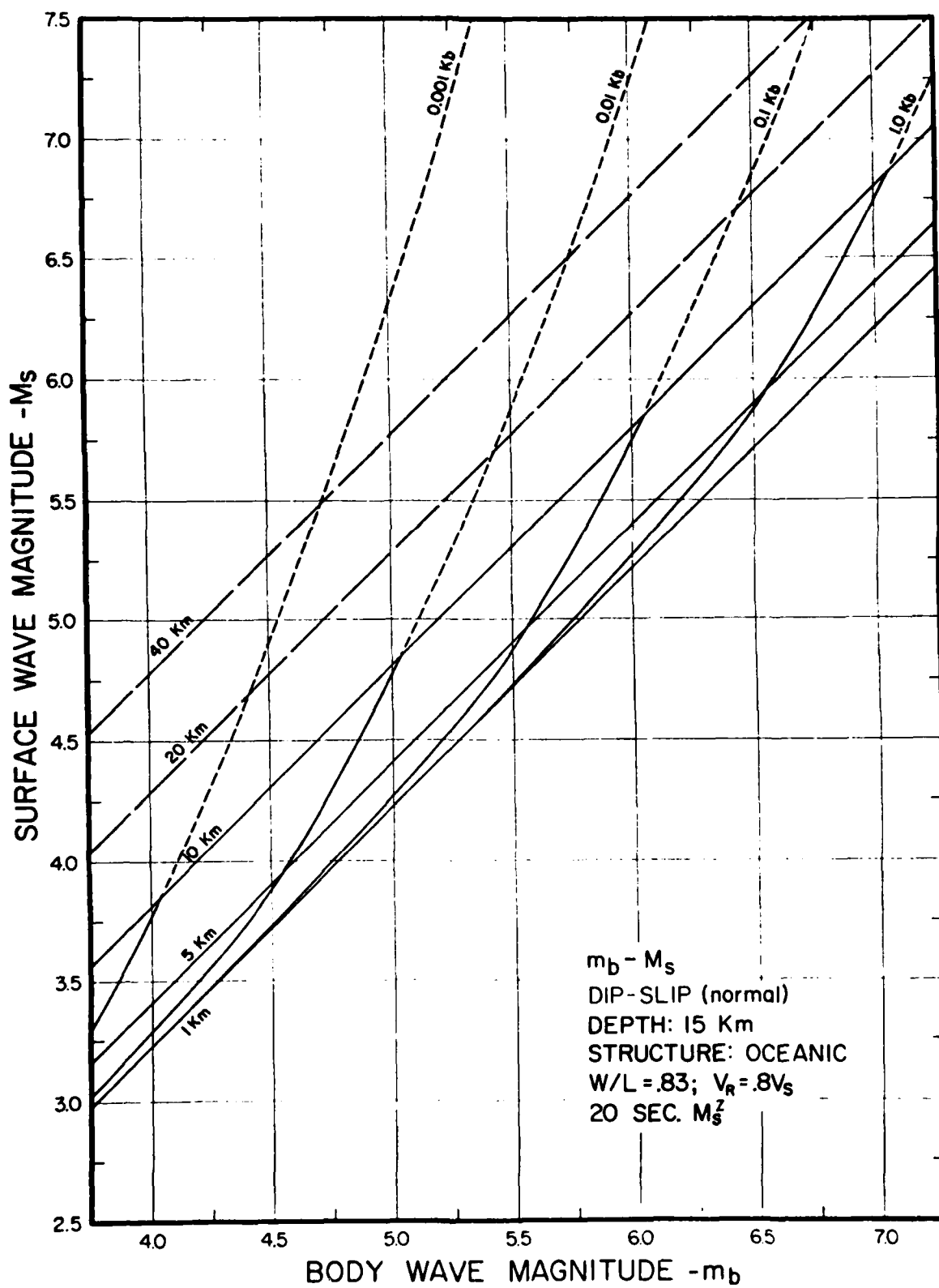Figure 1-a.
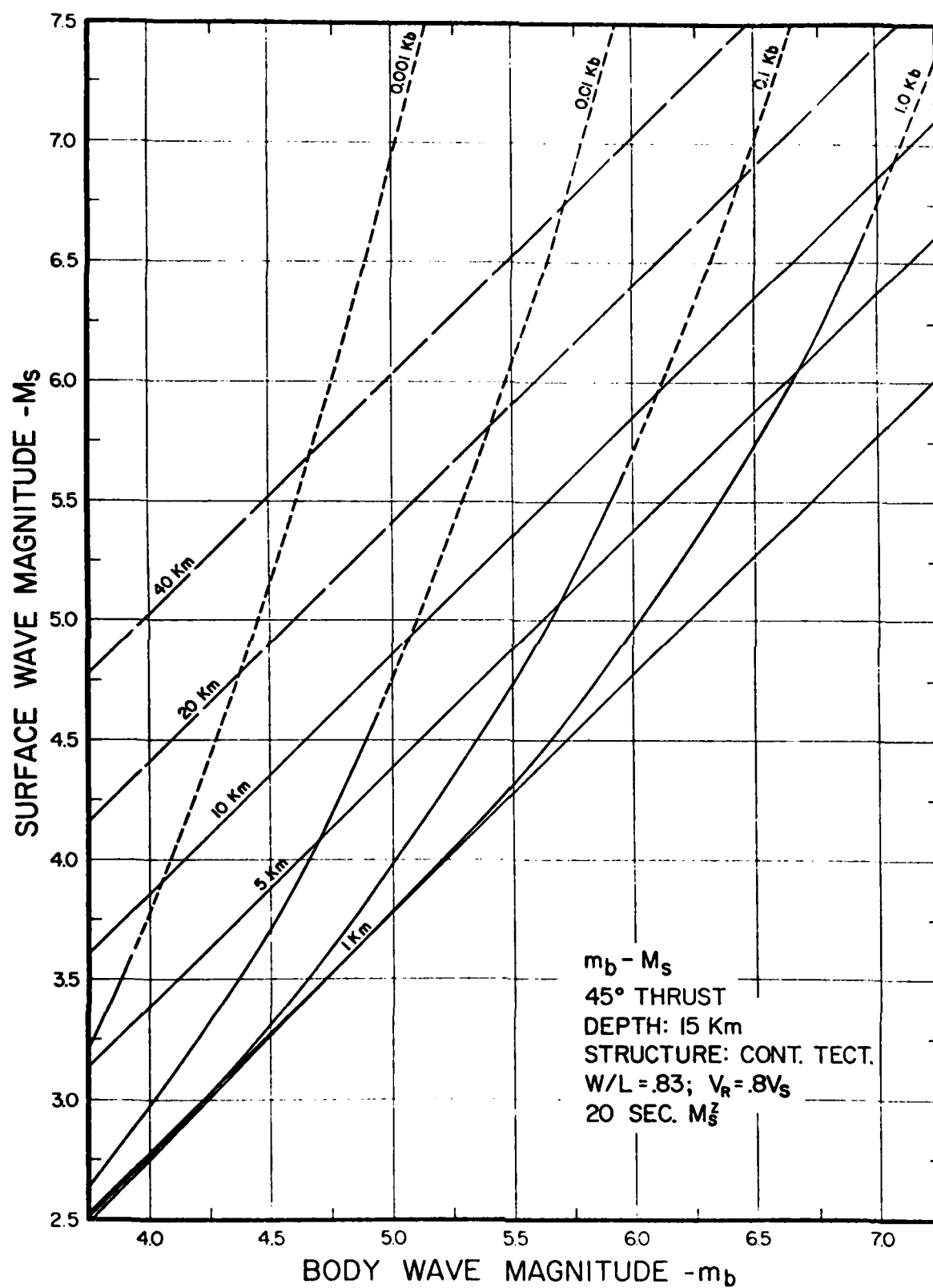
Figure 1-b.
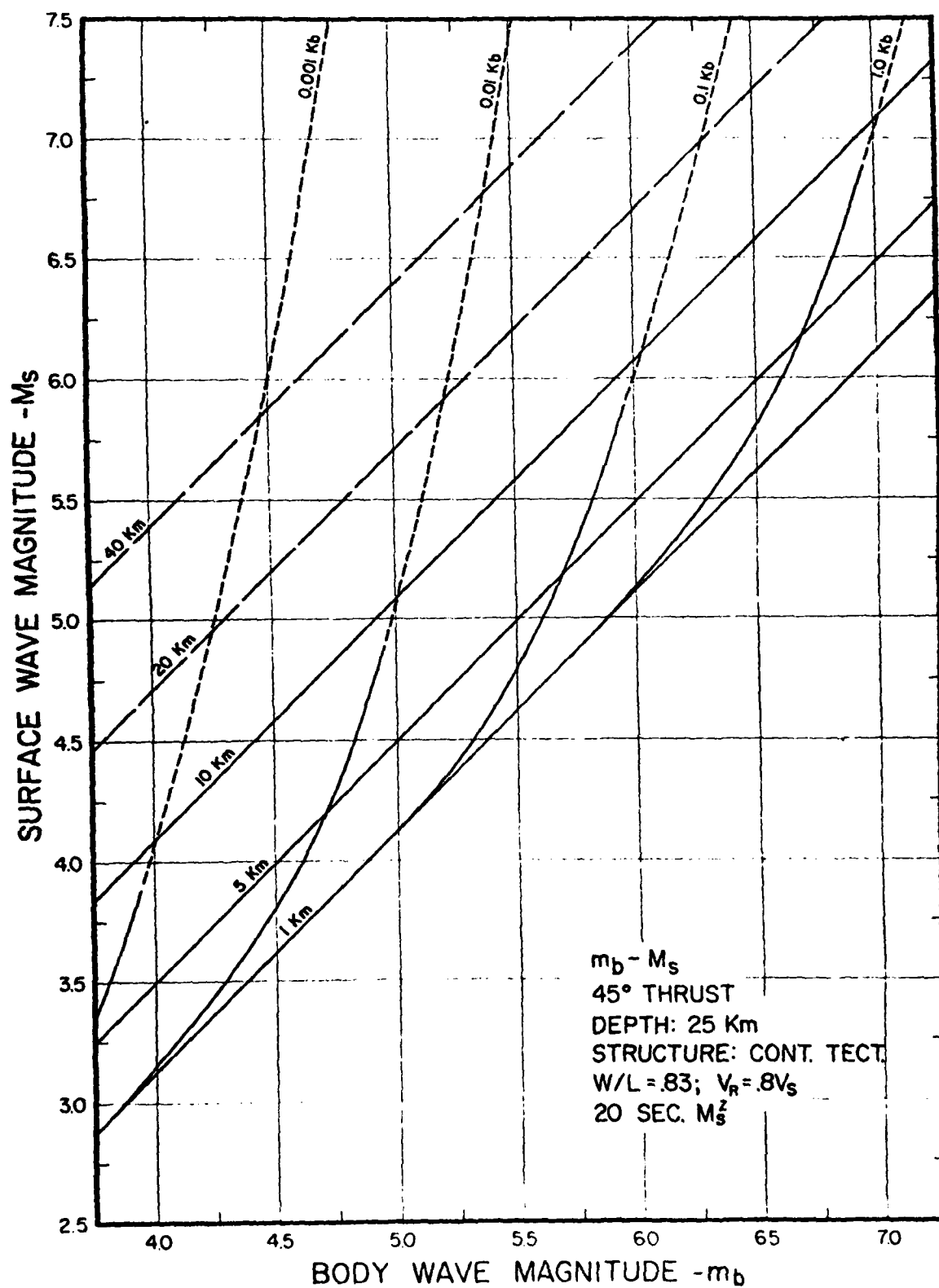
Figure 1-c.
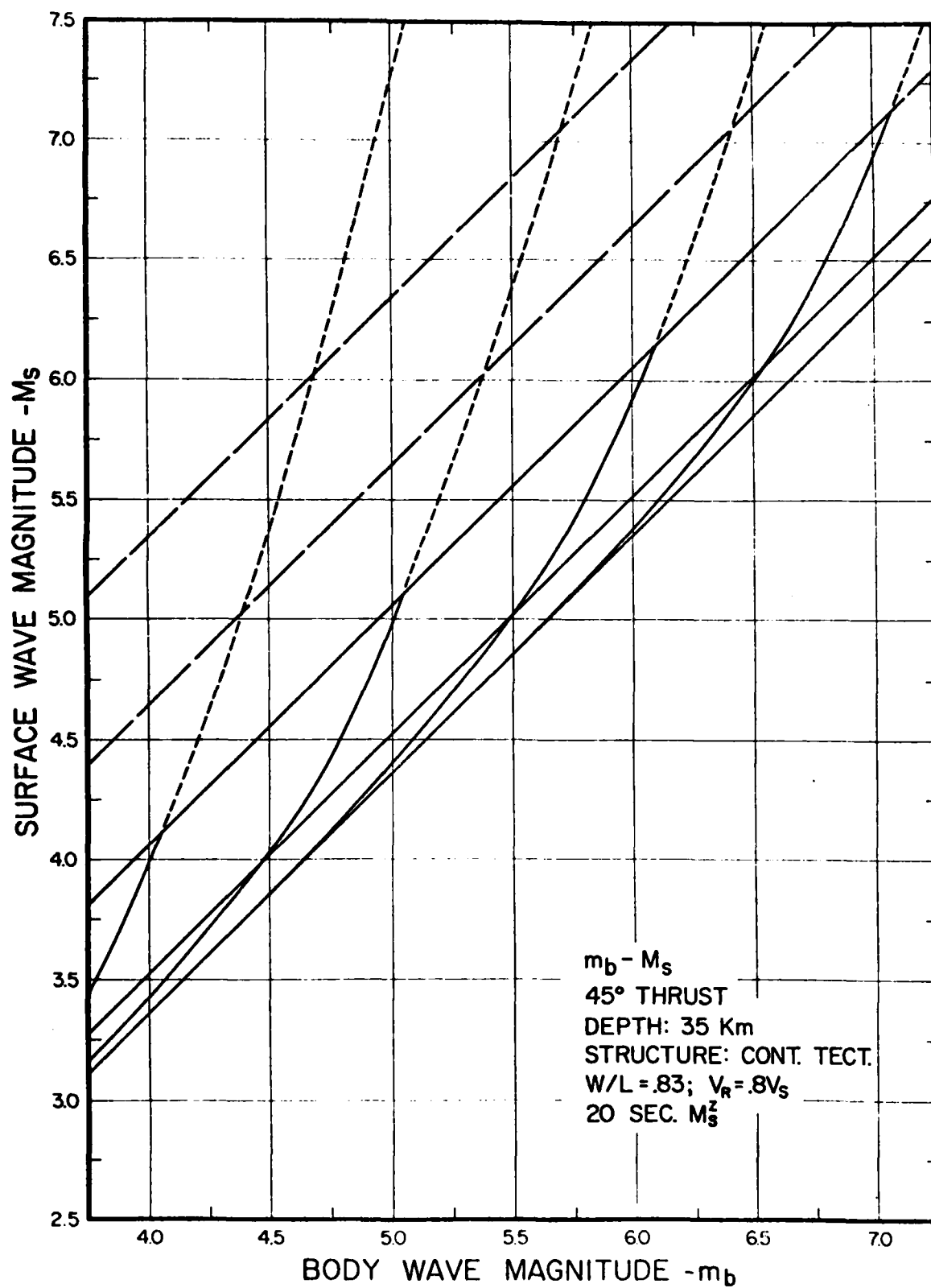
Figure 1-d.

Figure 1-e.

116
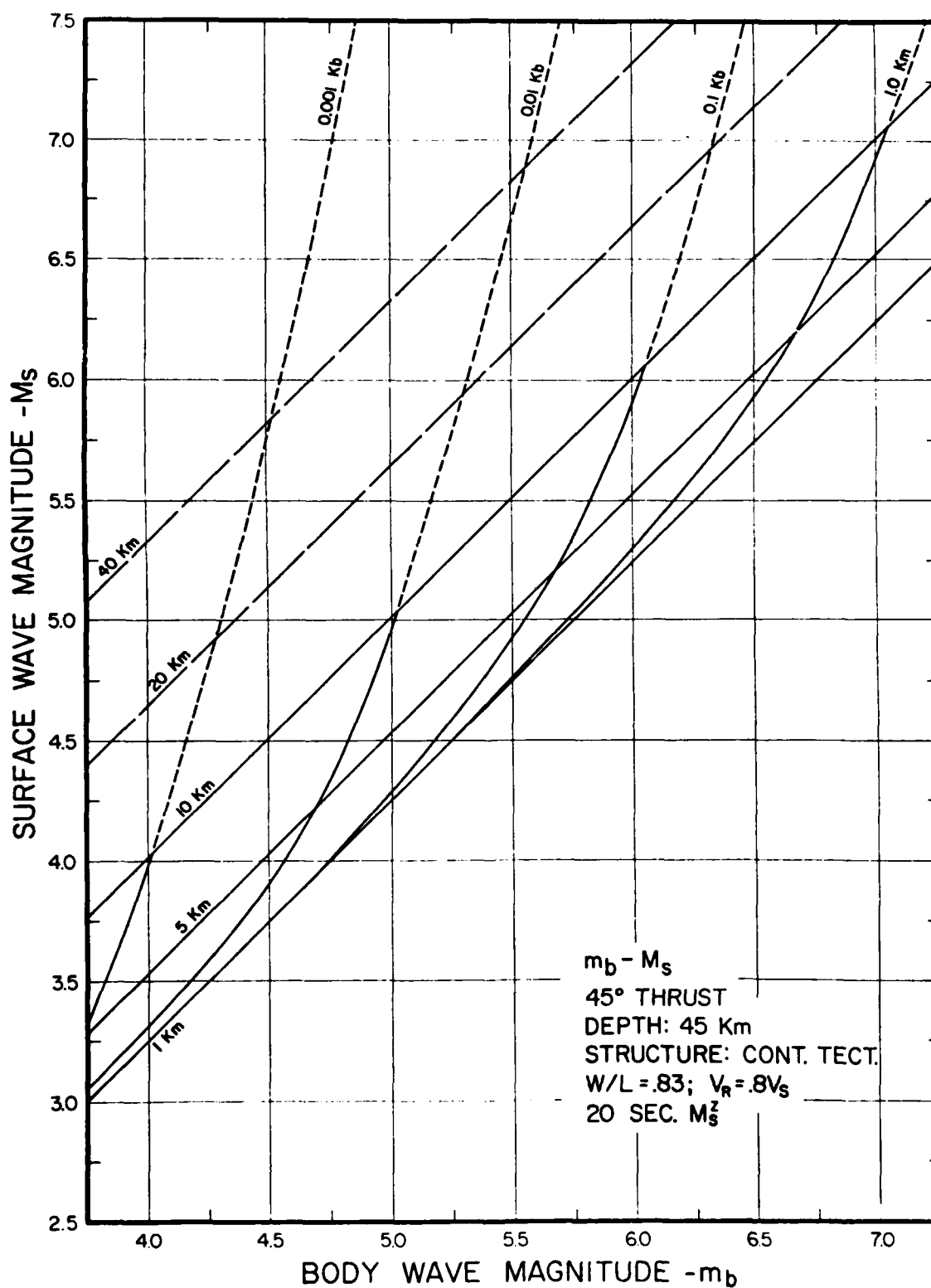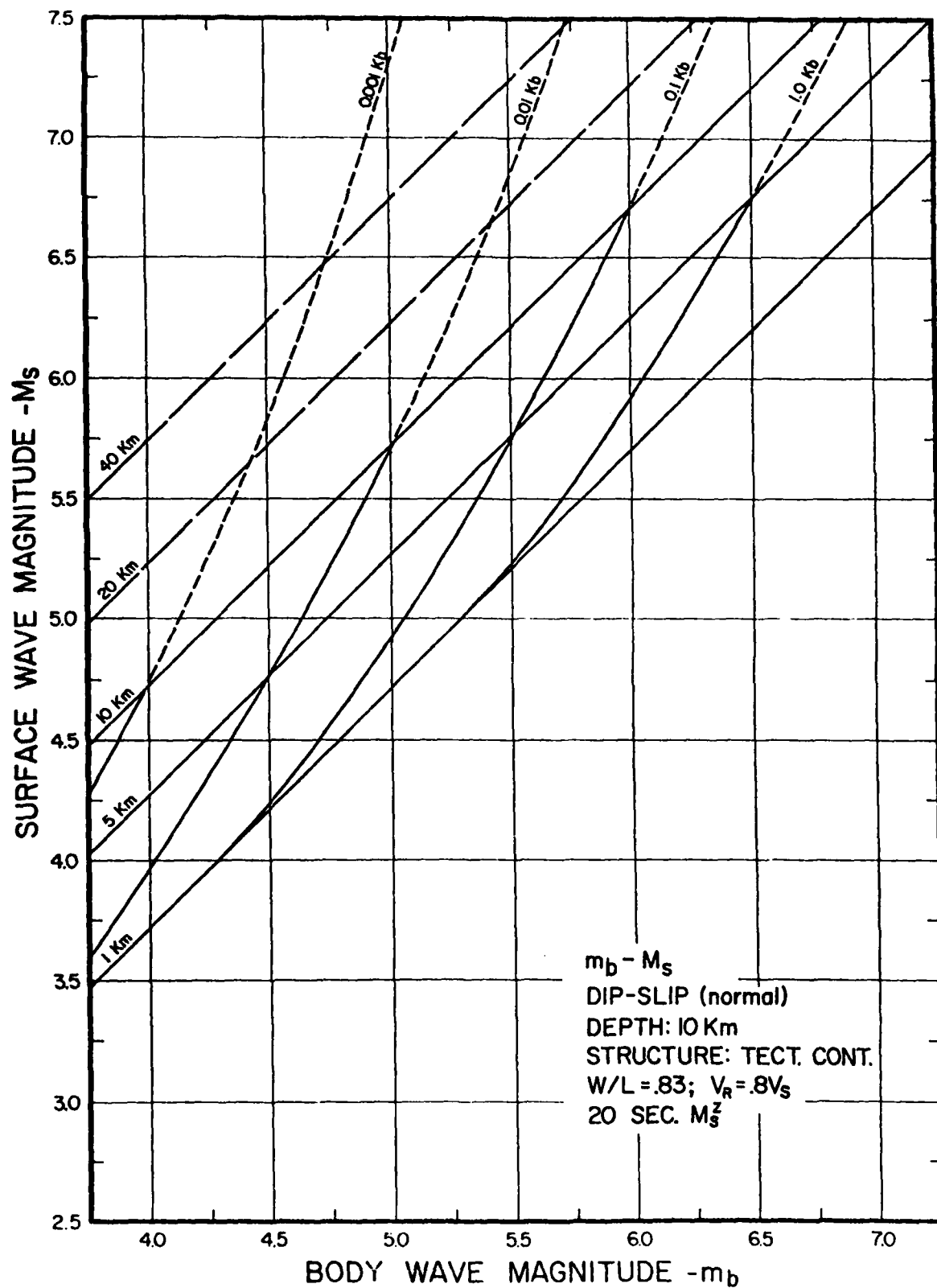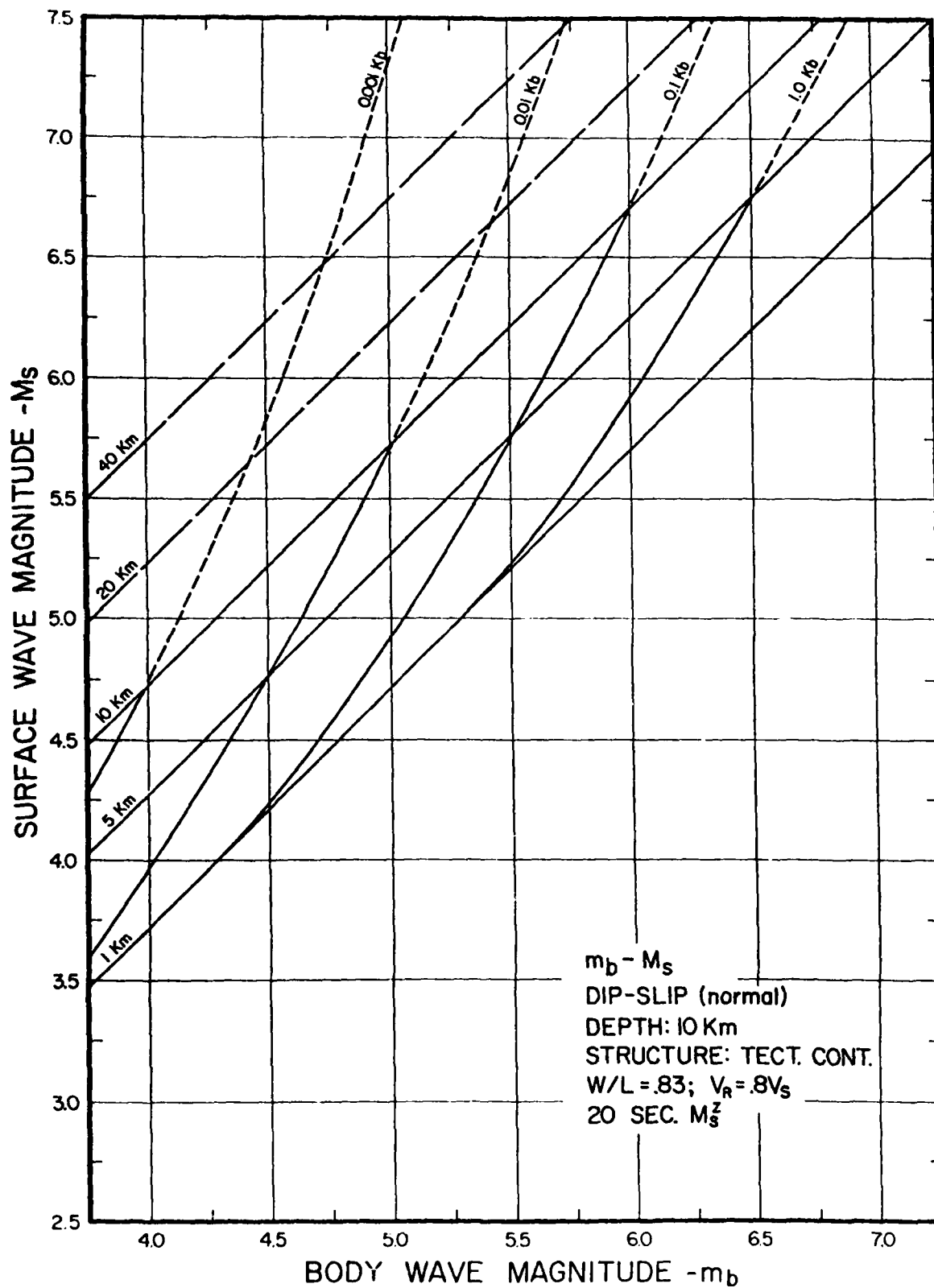
Figure 2-a.

Figure 2-a.

Figure 2-b.

Figure 2-c.

SURFACE WAVE MAGNITUDE -M_S

BODY WAVE MAGNITUDE -m_b

$m_b - M_s$
DIP-SLIP (normal)
DEPTH: 35 Km
STRUCTURE: TECT. CONT.
W/L =.83; V_R=.8V_S
20 SEC. M_s^z

0.001 Kb
0.01 Kb
0.1 Kb
1.0 Kb

40 Km
20 Km
10 Km
5 Km
1 Km
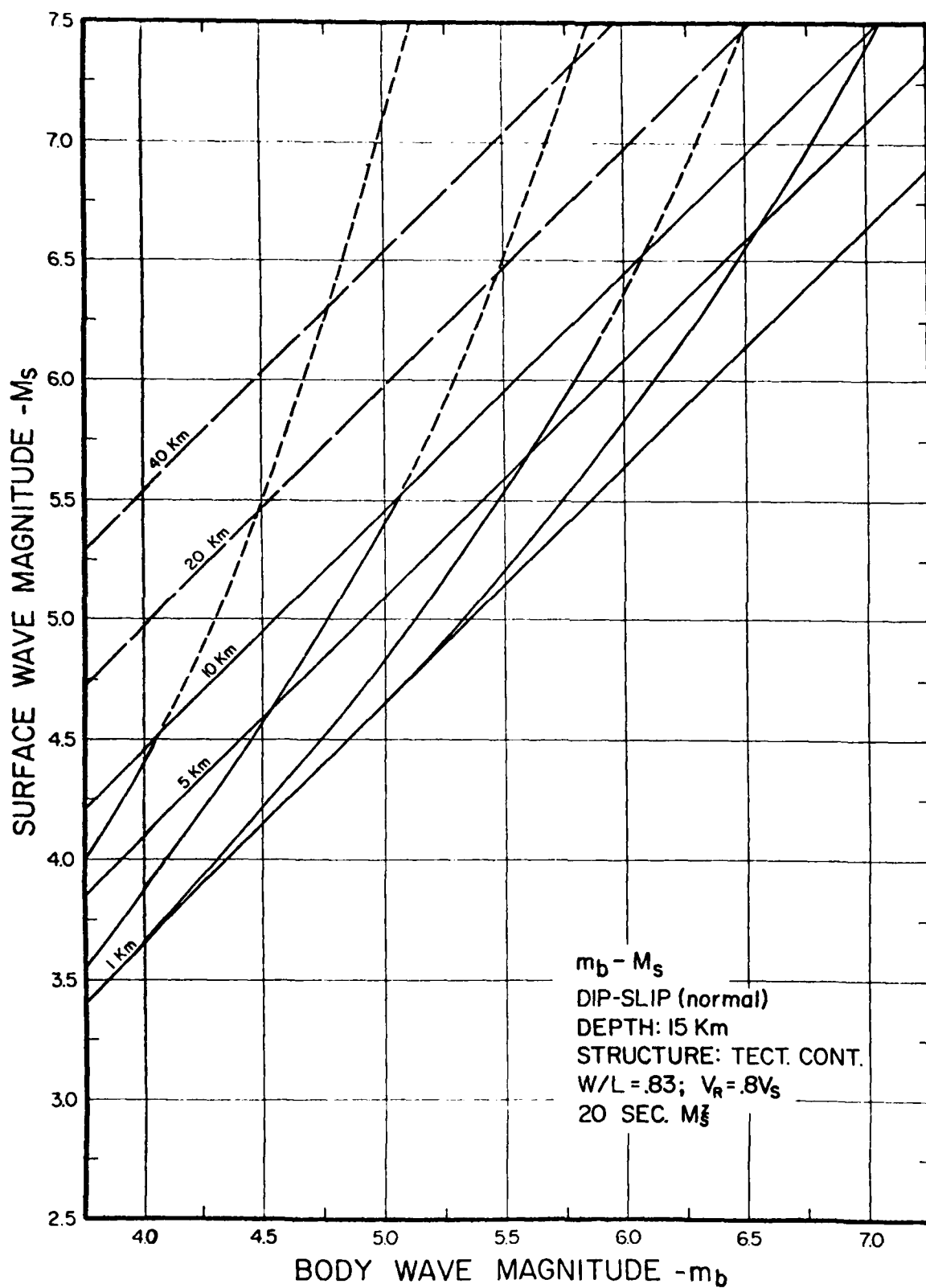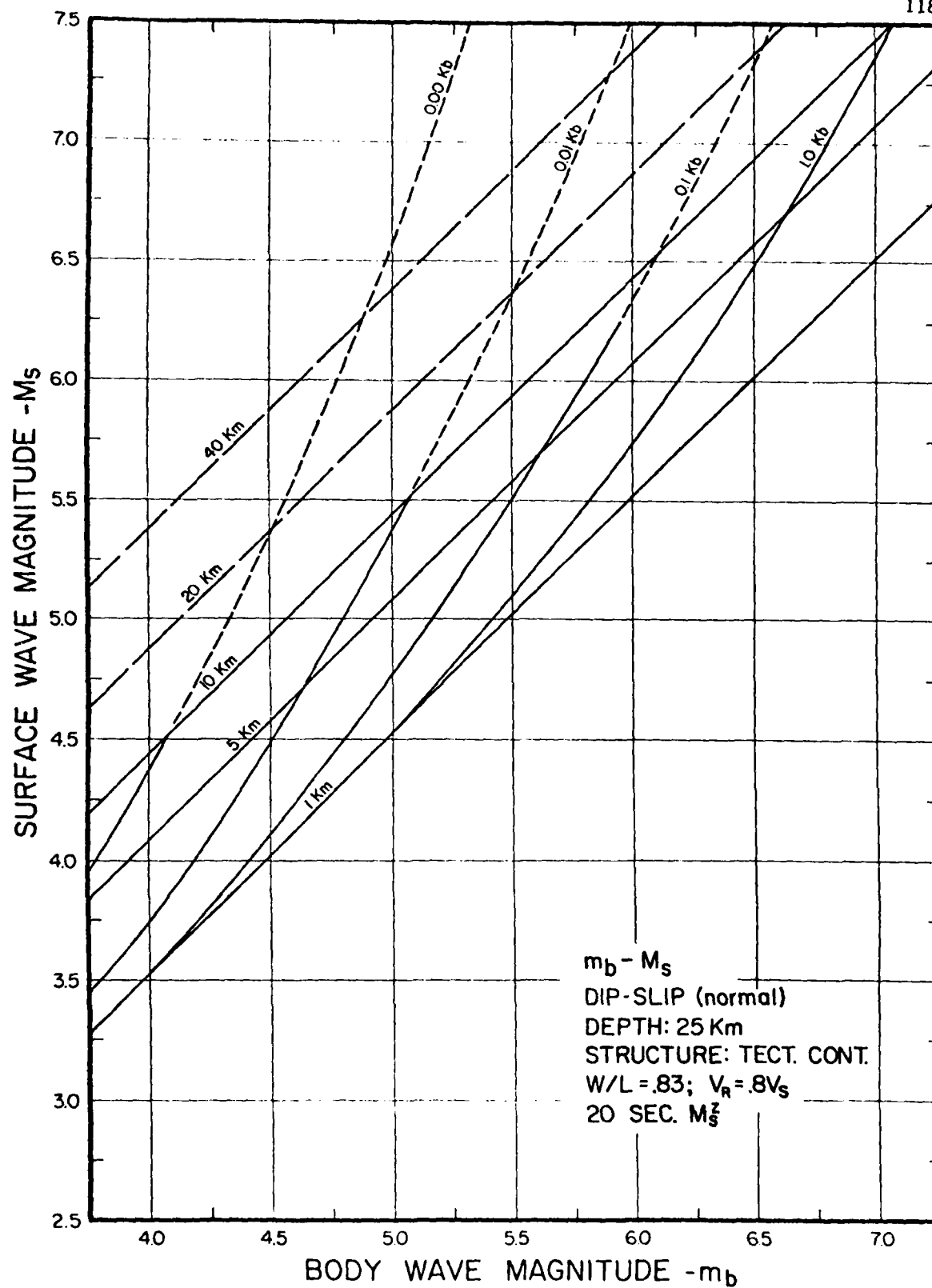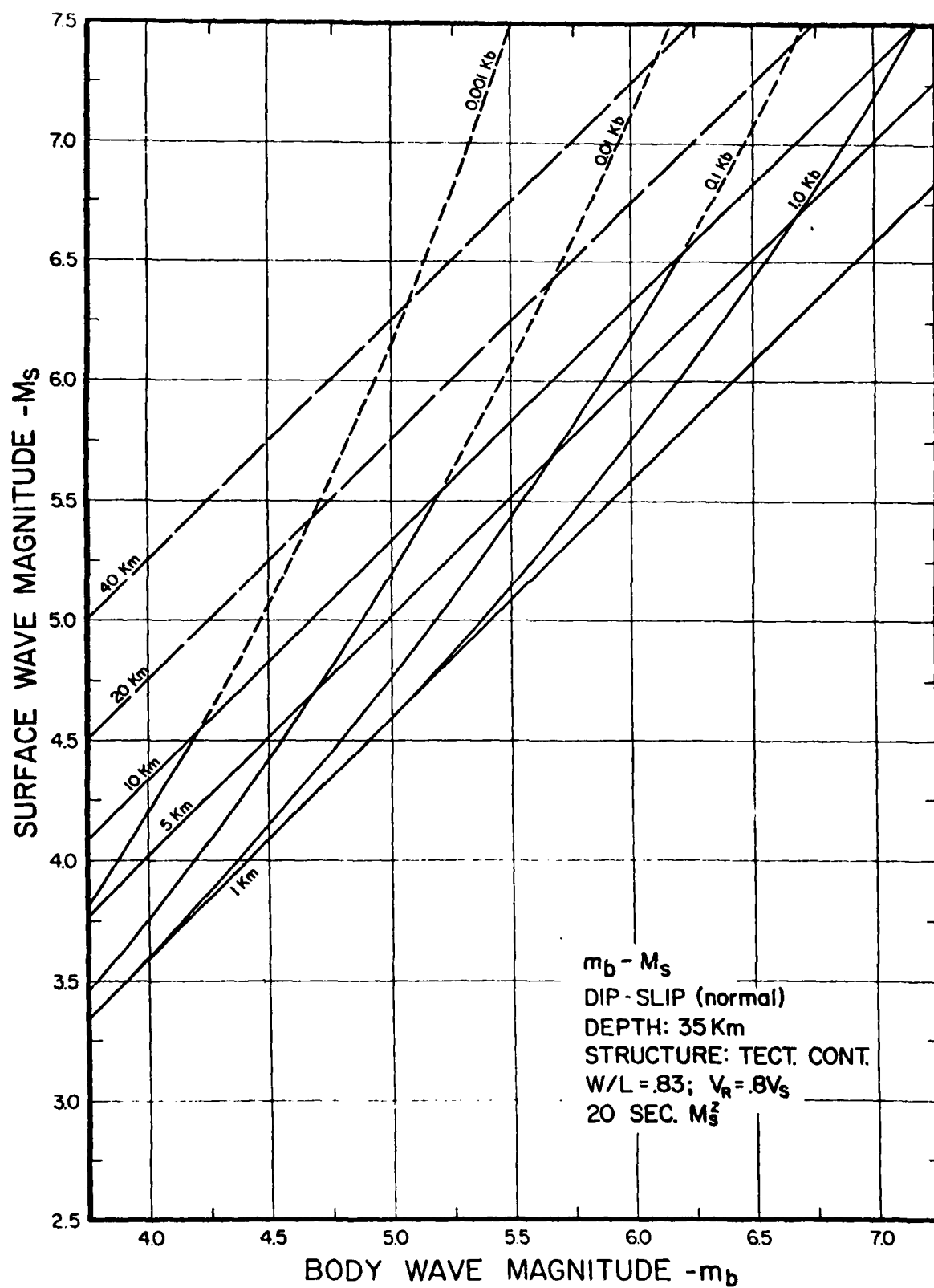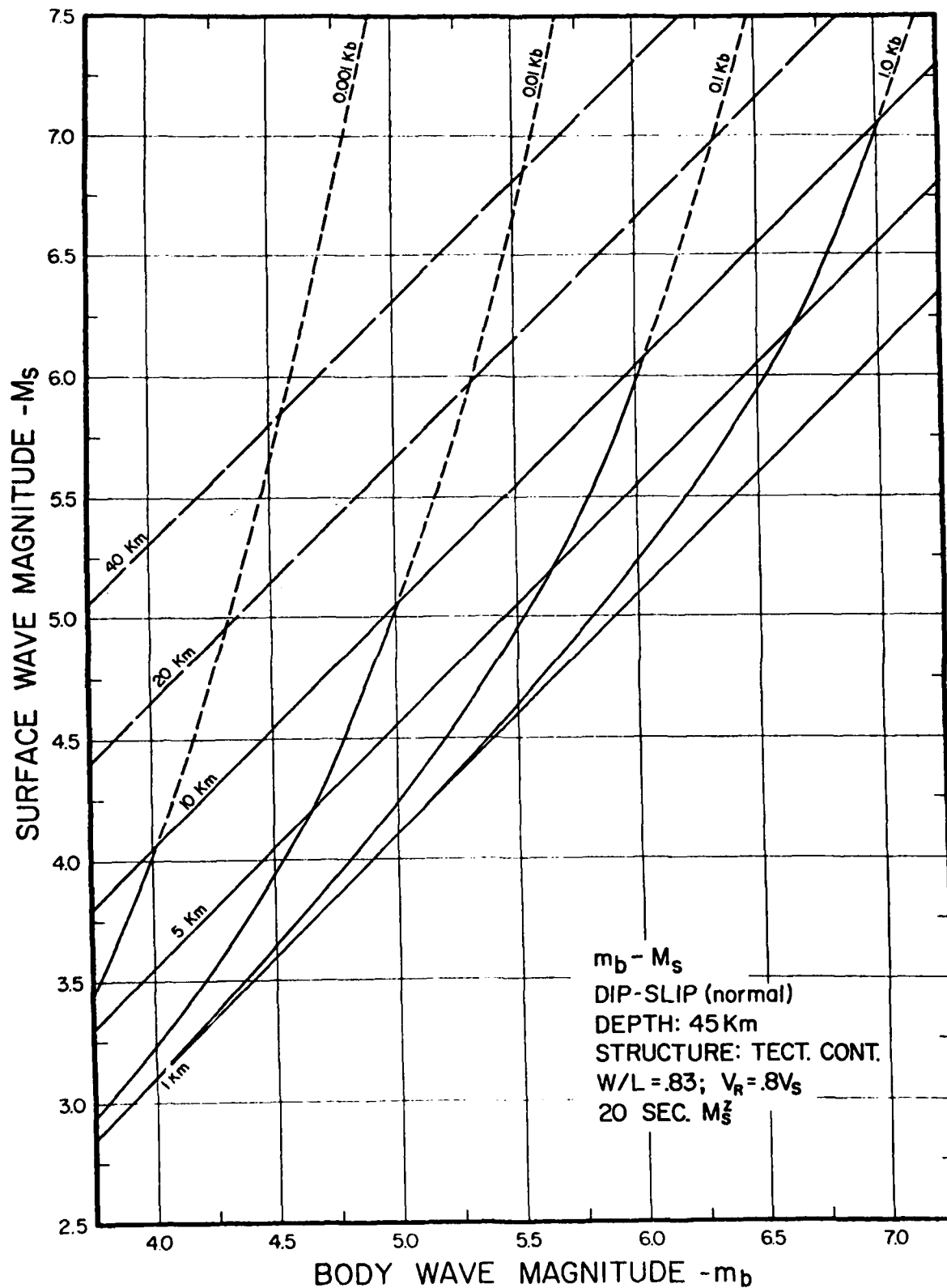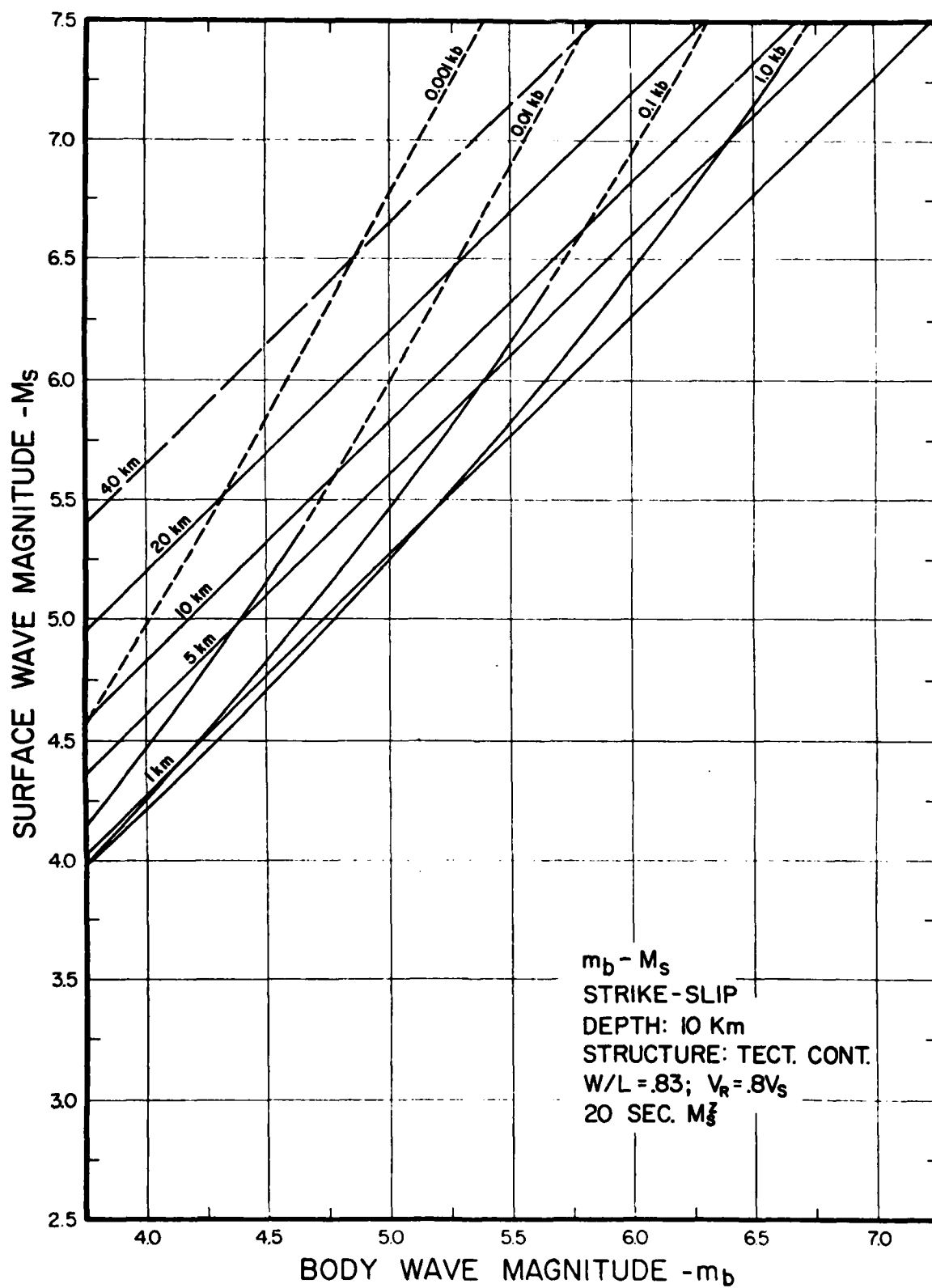
Figure 2-d.

Figure 2-e.

Figure 3-a.

Figure 3-b.

123

Figure 3-c.

124
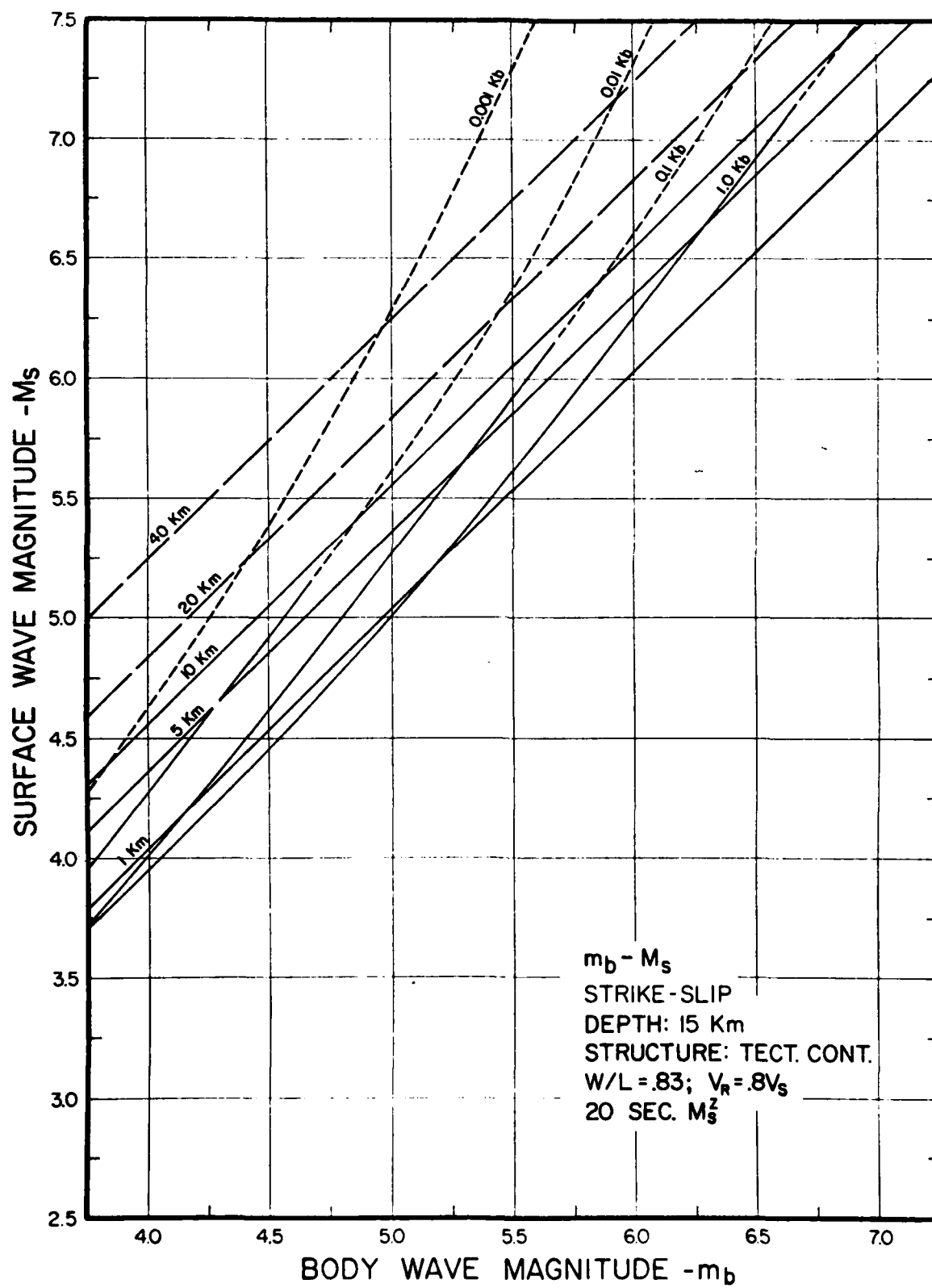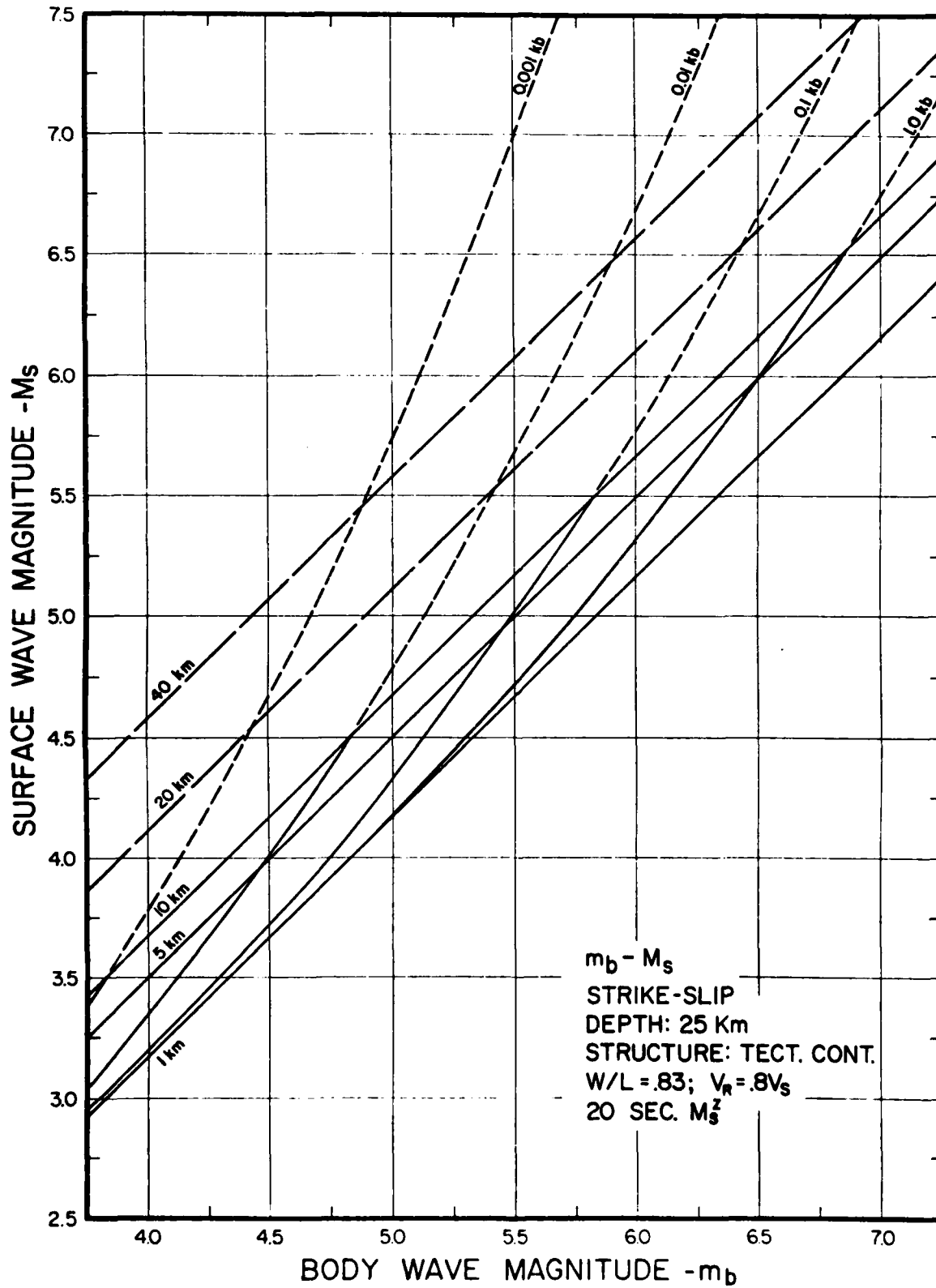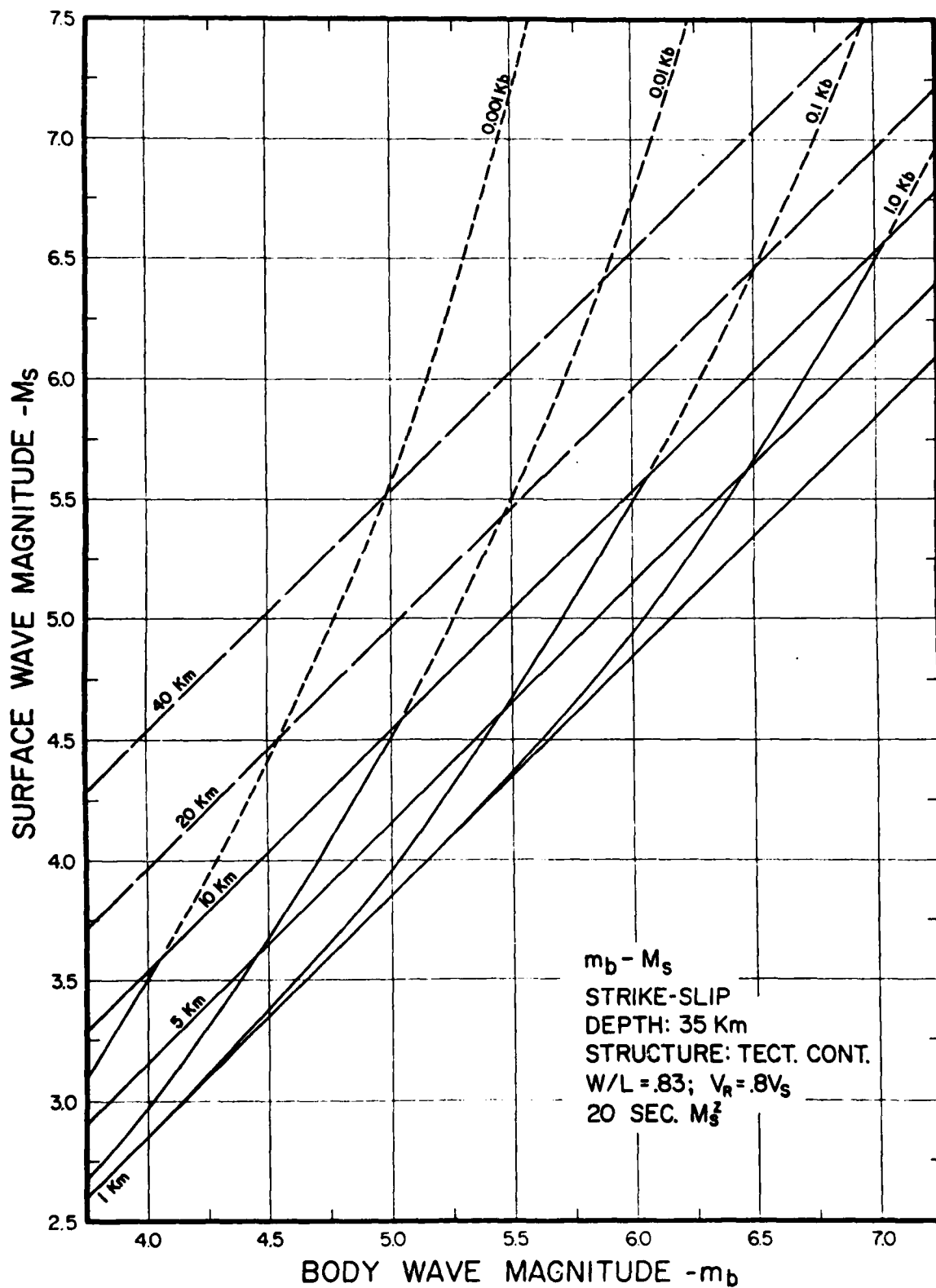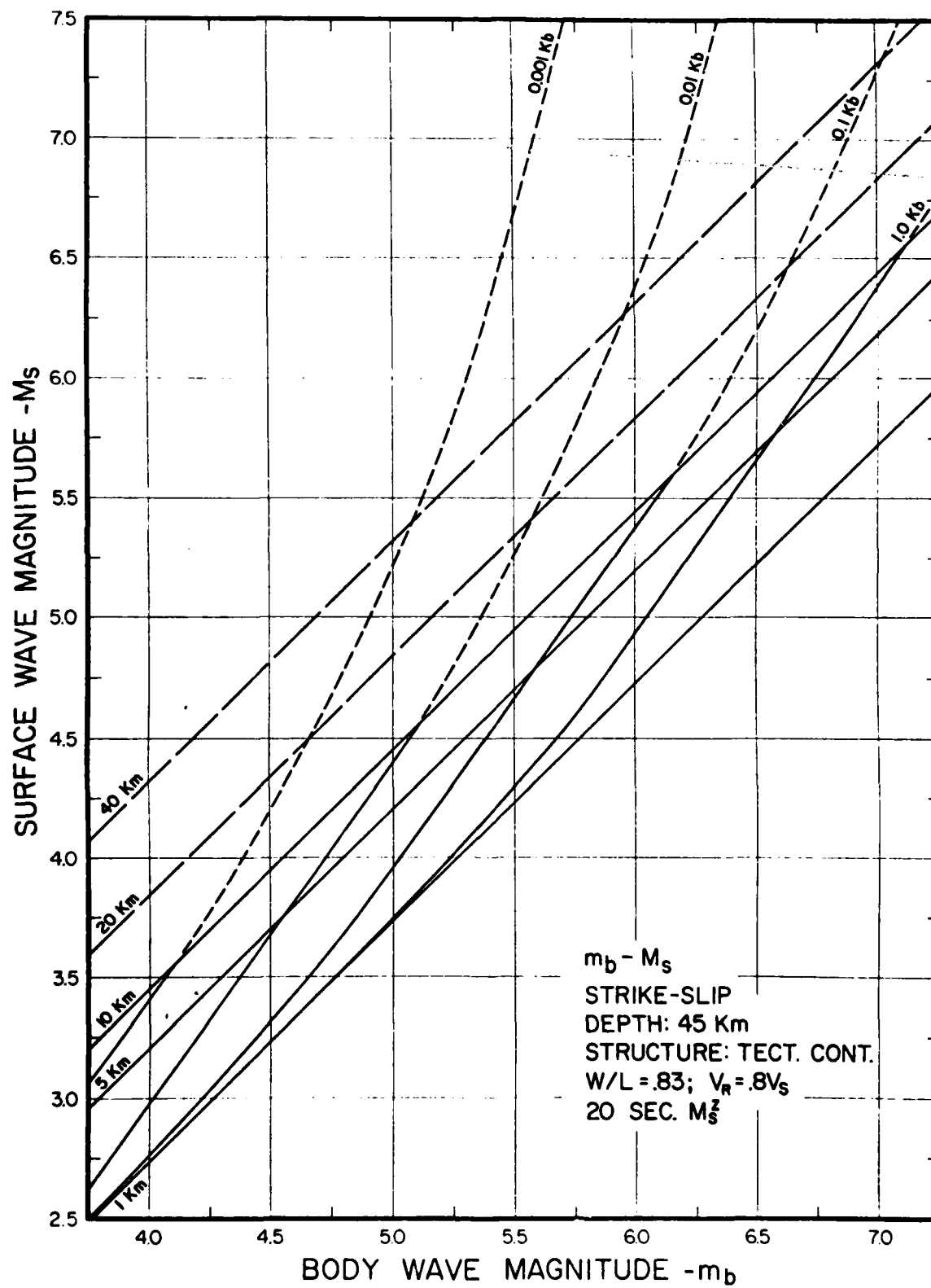
Figure 3-d.

Figure 3-e.

B. Theoretical m_b *vs* M_s curves for Thrust, Dip Slip and Strike slip events
    in Island Arc type *oceanic structure*.

Figure 4-a. Thrust (45°) events at a depth of 10 km.

Figure 4-b. Thrust (45°) events at a depth of 15 km.

Figure 4-c. Thrust (45°) events at a depth of 25 km.

Figure 4-d. Thrust (45°) events at a depth of 35 km.

Figure 4-e. Thrust (45°) events at a depth of 45 km.

Figure 5-a. Dip slip (normal) events at a depth of 10 km.

Figure 5-b. Dip slip (normal) events at a depth of 15 km.

Figure 5-c. Dip slip (normal) events at a depth of 25 km.

Figure 5-d. Dip slip (normal) events at a depth of 35 km.

Figure 5-e. Dip slip (normal) events at a depth of 45 km.

Figure 6-a. Strike-slip events at a depth of 10 km.

Figure 6-b. Strike-slip events at a depth of 15 km.

Figure 6-c. Strike-slip events at a depth of 25 km.

Figure 6-d. Strike-slip events at a depth of 45 km.
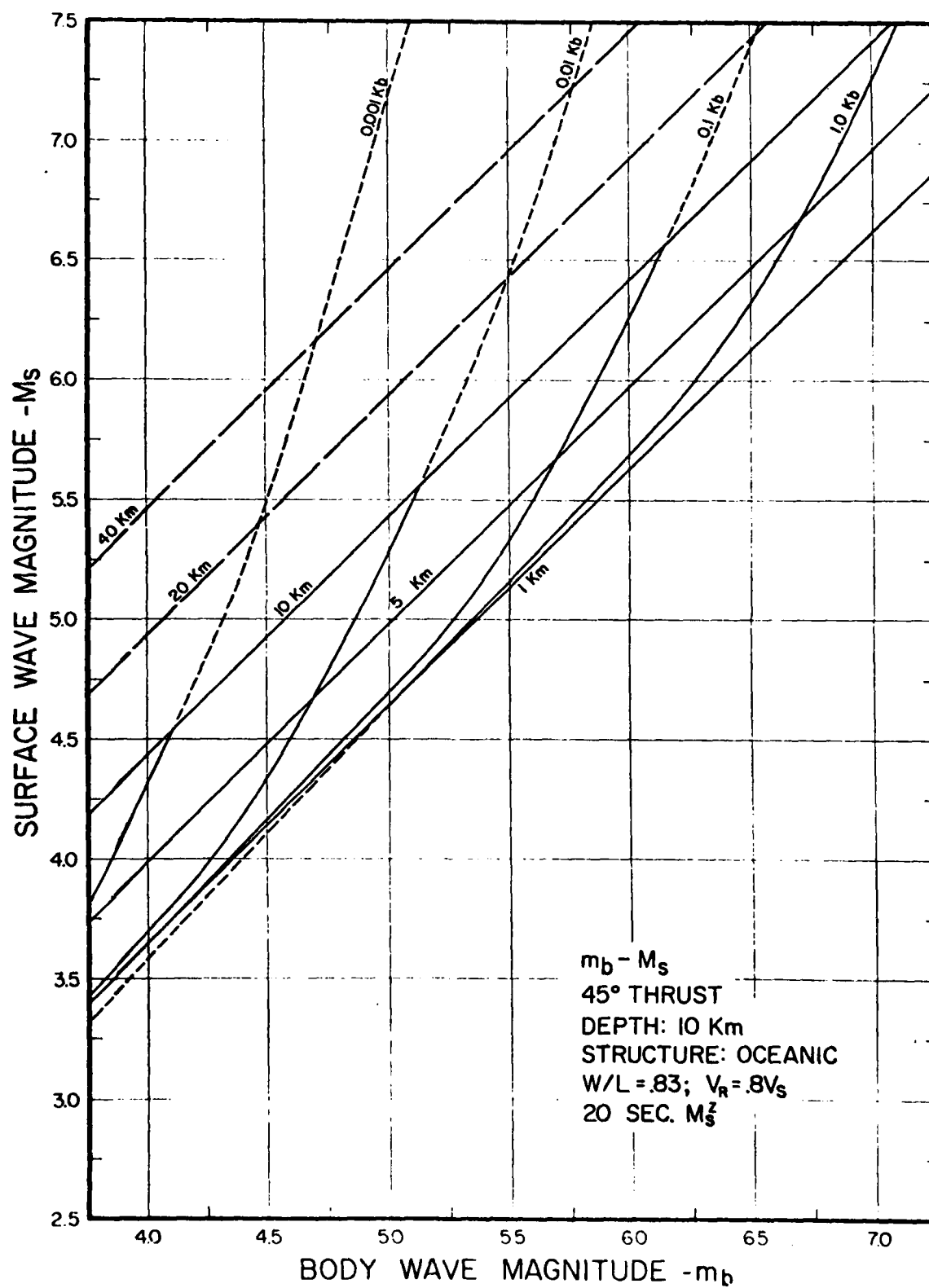
Figure 4-a.
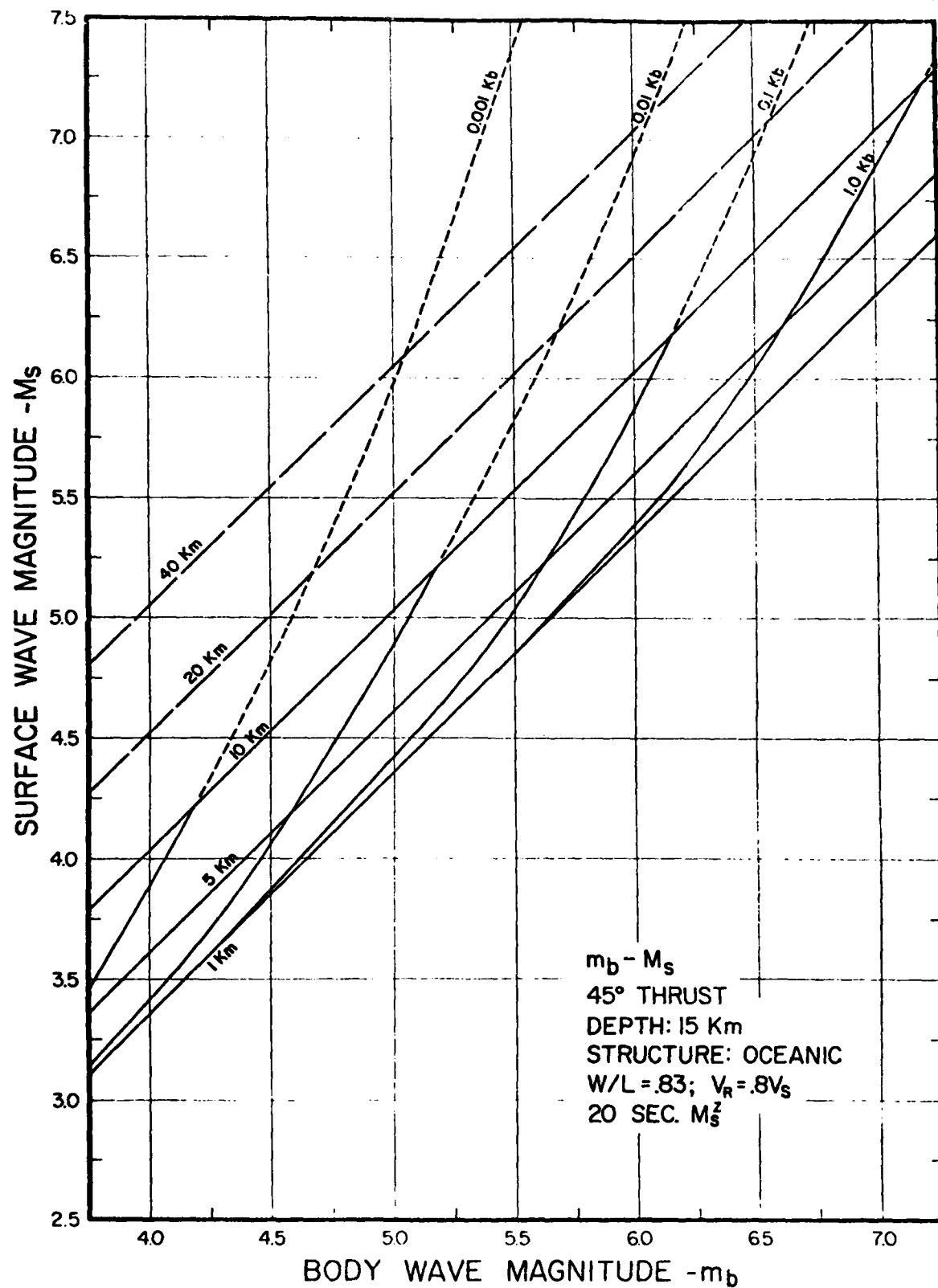
Figure 4-b.

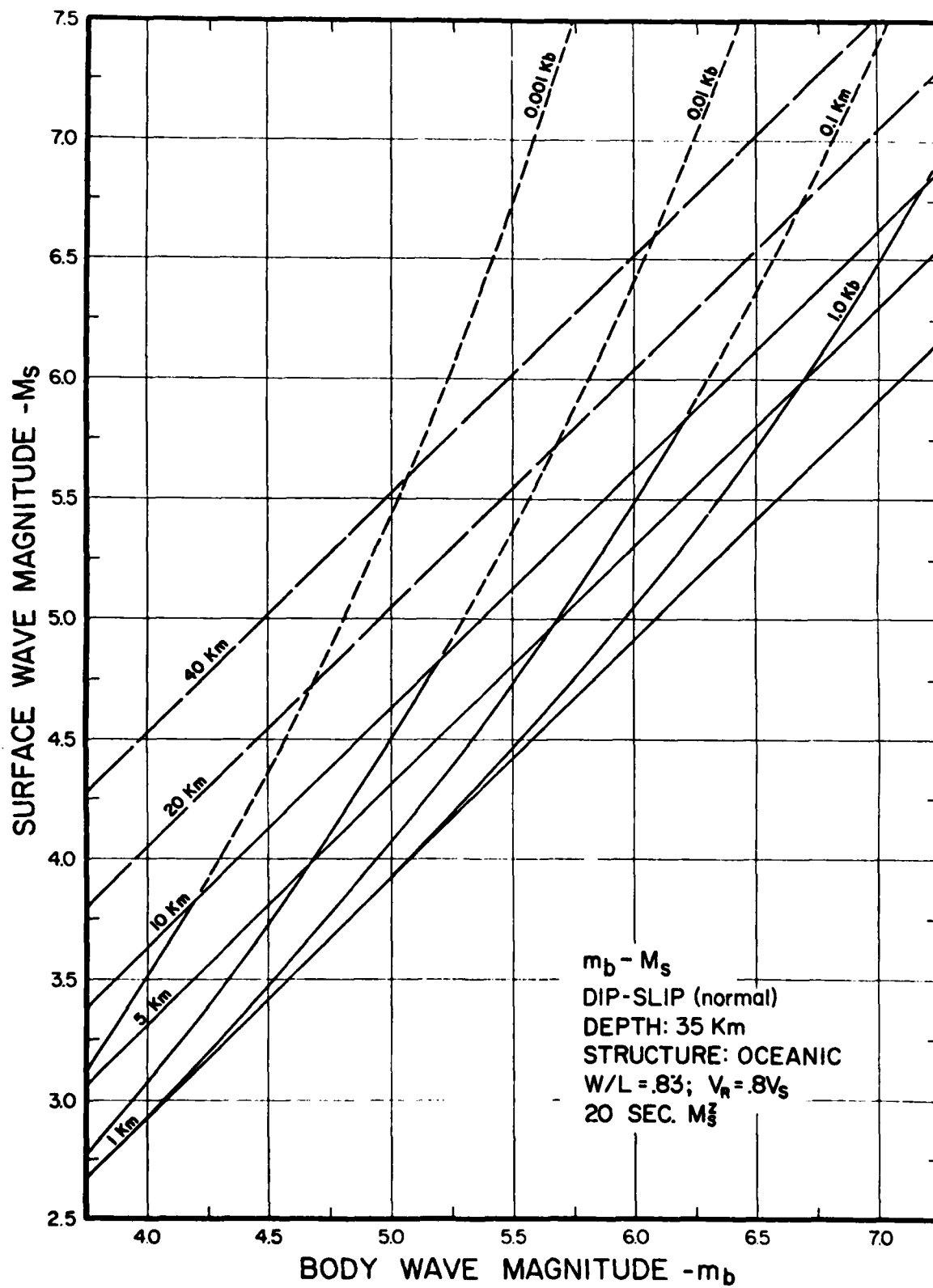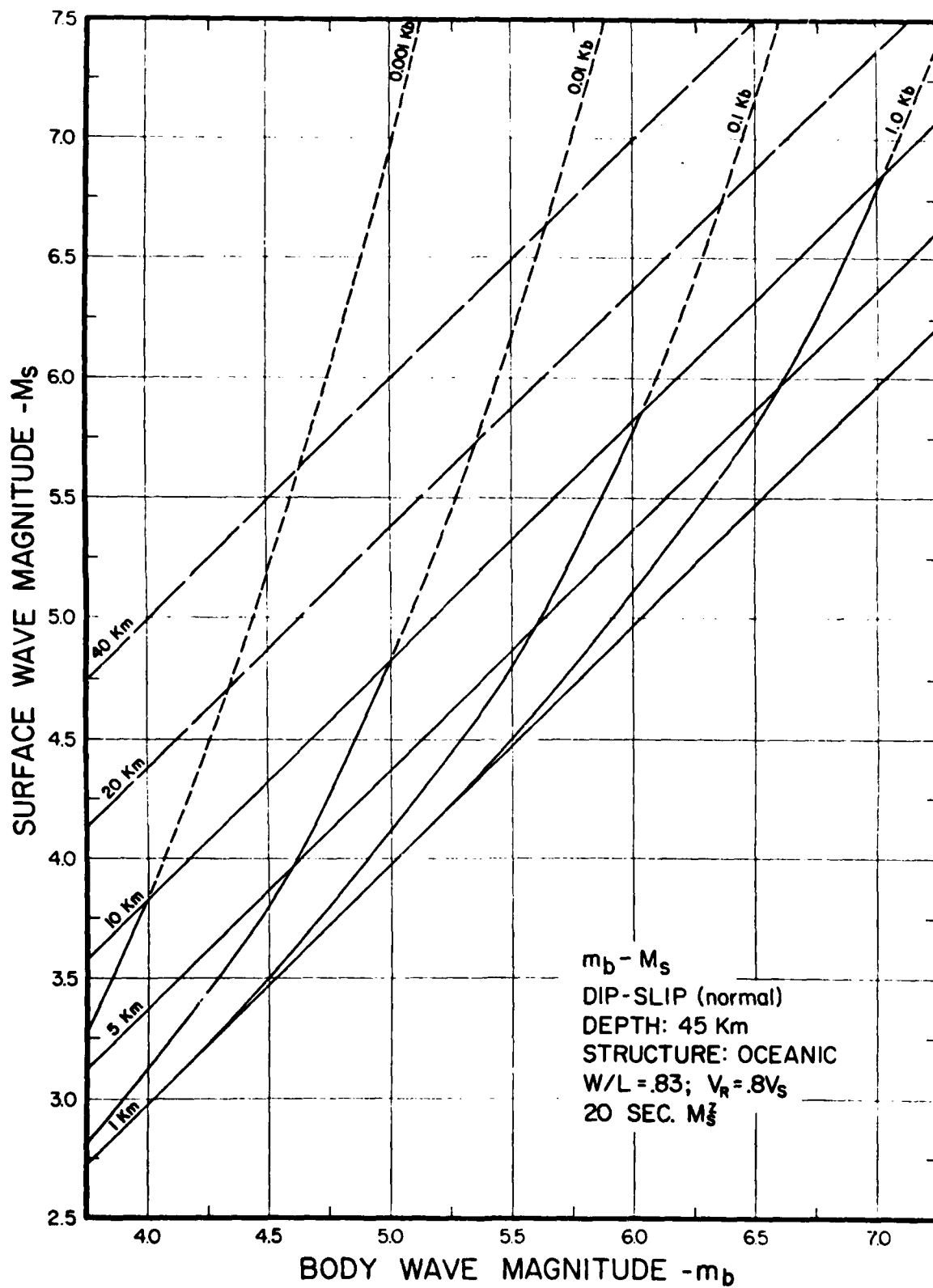Figure 4-c.

Figure 4-d.

Figure 4-e.
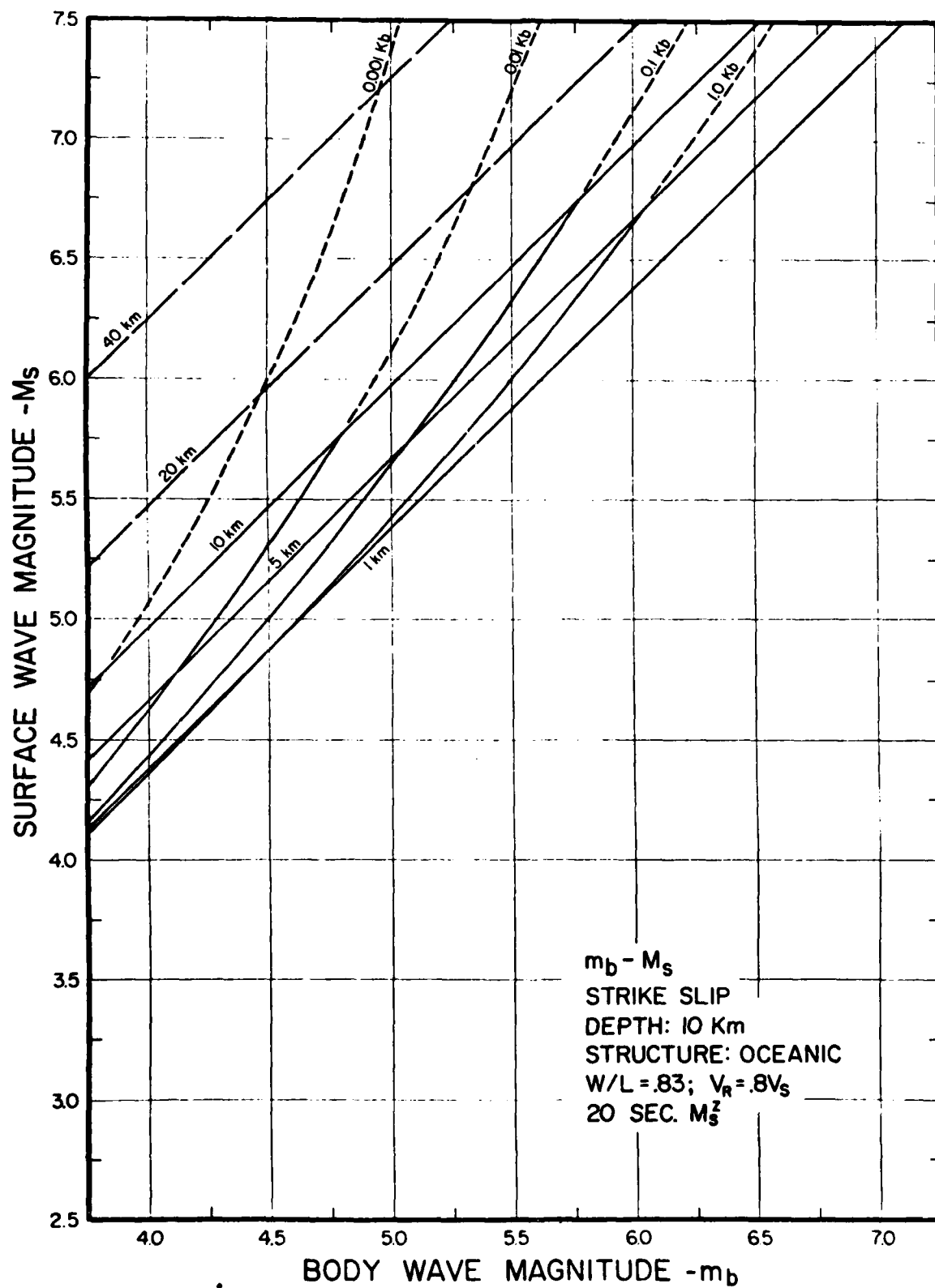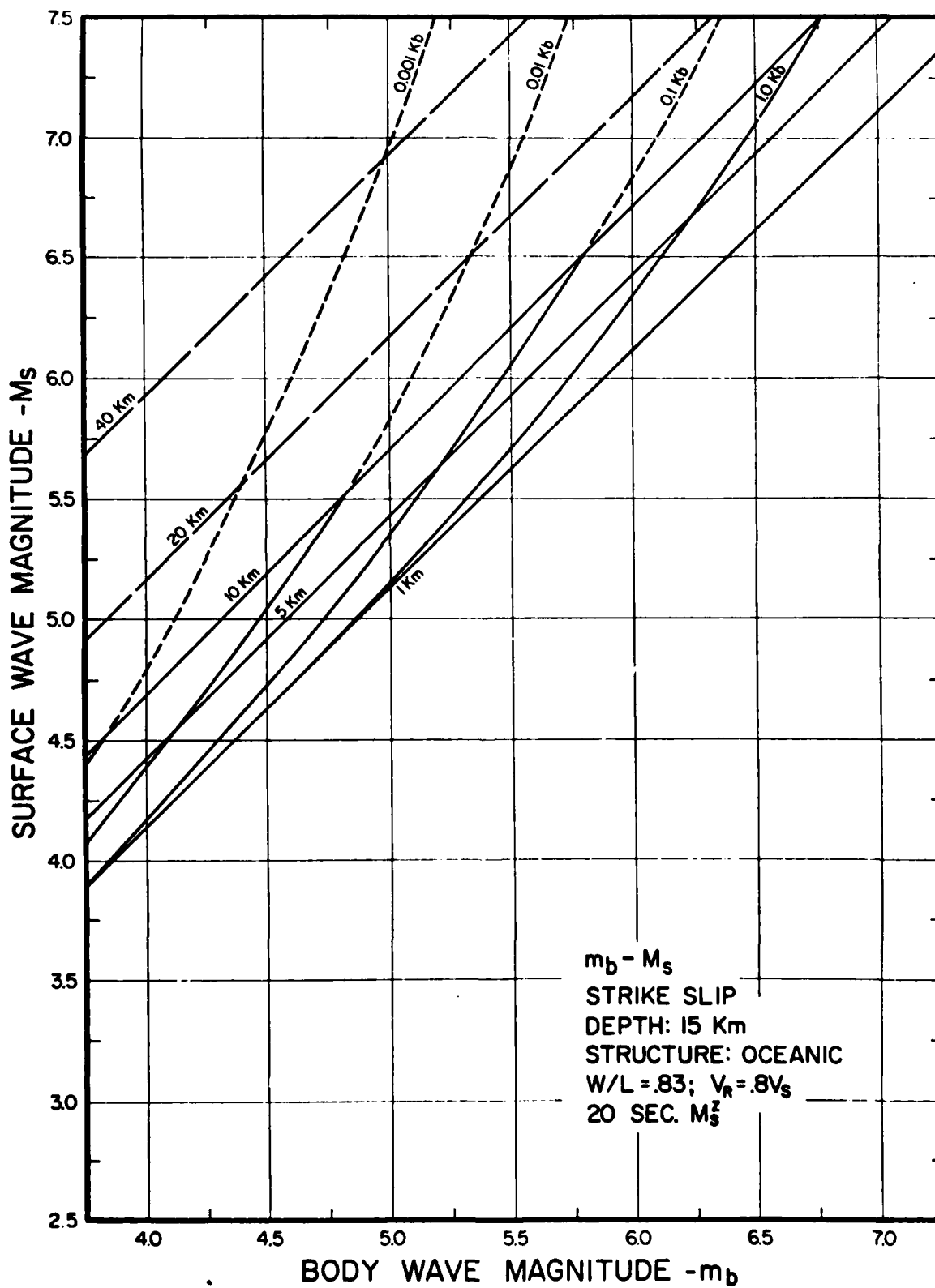
Figure 5-a.

Figure 5-b.
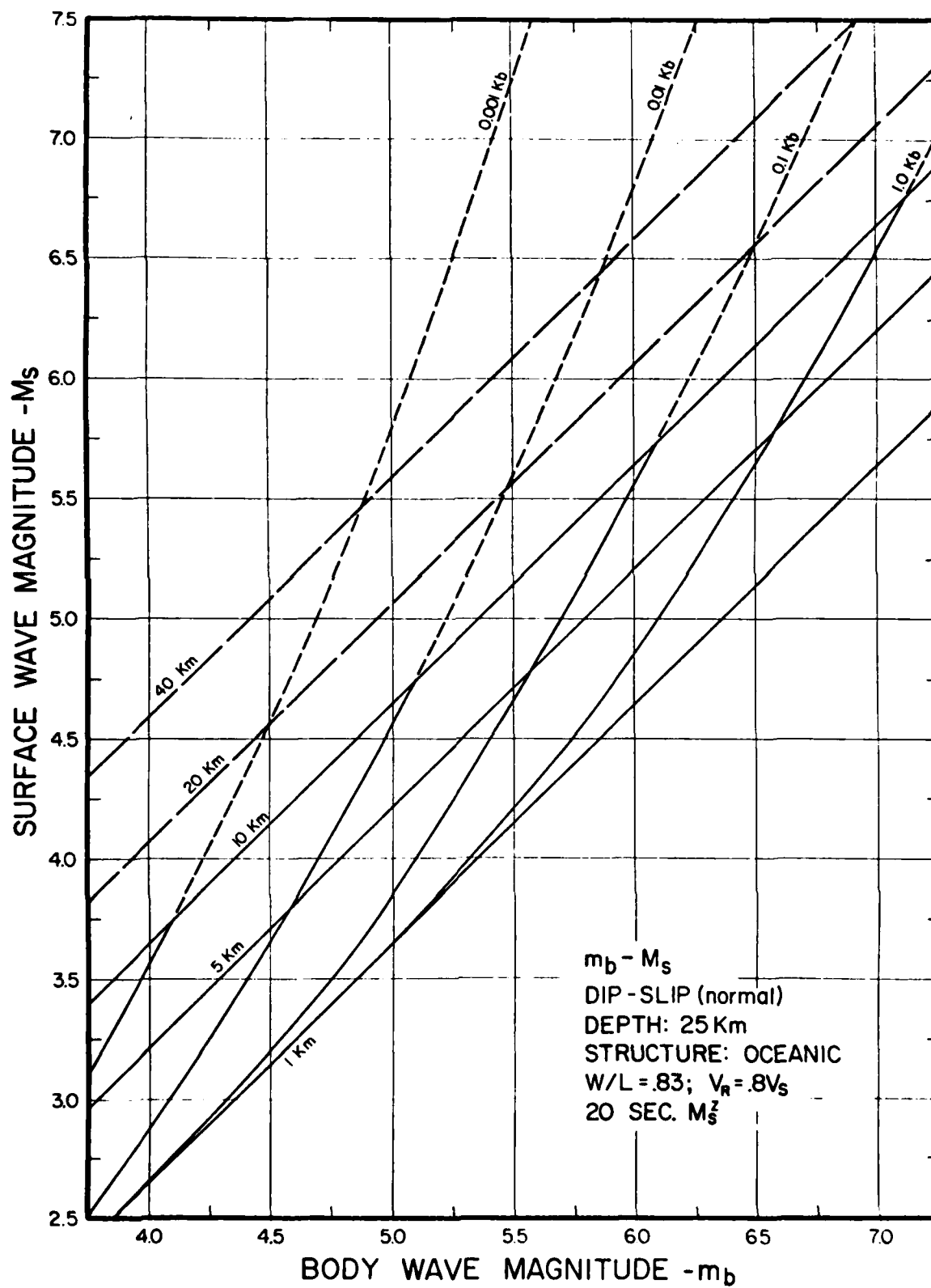
Figure 5-c.

Figure 5-d.

Figure 5-e.

Figure 6-a.

Figure 6-b.

Figure 6-c.

Figure 6-d.